Characterization of oceanic signatures in the Earth's magnetic field in view of their applicability as ocean model constraints

Dissertation

zur Erlangung des Doktorgrades
der Naturwissenschaften
vorgelegt von

CHRISTOPHER IRRGANG

am Fachbereich Geowissenschaften der Freien Universität Berlin,
angefertigt am Deutschen GeoForschungsZentrum GFZ, Potsdam.

Berlin, 2017

„There is pleasure in recognising old things from a new viewpoint."

    — Richard Feynman

Abstract

The general circulation of the world ocean generates characteristic magnetic signals by interacting with the ambient geomagnetic field. These ocean-induced magnetic signals can principally be measured by satellites and could serve as indirect observations of the ocean. Since the so-called motionally induced magnetic field is to first order proportional to conductivity-weighted and depth-integrated ocean velocities, global oceanic magnetic field observations could provide new constraints on oceanic transports of water, heat, and salinity. However, many aspects of electromagnetic induction in the ocean are either not well understood or unknown. This ranges from the basic characterization of motional induction in the ocean to possible applications and benefits for ocean modelling. This cumulative thesis encompasses the characterization of electromagnetic induction in the ocean, both in terms of physical properties and model uncertainties. One new application of electromagnetic induction in the ocean is investigated, namely the possibility to constrain an ocean general circulation model with satellite observations of the ocean-induced magnetic field.

An electromagnetic induction model is implemented into an ocean general circulation model. This model combination allows the investigation of specific influences of seawater properties on motional induction. In previous studies, the electric conductivity of seawater was often treated in a simplified way by assuming it to be uniformly distributed in the ocean and temporally constant. In the first application of the combined numerical models, it is shown that this assumption is insufficient for capturing the temporal variability of motional induction accurately. Considering a realistic three-dimensional seawater conductivity distribution based on ocean temperature and salinity increases the temporal variability of ocean-induced magnetic signals by up to 45 %. These changes are found to predominantly originate from large vertical gradients of seawater conductivity in the upper ocean.

The modelling of the general ocean circulation and of motional induction is affected by various uncertainties and errors, which are introduced by forcing input data and by the numerical models themselves. For potential applications of motional induction, e.g.,

a reliable comparison of model results with observational data, or data assimilation experiments, a realistic estimation of model uncertainties is essential. Ensemble simulations based on different error scenarios are performed to estimate the aggregated uncertainty of the modelled ocean-induced magnetic field. It is shown that the uncertainty of the modelled ocean-induced magnetic field reaches up to 30 % of the signal strength and is subject to large spatial and seasonal variations. The wind stress forcing of the ocean model is a major source of uncertainty. However, specific spatially and temporally robust regions are identified in the ocean-induced magnetic field that retain a small uncertainty in all error scenarios.

Based on the previous findings, data assimilation experiments with artificial satellite observations of the ocean-induced magnetic field are designed and conducted for the first time. In a model-based twin study, artificial satellite observations of the oceanic magnetic field are generated and sequentially assimilated into an ocean general circulation model with a localized ensemble Kalman filter. The impact of the data assimilation on the induced magnetic field, ocean velocities, temperature, and salinity is measured. Compared to a reference simulation without data assimilation, the ocean-induced magnetic field is improved by up to 17 % globally and up to 54 % locally. Improvements of the underlying depth-integrated ocean velocities show values up to 7 % globally, and up to 50 % locally. These improvements result from a consistently better recovery of ocean velocities from the sea surface down to the bottom of the ocean. However, the Kalman filter fails to improve ocean temperature and salinity globally. Kalman filter adjustments of the wind stress forcing of the ocean model are found to be essential for a successful data assimilation.

Kurzfassung

Die allgemeine Zirkulation des Weltozeans generiert charakteristische magnetische Signale durch Wechselwirkungen mit dem umgebenden geomagnetischen Feld. Diese ozeanisch induzierten Magnetfeldsignale können prinzipiell von Satelliten aufgezeichnet werden und somit als indirekte Beobachtungen des Ozeans Anwendung finden. Da das sogenannte bewegungsinduzierte Magnetfeld in erster Näherung proportional zu leitfähigkeitsgewichteten und tiefenintegrierten Geschwindigkeiten im Ozean ist, könnten globale Beobachtungen des ozeanischen Magnetfeldes neue Restriktionen für ozeanische Wasser-, Wärme-, und Salztransporte bieten. Viele Aspekte der elektromagnetischen Induktion im Ozean sind jedoch entweder nur unzulänglich verstanden oder gänzlich unbekannt; dies reicht von grundsätzlichen Eigenschaften der Bewegungsinduktion im Ozean bis hin zu möglichen Anwendungen jener und möglicher Nutzbarkeit für die Ozeanmodellierung. Diese kumulative Arbeit umfasst die Charakterisierung der elektromagnetischen Induktion im Ozean im Sinne von physikalischen Eigenschaften und Modellierungsunsicherheiten. Ferner wird die Realisierbarkeit untersucht, ein numerisches Ozeanmodell der allgemeinen Zirkulation durch Satellitenbeobachtungen des ozeanisch induzierten Magnetfeldes zu beschränken.

Ein elektromagnetisches Induktionsmodell wurde in ein Ozeanmodell der allgemeinen Zirkulation implementiert. Diese Modellkombination erlaubt die Untersuchung spezifischer Einflüsse von Meerwassereigenschaften auf die Bewegungsinduktion. In früheren Studien wurde die elektrische Leitfähigkeit des Meerwassers oft vereinfacht berücksichtigt, etwa gleichmäßig verteilt oder zeitlich invariant. Als erste Anwendung der Modellkombination wird gezeigt, dass diese vereinfachten Annahmen nicht ausreichen, um die zeitliche Variabilität der Bewegungsinduktion realistisch abzubilden. Eine dreidimensionale Verteilung der Leitfähigkeit des Meerwassers, die auf simulierten ozeanischen Wärme- und Salzverteilungen basiert, verstärkt die zeitliche Variabilität des ozeanisch induzierten Magnetfeldes um bis zu 45 %. Die Ursache dieser Verstärkung liegt primär in den starken vertikalen Gradienten der Leitfähigkeit des Meerwassers in den oberen Ozeanschichten.

Die Modellierung der allgemeinen Zirkulation und der Bewegungsinduktion wird durch

verschiedene Unsicherheiten und Fehler beeinträchtigt, die sowohl aus den Modellantriebs-daten als auch aus den numerischen Modellen selbst stammen. Für mögliche Anwendungen der Bewegungsinduktion, zum Beispiel für verlässliche Vergleiche zwischen simulierten und gemessenen Daten oder Experimenten zur Datenassimilation, ist eine realistische Abschätzung der Modellunsicherheiten essentiell. Basierend auf verschiedenen Fehlerszenarien wurden Ensemblesimulationen durchgeführt, um die akkumulierte Unsicherheit des modellierten ozeanisch induzierten Magnetfeldes abzuschätzen. Es wird gezeigt, dass die Unsicherheit der modellierten Bewegungsinduktion bis zu 30 % der Signalstärke entspricht und großen räumlichen sowie saisonalen Variationen unterliegt. Die Windschubspannung des Ozeanmodells stellt hierbei eine entscheidende Unsicherheitsquelle dar. Unabhängig von den verschiedenen Fehlerszenarien konnten jedoch zeitlich und räumlich robuste Regionen identifiziert werden, die nur mit niedrigen Unsicherheiten behaftet sind.

Auf den vorherigen Ergebnissen basierend wurden zum ersten Mal Datenassimilationsexperimente mit Satellitenbeobachtungen des ozeanisch induzierten Magnetfeldes konzipiert und durchgeführt. In einer modellbasierten Zwillingsstudie wurden künstlich erzeugte Satellitenbeobachtungen der Bewegungsinduktion mit einem lokalisierten und ensemblebasierten Kalmanfilter in ein Ozeanmodell der allgemeinen Zirkulation assimiliert. Der daraus resultierende Effekt auf das ozeanisch induzierte Magnetfeld, auf Ozeangeschwindigkeiten sowie auf Temperatur und Salzgehalt des Meerwassers wird gemessen. Verglichen mit einer unkorrigierten Simulation ohne Datenassimilation wird das ozeanische Magnetfeld global um bis zu 17 % und lokal bis zu 54 % verbessert. Die erzeugenden tiefenintegrierten Ozeangeschwindigkeiten werden gobal um bis zu 7 % und lokal um bis zu 50 % verbessert. Diese Werte resultieren aus einer konsistenten Korrektur der Ozeangeschwindigkeiten von der Meeresoberfläche bis hin zum Ozeanboden. Temperatur- und Salzverteilungen konnten durch den Kalmanfilter nicht global korrigiert werden. Die Experimente zeigen zudem, dass Anpassungen der Windschubspannung durch den Kalmanfilter essentiell für den Erfolg der Datenassimilation sind.

Contents

1

Introduction

1.1 Historical background

In 1832, Michael Faraday opened the door to the world of electromagnetic induction and, with this, also the consideration of induction processes in conducting fluids quickly gained attention. Soon after, first evidence for large-scale oceanic electromagnetic induction processes was detected in the 1850s, when submarine telecommunication cables started to connect the continents. These cables were subject to periodic voltage disturbances. For the first time, tidally induced electric currents with lunar periods were detected by Wollaston (1881) (see also Meloni et al., 1983) and later quantified by Cherry and Stovold (1946). In the mid-twentieth century, Stommel (1948), Longuet-Higgins (1949), and Longuet-Higgins et al. (1954) proposed to utilize ocean-flow induced electromagnetic disturbances to indirectly measure ocean velocities. Since then, the research interest in monitoring and modelling oceanic electromagnetic fields evolved rapidly.

In terms of field strength and spatial extent, the ocean-induced magnetic field is the smallest geomagnetic field constituent (Fig. 1.1) and it is five orders of magnitude weaker than the geomagnetic core field ($\pm$ 65 000 nT, Thébault et al., 2015). These oceanic magnetic signals are generated by interactions of seawater with the magnetic core field of the Earth. Because of its salt content, seawater is a highly conducting fluid that carries electric charge in the form of dissolved cations and anions. By moving through the geomagnetic core field, the salt-ions are deflected by the Lorentz force, creating electric currents. These currents induce weak magnetic signals with a magnitude of a few nano
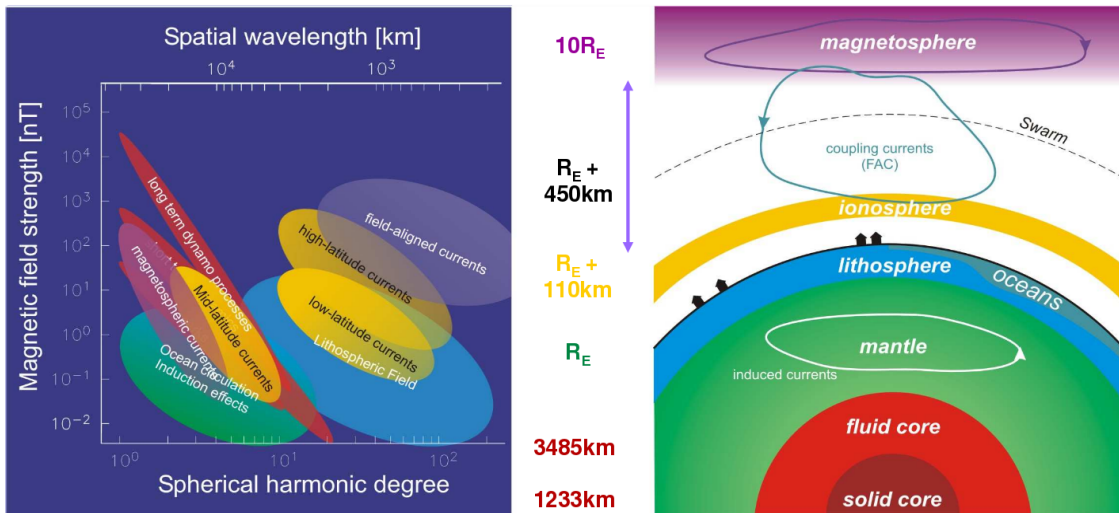
Figure 1.1: Visualization of magnetic field constituents in terms of intensity (left) and origin (right). R_E is the mean Earth radius of 6371 km. Image credit: ESA, Haagmans and Plank

Tesla (Fig. 1.2).

The pioneering modern investigation of the so-called motional induction was governed by Larsen (1968) and Sanford (1971). Sanford's theoretical results have shown a close relation between ocean-induced magnetic signals and depth-integrated ocean velocities that are weighted by the electric conductivity of seawater. The electric conductivity of seawater, in turn, is predominantly depending on seawater temperature and salinity distributions and can be estimated by a polynomial approximation (Apel, 1987). Chave (1983) and Chave and Luther (1990) continued Sanford's work and distinguished between poloidal and toroidal components of motional induction, based on the Helmholtz decomposition of a solenoidal (divergence-free) vector field (see, e.g., Jian-Ming, 2015). The two components differ in their sensitivity towards the type of ocean flow. The poloidal induced magnetic field is generated by toroidal electric currents, i.e., in the horizontal plane, and is predominantly sensitive to conductivity-weighted and depth-integrated ocean velocities. In contrast, the toroidal induced magnetic field is generated by electric currents in the vertical plane and predominantly sensitive to vertical gradients of ocean velocities. Whereas the toroidal induced magnetic field is confined to the ocean interior, the poloidal mode is measurable outside of the ocean, e.g., by land-based and space-borne magnetometers.

1.2   Modelling of motional induction

With the prospect of deriving indirect information about integrated oceanic water, heat, and salinity transports from observations of motional induction (see also Luther and

Chave, 1993), the numerical model-based prediction of oceanic electromagnetic induction started in the 1990s. The estimation of the ocean-induced magnetic field bases on the theory of electromagnetic induction introduced by James Clerk Maxwell (1865), i.e.:

1. Ampère's circuital law: $\qquad \vec{\nabla} \times \vec{B} = \mu_0 \left(\vec{j} + \varepsilon_0 \dfrac{\partial \vec{E}}{\partial t} \right)$ $\qquad\qquad$ (1.1)

2. Maxwell-Faraday equation: $\qquad \vec{\nabla} \times \vec{E} = -\dfrac{\partial \vec{B}}{\partial t}$ $\qquad\qquad\qquad$ (1.2)

3. Gauss's flux theorem: $\qquad \vec{\nabla} \cdot \vec{E} \;\; = \dfrac{\rho}{\varepsilon_0}$ $\qquad\qquad\qquad$ (1.3)

4. Gauss's law for magnetism: $\quad \vec{\nabla} \cdot \vec{B} \;\; = 0$ $\qquad\qquad\qquad$ (1.4)

Additionally, the generation of electric currents due to a moving conductor in presence of electric and magnetic fields is described by Ohm's law, i.e.,

$$\vec{j} = \sigma \left(\vec{E} + \vec{u} \times \vec{B} \right) \; . \qquad\qquad (1.5)$$

Above, $\vec{B}$ is the magnetic field, $\vec{E}$ is the electric field, μ_0 is the permeability of free space, ε_0 is the permittivity of free space, $\vec{j}$ is the electric current density, ρ is the electric charge density, σ is the seawater conductivity, and $\vec{u}$ is the ocean velocity of a moving and conducting particle. Inserting Ohm's law into Maxwell's second equation yields

$$\vec{\nabla} \times \left(\dfrac{\vec{j}}{\sigma} - \vec{u} \times \vec{B} \right) = -\dfrac{\partial \vec{B}}{\partial t} \; . \qquad\qquad (1.6)$$

Displacement currents due to temporal changes of the electric field $\vec{E}$ in equation 1.1 are neglected, leaving solely the oceanic water flow induced electric currents $\vec{j}$ as a source for the induction process. Thus, substituting Maxwell's first equation into equation 1.6 yields the general equation of electromagnetic induction, i.e.,

$$\dfrac{\partial \vec{B}}{\partial t} + \dfrac{1}{\mu_0} \vec{\nabla} \times \left(\dfrac{1}{\sigma} \vec{\nabla} \times \vec{B} \right) = \vec{\nabla} \times \left(\vec{u} \times \vec{B} \right) \; . \qquad\qquad (1.7)$$

Several approaches exist for solving equation 1.7 numerically. Each solution uses different simplifications and is given either in the frequency domain (Kuvshinov and Semenov, 2012), in the time domain (Velímský and Martinec, 2005), or utilizes a so-called magnetostatic thin-sheet approximation (Tyler et al., 1997; Vivier et al., 2004).

The magnetostatic thin-sheet approximation is adopted in this thesis, especially due to its low computational cost, as it provides a simple scalar model equation derived from equation 1.7. The magnetic field $\vec{B}$ is treated as the sum of the geomagnetic core
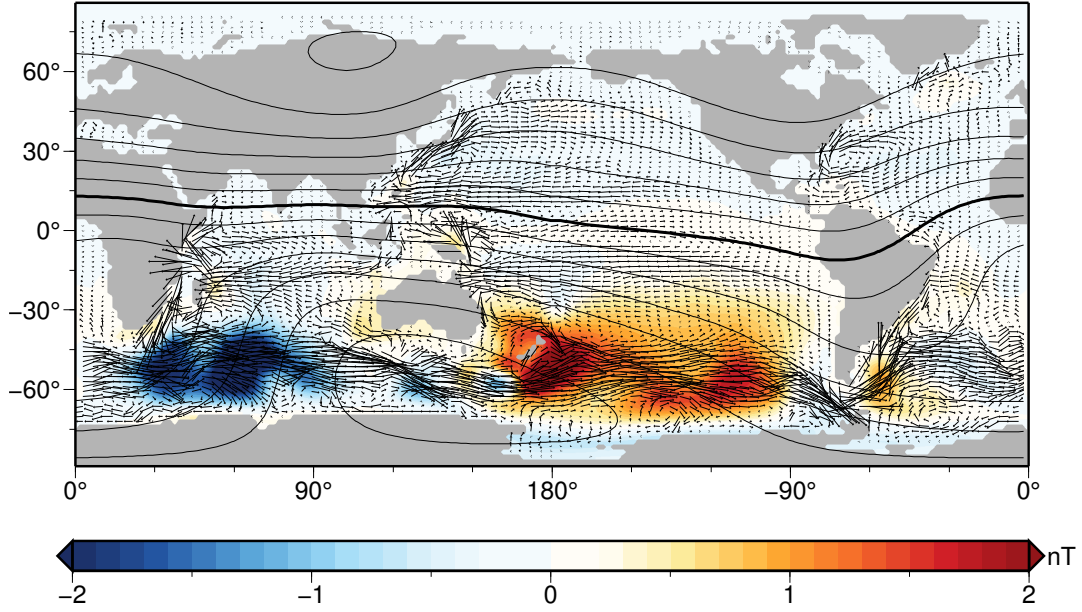
Figure 1.2: Visualization of the electromagnetic induction process due to the general ocean circulation. The colour plot depicts an annual mean field of the radial component b_r of the ocean-induced magnetic field at sea level altitude. Arrows indicate an annual mean field of conductivity-weighted and depth-integrated ocean velocities. Contours show the radial component F_z of the geomagnetic core field. The thick contour line highlights the geomagnetic equator.

field $\vec{F}$ and the ocean-induced magnetic field $\vec{b}$, i.e., $\vec{B} = \vec{F} + \vec{b}$. The ocean basin is considered to resemble a thin spherical layer, assuming that the vertical extent is small compared to the horizontal extent. Thereby, only horizontal and vertically integrated ocean velocities are considered for the induction process. This thin sheet is nested between an insulating atmosphere and an insulating Earth's mantle. The geomagnetic core field $\vec{F}$ is considered constant in time, as temporal variations only become significant for decadal and longer time periods (e.g., Maus et al., 2010), which are not in the scope of this project. Additionally, the self-induction term of the ocean-induced magnetic field, $\vec{u} \times \vec{b}$, is neglected, reducing the source of electric currents to interactions between the moving ocean water and the ambient geomagnetic field. For divergence-free electric currents, an electric stream-function ψ_e can be defined as

$$\int_h \vec{j}\, \mathrm{d}z = -\vec{\nabla}\psi_e \times \vec{e}_z \,, \tag{1.8}$$

where h is the height of the water column from ocean bottom to sea surface and $\vec{e}_z$ is the unit vector in vertical direction. Considering these simplifications, the electromagnetic

induction equation 1.7 is transformed into a scalar model equation for ψ_e, i.e.,

$$\nabla \cdot \left(\Sigma^{-1} \nabla \psi_e \right) = \nabla \cdot \left(\Sigma^{-1} F_z \int_h \sigma u_H dz \right) , \tag{1.9}$$

where u_H is the horizontal ocean velocity, F_z is the radial component of the geomagnetic field, and

$$\Sigma = \int_h \sigma \, \mathrm{d}z \tag{1.10}$$

is the ocean conductance, i.e., depth-integrated seawater conductivity. The ocean-induced magnetic field $\vec{b}$ is estimated from the numerically calculated electric stream-function ψ_e. Therefore, $\vec{b}$ is expressed as the gradient of a potential field P as

$$\vec{b} = -\vec{\nabla} P , \tag{1.11}$$

provided that no electric currents are present in the atmosphere. As the ocean-induced magnetic field is divergence-free (non-existence of magnetic monopoles, given by $\nabla \cdot \vec{b} = 0$), a Laplacian boundary value problem can be formulated for the potential field P as

$$\vec{\nabla}^2 P = 0 , \tag{1.12}$$

$$P(r \to \infty) = 0 , \tag{1.13}$$

$$P(r = a + \zeta) = -\frac{1}{2}\mu_0 \psi_e , \tag{1.14}$$

where r is the height above sea level, a is Earth's mean radius, and ζ is the sea surface height. In spherical coordinates, the solution of this boundary value problem is represented by a spherical harmonics expansion (see, e.g., Atkinson and Han, 2012). Thereby, also the solution of the radial component of the ocean-induced magnetic field is known and allows to calculate the emitted signal at any desired altitude above sea level, i.e.,

$$b_r(\phi, \vartheta, r) = \frac{\partial}{\partial r} P(\phi, \vartheta, r) = \sum_{j=0}^{\infty} \sum_{m=-j}^{j} \frac{1}{2} \frac{\mu_0}{r} \psi_{jm} \left(\frac{a}{r} \right)^{j+1} (j+1) Y_{jm}(\phi, \vartheta) . \tag{1.15}$$

Here, ϕ and ϑ are longitudinal and colatitudinal coordinates on the sphere, a is the Earth's radius, r is the height above sea level, ψ_{jm} are the expansion coefficients of the spherical harmonics functions $Y_{jm}(\phi, \vartheta)$, and j and m are degree and order, respectively. Combined with a general ocean circulation model that provides the electromagnetic source, i.e., horizontal ocean velocities, heat, and salinity distributions, the thin-sheet induction model forms an efficient way for estimating global fields of the ocean circulation induced magnetic field at both sea level and satellite altitude. Further details on the mathematical background of oceanic electromagnetic induction can be found in Dostal (2014).

1.3   Present state of research

Regardless of the utilized numerical models, previous studies can be categorized according to the type of the considered ocean flow, for example, general ocean circulation, ocean tides, or extreme events like tsunamis.

Stephenson and Bryan (1992) numerically estimated the global ocean circulation induced electromagnetic field from a climatologically forced ocean general circulation model. These efforts were continued and extended by Tyler and Mysak (1995), Flosadóttir et al. (1997), Tyler et al. (1997), and Tyler et al. (1998), who were stressing that ocean circulation induced magnetic signals could be strong enough for space-borne measurements via low-Earth-orbiting satellites. More recent studies specifically focused on induced magnetic signals in the Antarctic Circumpolar Current (Vivier et al., 2004), spatial and temporal variability of motional induction (Glazman and Golubev, 2005), and sensitivity of motional induction to seasonal variations in the wind- and density-driven ocean circulation (Manoj et al., 2006). All previous studies are in agreement that the detection of the ocean circulation induced component in magnetic field observations poses a challenge, largely due to the comparatively weak signal strength and the complex and irregular superposition of different magnetic field constituents (see also the review conducted by Kuvshinov, 2008).

So far, the separation of the non-periodic ocean circulation induced magnetic signals has not yet been achieved. In contrast, the numerically predicted periodic magnetic signals induced by the principal lunar semi-diurnal (M2) tide have been identified in land observatories (Maus and Kuvshinov, 2004), in ocean-bottom measurements (Schnepf et al., 2014), by combined satellite observations from CHAMP, Ørsted, and SAC-C (Tyler et al., 2003; Sabaka et al., 2015), and by satellite observations from Swarm (Sabaka et al., 2016). Due to the galvanic coupling of tide currents to media below the ocean and due to the well known period of M2 variations, the M2 induced magnetic field was found suitable for probing the electric conductivity structure of the lithosphere and upper mantle down to a depth of approximately 250 km (Schnepf et al., 2015; Grayver et al., 2016).

Furthermore, local observations of oceanic electromagnetic induction might also be suitable for tsunami early warning systems. Therefore, continuous efforts are made to detect and to utilize tsunami-generated magnetic field anomalies recorded by ocean bottom magnetometers (e.g., Toh et al., 2011; Minami et al., 2015; Schnepf et al., 2016).

The Swarm satellite mission of the European Space Agency introduced a renaissance for research in oceanic electromagnetic induction (Friis-Christensen et al., 2006). The satellite trio is the latest geomagnetic field mission and measures the magnetic field of the Earth with unprecedented precision and resolution of up to 0.1 nT (see Table 1.1). For the first time, ocean circulation induced magnetic signals and their spatio-temporal

Table 1.1: Recent geomagnetic field satellite missions. Resolution values are given for the mounted scalar magnetometers on the satellites.

Name	Mission runtime	Orbit altitude [km]	Resolution [nT]
Ørsted[1]	Since Feb. 1999	630 − 830	0.5
CHAMP[2]	Jul. 2000 − Sep. 2010	350 − 450	0.5
SAC-C[3]	Nov. 2000 − Aug. 2013	700	1.0
Swarm[4]	Since Nov. 2013	450 − 530	0.1

[1] Lundahl et al. (1999) [2] Reigber et al. (2002) [3] Colomb et al. (2001) [4] Friis-Christensen et al. (2006)

variations are in the range of space-borne observational precision. The detection of the weak ocean circulation induced magnetic signals was defined as one of the research objectives of the Swarm mission (Friis-Christensen et al., 2006). Consequently, separable satellite observations of the ocean circulation induced magnetic field have the potential to be utilized as global indirect observations of the world ocean, which contain integrated information about transports of oceanic water, heat, and salinity. These global constraints, in turn, provide the opportunity to correct ocean general circulation models with data assimilation methods. Thereby, observations of motional induction could complement existing ocean observing techniques, e.g., satellite altimeter measurements (TOPEX/Poseidon, Fu et al. (1994); Jason-1, and Jason-2, Masters et al. (2012)), satellite gravity field measurements (GRACE, Tapley et al., 2004), or in-situ measurements from ocean bottom pressure gauges (e.g., Macrander et al., 2010) and profiling floats (ARGO, Roemmich et al., 2009). All ocean observing techniques have different focuses, advantages and limitations. Thus, often combinations of the former are utilized. Observations of the ocean-induced magnetic field contain aggregated information about ocean velocities from sea surface to ocean bottom, including both barotropic and baroclinic ocean flows, and effects due to friction. The dominant dependency of electric seawater conductivity on oceanic temperature and salinity could also allow a derivation of integrated information about global oceanic heat and salinity transports. Additionally, oceanic magnetic signals are detectable in ice-covered regions (Friis-Christensen et al., 2006). These features hold out the prospect that a satellite-based global coverage of observed oceanic electromagnetic signals provides a promising additional tool for improving the current understanding of large-scale ocean dynamics.

1.4   Aims and structure of this thesis

The separation of ocean circulation induced magnetic signals from satellite observations has not yet been achieved. However, there is a high potential for novel applications of electromagnetic induction in the ocean, as respective studies on ocean tidal magnetic signals have already shown (see section 1.3). Additionally, the Swarm satellite mission opens up a new era of high-resolution geomagnetic field measurements, which is expectedly leading to a global coverage of ocean-induced magnetic field observations.

This cumulative thesis contributes to the research topic of motional induction by utilizing numerical models in the framework of three consecutive studies. Each of the following chapters contains a separate study in the form of a published, or currently reviewed, manuscript. The three studies answer research questions in the subjects of *physical characterization, uncertainty estimation*, and *data assimilation*, respectively. Between the chapters, the studies are connected through context passages. The first two studies focus on the model-based estimation of spatio-temporal patterns of motional induction and their sensitivity towards both oceanographic processes (chapter 2) and modelling uncertainties (chapter 3). Numerical model-based sensitivity analyses are a powerful tool to understand the spatio-temporal behaviour of electromagnetic induction in the ocean, and also to assess the robustness of these numerical simulations. Thus, the results close existing knowledge gaps and also support the ongoing effort to detect ocean circulation induced magnetic signals in observations. The third study (chapter 4) builds upon the findings of the two previous studies and focusses on the feasibility to correct an ocean general circulation model by assimilating model-based satellite observations of the ocean-induced magnetic field. Chapter 5 summarizes the results of this thesis and provides an outlook for future studies.

Physical characterization

How strong is the ocean-induced magnetic field?

What are the spatio-temporal patterns of the ocean-induced magnetic field?

How sensitive is motional induction towards changes in seawater conductivity?

In the first study, chapter 2, a model combination of an ocean general circulation model and an electromagnetic induction model is presented. This model combination does not only allow the estimation the ocean-induced magnetic field at the sea surface and at satellite altitude, but also to test the sensitivity of motional induction against oceanographic quantities. An accurate and realistic numerical prediction of the irregular and non-periodic ocean circulation induced magnetic signals supports the ongoing effort to identify these signals in satellite observations. Especially the estimation of temporal

variations of the ocean-induced magnetic field is important in this course, since they distinguish the oceanic component from other more static magnetic field constituents. Still, the sensitivity of motional induction and its variations in the ocean towards oceanographic phenomena is rarely considered. In this study, the model combination is utilized to investigate the previously unknown influence of spatial and temporal variations of the electric seawater conductivity on motional induction.

Uncertainty estimation

Which error sources affect simulations of motional induction?

What is the aggregated uncertainty of the simulated ocean-induced magnetic field?

Are there robust regions in the simulated ocean-induced magnetic field?

In the second study, chapter 3, the numerical modelling of electromagnetic induction in the ocean is complemented with the estimation of model uncertainties. In contrast to sensitivity analyses of simulated motional induction with respect to ocean water properties, realistic numerical predictions of the ocean-induced magnetic field also include the estimation of errors in forward simulations. These errors have various sources, for example, deficiencies in the atmospheric forcing of the ocean model. The robustness of motional induction simulations with respect to model uncertainties is unknown. However, this knowledge is crucial for applications, like reliable comparisons of measured and simulated oceanic magnetic signals. Therefore, ensemble simulations of the introduced model combination (chapter 2) are performed in this study to estimate modelling uncertainties of the ocean-induced magnetic field. The ensembles are generated from calculated error covariance matrices, which are also a key component for data assimilation studies.

Data assimilation

Is it feasible to constrain an ocean model with motional induction satellite observations?

How large is the beneficial impact on the ocean model state?

What are the limitations of this application?

In the third study, chapter 4, the possibility to constrain an ocean general circulation model with satellite observations of motional induction is investigated. In this novel procedure, satellite observations of the ocean-induced magnetic field are assimilated into an ocean general circulation model. For this, the findings from the previous studies (chapters 2 and 3) are combined to design and to conduct the first motional induction data assimilation experiments. Since actual satellite observations of the ocean-induced magnetic field do not exist at this point, artificial satellite observations are derived from the combined ocean model and electromagnetic induction model. By using an ensemble-based

Kalman filter in a synthetic twin-experiment, the benefits and challenges of constraining an ocean general circulation model with satellite observations of ocean-induced magnetic signals are analyzed in a controlled environment.

2

Impact of variable seawater conductivity on motional induction simulated with an ocean general circulation model

Chapter Abstract

Carrying high concentrations of dissolved salt, ocean water is a good electrical conductor. As sea-water flows through the Earth's ambient geomagnetic field, electric fields are generated, which in turn induce secondary magnetic fields. In current models for oceanic induced magnetic fields, a realistic consideration of sea-water conductivity is often neglected and the effect on the variability of the oceanic induced magnetic field unknown. To model magnetic fields that are induced by non-tidal global ocean currents, an electromagnetic induction model is implemented into the Ocean Model for Circulation and Tides (OMCT). This provides the opportunity to not only model oceanic induced magnetic signals, but to assess the impact of oceanographic phenomena on the induction process. In this paper, the sensitivity of the induction process due to spatial and temporal variations in sea-water conductivity is investigated. It is shown that assuming an ocean-wide uniform conductivity is insufficient to accurately capture the temporal variability of the magnetic signal. Using instead a realistic global sea-water conductivity distribution increases the temporal variability of the magnetic field up to 45 %. Especially vertical gradients in sea-water conductivity prove to be a key factor for the variability of the oceanic induced magnetic field. However, temporal variations of sea-water conductivity only marginally affect the magnetic signal.

2.1   Introduction

The principle of electromagnetic induction due to water flow is long known and was first described by Faraday (1832). As the oceans move through the Earth's ambient geomagnetic field, salt-ions in ocean water are deflected by the Lorentz force. Thereby, spatial accumulations of electric charge are formed, leading to the generation of electric currents, which in turn induce secondary magnetic fields. This process is often referred to as "motional induction". Fundamental theoretical work in the modern investigation of ocean generated electric fields was done by Larsen (1968) and Sanford (1971). Chave (1983) discussed electromagnetic induction due to ocean dynamics, as well as the effects of coastlines and the electrical structure of the Earth. With the advance in computational power, ocean models and data have been used in studies to estimate motionally induced magnetic signals. Stephenson and Bryan (1992), Tyler et al. (1997) and Manoj et al. (2006) focused on motional induction due to global ocean circulation, while Tyler et al. (2003), Kuvshinov et al. (2006), Dostal et al. (2012) and Schnepf et al. (2014) discussed the modelling and observation of electromagnetic fields due to ocean tides. Flosadóttir et al. (1997) and Vivier et al. (2004) investigated electromagnetic fields on a regional scale, focusing on the North Atlantic circulation and the Antarctic Circumpolar Current. A comprehensive review of modelling electromagnetic induction in the ocean was conducted by Kuvshinov (2008). Despite the varying research focus of these studies on different oceanographic processes and spatio-temporal scales, there is a consensus regarding the small variability of the oceanic induced magnetic field and its difficult detectability and separability from other magnetic signals in satellite data. In many regions, the crustal magnetic field has comparable or higher amplitudes in satellite measurements which makes it challenging to separate both contributions (Kuvshinov (2008)). The temporal variability of the oceanic induced magnetic field, however, distinguishes it from the static crustal field.

In the above mentioned studies, sea-water conductivity is treated in different ways. Both homogeneous and inhomogeneous sea-water conductivity distributions are used. In addition, sea-water conductivity is assumed either constant or variable in time. Most often, a globally uniform value is used instead of a realistic conductivity distribution in the ocean. Sea-water conductivity can be derived from salinity and temperature, where the temperature is the predominant component. Both exhibit large spatial variations in the ocean and evolve in time. The typical mean conductivity of sea-water lies in the range of $3-4$ Siemens per metre. Strongest changes in sea-water conductivity occur above the main thermocline, with highest values reaching up to 6 Siemens per metre. Chave and Luther (1990) investigated the effect of vertically varying sea-water conductivity on low-frequency, motionally induced electromagnetic fields on a theoretical basis, considering different one-dimensional vertical conductivity profiles. The influence of a realistic three-

dimensional and time-varying sea-water conductivity on the variability of magnetic fields which are induced by the ocean global circulation is still unknown.

The aim of this study is to examine the spatial and temporal influence of sea-water conductivity on the variability of the motionally induced magnetic field in the framework of an ocean global circulation model. This allows to answer the question whether it is necessary to account for a realistic sea-water conductivity distribution in the ocean and which simplifications are justifiable in order to capture the variability of the magnetic field accurately. Therefore, an electromagnetic induction model is coupled to an ocean global circulation model. The two models and the experiment setup are described in Sect. 2.2 of this paper. In Sect. 2.3, the results are presented and discussed. In Sect. 2.4, the conclusions are drawn and a summary is given.

2.2   Methodology

2.2.1   Global Ocean Model

The Ocean Model for Circulation and Tides (OMCT, Thomas et al. (2001), Dobslaw and Thomas (2007)) is used to model and simulate the global ocean circulation. The model is based on non-linear balance equations for momentum, the continuity equation, and conservation equations for heat and salt. In our configuration, the baroclinic ocean global circulation model (OGCM) uses a horizontal resolution of $1.875° \times 1.875°$, 13 layers in the vertical and a time-step of 30 minutes. The hydrostatic and the Boussinesq approximations are applied, whereas the correction of artificial mass change due to the Boussinesq approximation follows Greatbatch (1994). Tidal flows are not considered in this configuration, as the focus lies solely on global circulation patterns. To generate a realistic distribution and temporal variability of sea-water conductivity and ocean velocities, the model is forced with heat-flux, wind-stress, surface-pressure, precipitation and evaporation, which are based on 6-hourly ERA-Interim products from the European Centre for Medium-Range Weather Forecasts (ECMWF, Dee et al. (2011)). Additionally, the model is forced with daily river-runoff from the Land Surface Discharge Model (LSDM, Dill (2008)) which is also forced by the ECMWF-Interim data.

In this configuration, the OMCT realistically resolves the main features of ocean global circulation, e.g., the Antarctic Circumpolar Current and Western Boundary Currents (see Sect. 2.3 and Dobslaw and Thomas (2007), esp. Figs. 6 and 7). Eddies and other small-scale features are not resolved by the current configuration of the OMCT. These features have a considerable effect on the motionally induced magnetic field at sea-surface. Due to the smoothing effect of the upwardly continuation to satellite altitude, however, the small-scale features are neither visible in the spatial pattern of the magnetic signal at

satellite altitude nor affecting the estimated strength of the magnetic signal (Vennerstrom et al. (2005)). In the present study, the focus lies therefore on large-scale ocean global circulation patterns that predominantly characterize the oceanic induced magnetic signal at both sea-surface and satellite altitude. Nevertheless, the findings of the experiments in this study are applicable to both eddy-resolving models and models of tidal motion.

2.2.2   Electromagnetic Induction Model

The electromagnetic induction model is based on a 2-D induction equation and follows the same model approach as Vivier et al. (2004) and Tyler et al. (1997). Vertical ocean flow velocities are neglected and a thin-shell approximation is used which contains depth-integrated and conductivity-weighted horizontal flow and induced electric currents. The atmosphere and upper mantle are treated as insulators (Vivier et al. (2004), Parkinson and Hutton (1989)). The thin shell is allowed to include an underlying layer of conductive sediments. Therefore, a global sediment conductance map has been derived using the method described by Everett et al. (2003) and sediment thicknesses of Laske and Masters (1997). Using this approach, the radial component of the motionally induced primary poloidal magnetic field is calculated. The primary toroidal oceanic induced magnetic signals are not considered in this study, since these are confined to the oceans and cannot be measured from the outside. Nevertheless, the toroidal component couples with the large conductivity contrasts between the oceans and continents, which leads to the generation of secondary poloidal magnetic signals along the oceanic shorelines (Dostal et al. (2012), Szuts (2010)). In this study, only the primary poloidal induced magnetic signatures are considered that directly originate from large-scale ocean global circulation and that can be recorded at both sea surface and satellite altitude.

According to Vivier et al. (2004), the induced electric currents in the horizontal plane can be expressed as an electric stream function ψ_e which leads to a scalar model equation derived from Ampere's Law and Ohm's Law:

$$\nabla \cdot \left(\Sigma^{-1} \nabla \psi_e \right) = \nabla \cdot \left(\Sigma^{-1} F_z \int_h \sigma \boldsymbol{u}_H dz \right) \; . \tag{2.1}$$

Here, h is the variable height of the thin shell according to the bathymetry, Σ is the depth-integrated conductivity, σ is the conductivity at a given point, F_z is the radial part of the Earth's ambient geomagnetic field and $\boldsymbol{u}_H$ is the horizontal ocean flow velocity. F_z is derived from the POMME-6 Magnetic Model of the Earth and $\boldsymbol{u}_H$ is prognostically calculated with OMCT. The induced magnetic field b_r is then calculated from the stream

function ψ_e using spherical harmonic expansion:

$$b_r(\phi, \vartheta, r) = \sum_{j=0}^{j_{\max}} \sum_{m=-j}^{j} \frac{1}{2} \frac{\mu_0}{r} \psi_{jm} \left(\frac{a}{r}\right)^{j+1} (j+1) Y_{jm}(\phi, \vartheta) \, . \tag{2.2}$$

Here, ϕ and ϑ are longitudinal and colatitudinal coordinates on the sphere, μ_0 is the permeability of free space, a is the Earth's radius, r is the height above sea level, ψ_{jm} and $Y_{jm}(\phi, \vartheta)$ are the spherical harmonic coefficients and functions. The spherical harmonic coefficients are calculated according to Driscoll and Healy (1994). In consequence of applying a spherical harmonic expansion, this approach gives the opportunity to easily calculate the motionally induced magnetic field at both sea level and satellite altitude. The ocean model's horizontal resolution of $1.875° \times 1.875°$ corresponds to a global grid size of 194×96 grid cells. In order to prevent aliasing effects that would otherwise occur during grid transformations, the maximum degree and order of the spherical harmonic expansion $j_{\max}$ is limited to $47 = \frac{96}{2} - 1$ (Driscoll and Healy (1994)).

2.2.3 Sea-Water Conductivity Distribution Experiments

The OMCT prognostically calculates ocean velocities, salt and temperature distributions at every time step (Thomas et al. (2001)). The variables are sub-sampled and stored daily over the simulation period of one year. From OMCT salt and temperature values the sea-water conductivity is estimated using the transformation method from Apel (1987), resulting in 3-D spatio-temporal variable conductivity distributions.

In order to assess the influence of sea-water conductivity distributions on the motional induction process, three simulation experiments are performed. For all three experiments the motionally induced magnetic field is calculated using different distributions of sea-water conductivity, but from the same previously stored OMCT velocities and the same background magnetic field. For the first experiment ("constant conductivity experiment"), a globally uniform and constant in time mean sea-water conductivity of 3.5 S/m is applied at every grid point and every time step. For the second experiment ("spatially-variable-conductivity experiment"), the previously stored three dimensional and temporal variable conductivity distribution is processed. Annual mean values are derived from the conductivity distribution for every grid point, resulting in a 3-D variable but time-constant conductivity. For the third experiment ("spatio-temporal-variable-conductivity experiment"), the fully spatio-temporal variable conductivity distribution is utilized to calculate the induced magnetic fields.
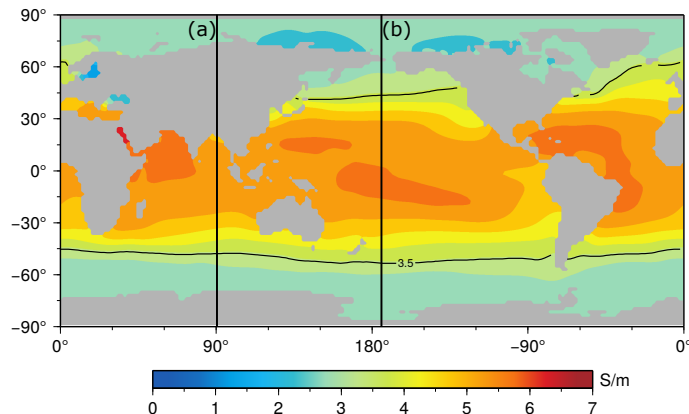
Figure 2.1: Annual mean sea-water conductivity of the upper ocean in Siemens per metre (S/m). The black meridional lines indicate the locations of the sections in the Figs. 2.2 (a) and 2.2 (b). The black contour line indicates the mean conductivity of 3.5 S/m.
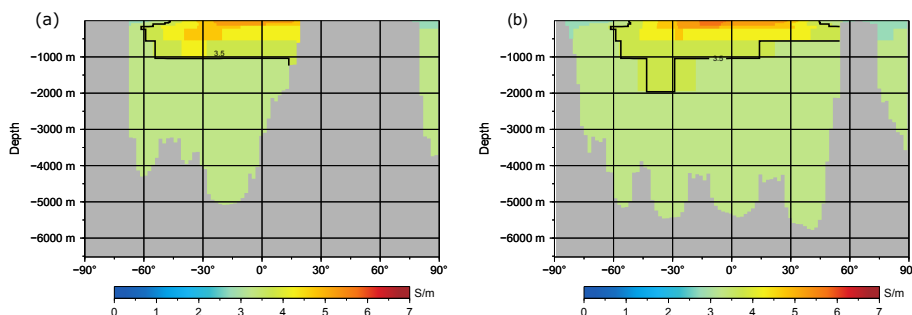

Figure 2.2: Meridional sections of sea-water conductivity distribution at 90°E (a) and 182°E (b). Ocean depth is given in metres. The black contour line indicates the mean conductivity of 3.5 S/m.

2.3   Results and Discussion

The annual mean global sea-water conductivity distribution at sea surface and two representative longitudinal depth-profiles is depicted in Figs. 2.1 and 2.2. Note, that this conductivity distribution exhibits both horizontal and vertical gradients, affecting the conductivity-weighting of the horizontal ocean velocities $\boldsymbol{u}_H$ (see Eq. 2.1). Due to high temperature and salinity values, the highest values of up to 6 S/m occur in equatorial and some coastal regions. A decrease of conductivity arises in poleward directions where lower temperature and salinity values occur. The depth profiles show that the least conducting areas are located in polar regions and lower parts of the ocean basin with values as low as 2.5 S/m. In comparison to equatorial regions, depth-profiles in polar areas show an inverted conductivity gradient with lowest values in the upper ocean.

When using a globally uniform sea-water conductivity, the signals of the motionally induced magnetic field at sea level due to global ocean circulation range from $-5\ nT$ to $4\ nT$ at sea level altitude. Mean values over the simulation period are in the range of -4
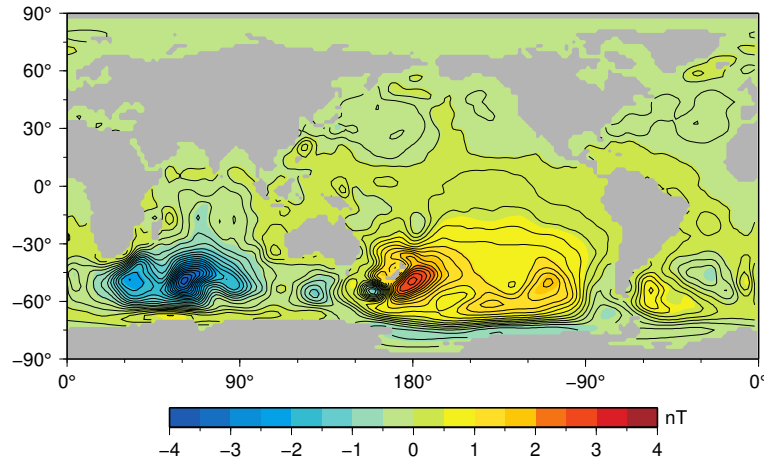
Figure 2.3: Annual mean values of motionally induced magnetic field at sea level altitude due to ocean global circulation from the constant conductivity experiment in nano Tesla (nT).

to 3 nT (Fig. 2.3). The local standard deviation reaches up to 10 % of the signal strength (Fig. 2.4). The strongest signals and variabilities occur in the area of the Antarctic Circumpolar Current (ACC). The characteristic separation into one positive part east of Australia and one negative part west of Australia are caused by the shape of the Earth's ambient geomagnetic field. Additional features are visible, e.g., the North Atlantic circulation and Western Boundary Currents along the eastern coasts of South Africa, South America or Japan. The results of the motionally induced magnetic field show good agreement with previous studies, e.g., Fig. 2 in Vivier et al. (2004) and Fig. 3 in Manoj et al. (2006). Vivier et al. (2004) compared motionally induced magnetic fields and their variability as calculated by three different ocean general circulation models (OGCM). For all three calculations, the same depth-integrated conductivity transport from one of the OGCMs is used. Manoj et al. (2006) utilized a mean sea-water conductivity of 3.2 S/m to calculate the exciting electric current in the ocean and a spatially-variable sea-water conductivity for modelling the shell conductance.

In order to assess the influence of the 3-D sea-water conductivity distribution on the variability of the magnetic signal, results from the constant conductivity experiment and spatially-variable-conductivity experiment are compared. Figure 2.5 shows the difference in the standard deviation of the magnetic signal, relative to the spatially-variable-conductivity experiment. Positive values indicate that using spatially variable conductivity profiles results in a larger temporal variability of b_r, whereas negative values state the opposite effect. Dominant positive areas are located in the zonal limits of $45°S$ and $45°N$ with values up to 45 %. The strongest negative areas, however, predominantly reside beyond $50°S$ and $50°N$, reaching values up to -20 %. The most prominent positive features can be found in the Indian Ocean. Additional positive features are located in
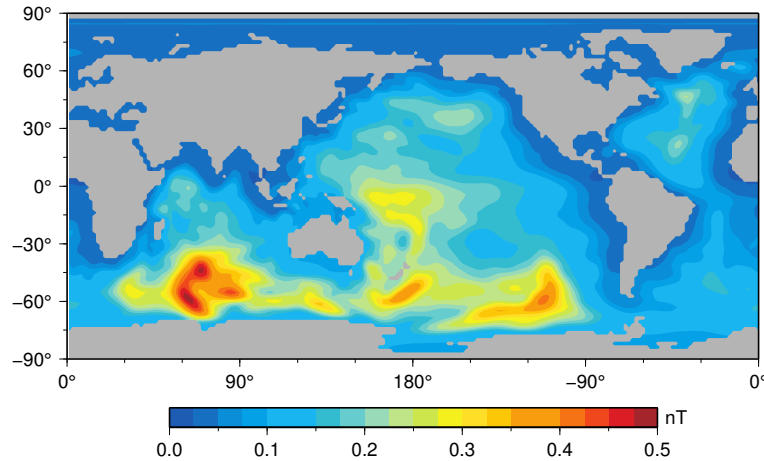
Figure 2.4: Standard Deviation of motionally induced magnetic field at sea level altitude due to ocean global circulation from the constant conductivity experiment in nano Tesla (nT).
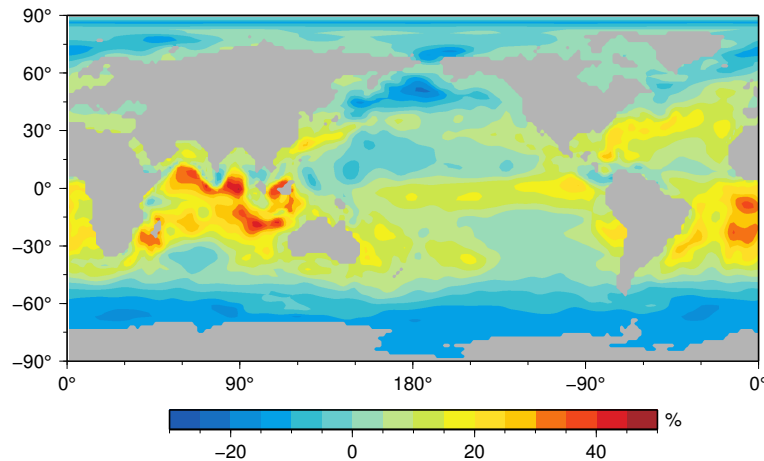

Figure 2.5: Influence of the spatially variable conductivity on the variability of the motionally induced magnetic field.

the area of the Kuroshio current, Agulhas current, east of Australia, along the equatorial jet in the Pacific Ocean, in the Gulf Stream and in the south Atlantic Ocean along the Brazil current. The signatures of the Western Boundary Currents can clearly be identified. Most prominent negative features are located in the area of the Aleutian Islands and the Antarctic Circumpolar Current. Note, that comparing the spatially-variable-conductivity experiment to other uniform conductivity distributions instead of 3.5 S/m will change patterns (especially zero-crossings) and strength of the values shown in Fig. 2.5. The result of a local under- and over-estimation still holds.

The high changes in temporal variability of the induced magnetic field and their spatial pattern are only partly explained by the horizontal conductivity distribution in the spatially-variable conductivity experiment (compare Figs. 2.1 and 2.5). Therefore, the
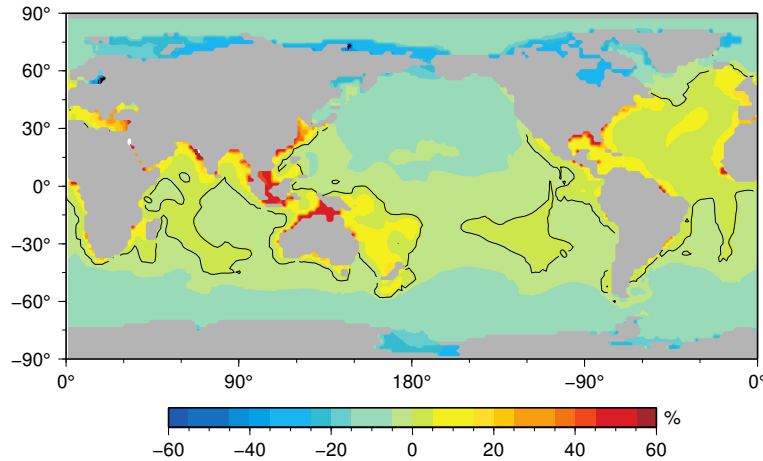
Figure 2.6: Relative difference between depth-mean conductivity used in the spatially-variable-conductivity experiment and globally constant conductivity of 3.5 S/m used in the constant conductivity experiment. The black contour line highlights the transition from positive to negative values.

difference between the depth-mean conductivity of the spatially-variable-conductivity experiment and the globally constant conductivity of the constant conductivity experiment are calculated. The differences are divided by the globally constant conductivity and illustrated in Fig. 2.6, showing the relative increase or decrease of the depth-mean conductivity at any point. The values reside in the range of ±60 % (peak to peak), whereas most changes reside in the range of ±20 %. An increase emerges in areas where the surface conductivity lies above the mean of 3.5 S/m and water-depth is comparably small. Largest decreases occurs in areas where the surface conductivity lies below the mean (see Figs. 2.2 and 2.6). Particularly, coastal regions and oceanic ridges form prominent features, e.g., Central Indian Ridge and East Pacific Rise. The comparison of the conductivity differences (Fig. 2.6) and changes in the variability of the magnetic field (Fig. 2.5) shows much more agreement than Figs. 2.1 and 2.5. Before the depth-integration over the water column according to the thin-shell approximation (Eq. 2.1), ocean flow velocities are multiplied by their specific conductivity. Consequently, ocean flow velocities are weighted by a comparably high conductivity in areas of positive changes in depth-mean conductivity or by a comparably low conductivity in areas of negative changes (see Fig. 2.6). This effect is visible around Indonesia, east of Australia in the Pacific Ocean and in the north Atlantic Ocean (compare Fig. 2.5). Again, the general findings also hold for other globally uniform conductivities than 3.5 S/m.

However, in areas where the most prominent changes in magnetic field variability arise, i.e., Indian Ocean, Aleutian Islands, mid Pacific Ocean and south Atlantic Ocean, only few significant changes in the depth-mean conductivity are visible. These discrepancies are explained by vertical gradients of the conductivity, together with near surface ocean
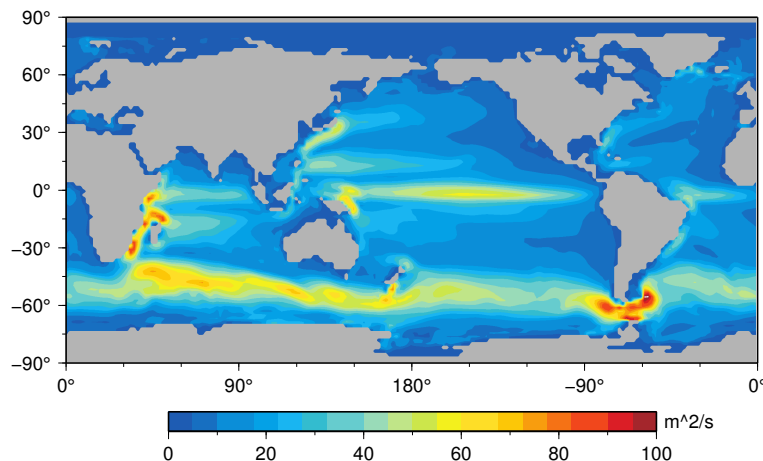
Figure 2.7: Annual mean depth-integrated ocean flow velocities over the upper 1040 metres.

flow velocities and their large temporal variability. Figures 2.7 and 2.8 show annual mean depth-integrated ocean flow velocities over the upper 1040 metres and their standard deviation. The water column thickness of approximately one kilometre is chosen, since the largest deviations in conductivity from the mean occur in this layer (compare Fig. 2.2). In this layer, high ocean flow velocities and variability are weighted by an above-average conductivity in the areas of the Gulf Stream, Indian Ocean, mid Pacific Ocean (compare Figs. 2.2 and 2.8). This leads to an amplification of the magnetic field variability, although the depth-mean conductivity is similar to the globally constant conductivity used in the constant conductivity experiment. In addition, ocean currents are much more visible in the variability of the magnetic signal (see Figs. 2.4 and 2.5). Since the variability of the motionally induced magnetic signal distinguishes the oceanic contribution from the static crustal field, this is a key feature for the detection of global ocean flow in satellite data. The opposite effect occurs in high latitudes. In the Arctic Ocean, around the Aleutian Islands and in the Antarctic Circumpolar Current, high ocean flow velocities and variability in the upper layer are weighted by a below-average conductivity. Here, this leads to a relative dampening of the magnetic field variability.

In order to identify the influence of temporal variability of the conductivity distribution on motional induction, results from the spatially-variable-conductivity experiment and spatio-temporal-variable-conductivity experiment are compared. As opposed to the change of standard deviation induced by spatial conductivity gradients, only negligible differences are determined, which is based on the very small temporal variability of the conductivity distribution. The standard deviation does not exceed 0.7 S/m at the surface and 0.01 S/m below the upper 1040 metres. Consequently, the influence of conductivity distributions on the variability of motionally induced magnetic fields is predominantly driven by spatial contrasts of the conductivity.
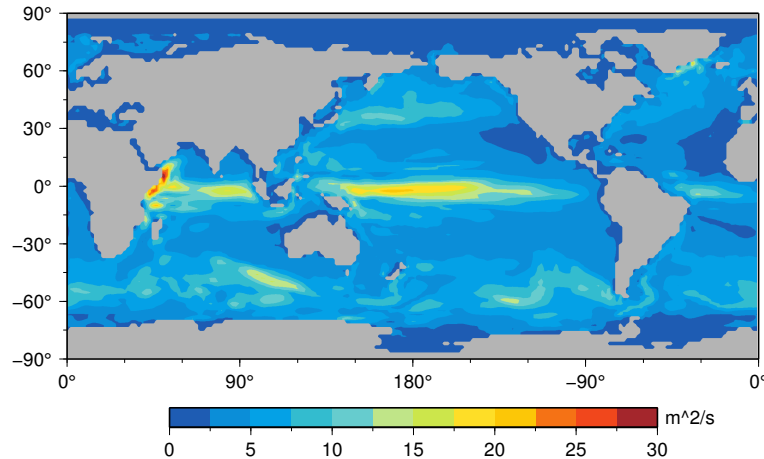
Figure 2.8: Standard Deviation of depth-integrated ocean flow velocities over the upper 1040 metres.

2.4 Summary and Conclusion

In order to model and simulate ocean circulation induced magnetic fields, a 2-D electromagnetic induction model is implemented into the ocean global circulation model OMCT. This combination gives the unique possibility to not only calculate motionally induced magnetic signals, but to assess the impact of oceanographic phenomena on the induction process. All necessary oceanic quantities for the estimation of ocean global circulation induced magnetic signals are calculated by the model. In this study, we focused on the question to what extent spatial and temporal variability in sea-water conductivity influences oceanic induced magnetic fields. Over the simulation period of one year, it is shown that assuming a globally uniform sea-water conductivity is insufficient in order to accurately capture the variability of the oceanic induced magnetic signal. Applying a three dimensional non-uniform conductivity distribution rather than a globally constant conductivity increases the temporal variability of the magnetic field up to 45 % in equatorial regions. In polar regions, a decrease of up to 20 % is detected. Hence, assuming an ocean-wide uniform conductivity leads to an underestimation of the variability of the motionally induced magnetic field in equatorial regions and to an overestimation in polar regions. These variations are only partly explained by horizontal gradients in the inhomogeneous sea-water conductivity distribution. The results show that especially vertical gradients in the conductivity distribution together with the bathymetry form a key feature for changes in the variability of the motionally induced magnetic signal. Ocean currents and their temporal variability in the upper ocean are amplified (dampened) in equatorial regions (polar regions) by the vertical conductivity structure and are, in turn, much more (less) visible in the induced magnetic signal. However, accounting additionally for temporally variable conductivity has negligible impact on the temporal variability of the magnetic

field.

In past studies, different modelling approaches and parametrizations have been used to simulate global ocean induced magnetic fields. There is a consensus regarding the small variability of ocean induced magnetic fields and, consequently, its difficult detectability and separability from other magnetic signals in satellite data, e.g., in many regions, the crustal magnetic field has comparable or higher amplitudes in satellite measurements. The temporal variations of the oceanic induced magnetic field, however, distinguish it from the static crustal field. Thus, it is of particular importance to account for a realistic conductivity distribution in the ocean, in order to capture the temporal variability of the induction process more accurately, which may help future studies to more easily detect global ocean induced magnetic signals in satellite-based measurements.

The results of this study are not solely confined to magnetic fields that are induced by ocean global circulation. In principle, the findings are independent from the configuration of the ocean model, the electromagnetic induction model and other assumptions like the exact value of the globally uniform conductivity used in the constant conductivity experiment. In consequence, related studies dealing with, e.g., toroidal motionally induced magnetic signals, tidal ocean velocities or eddy-resolving model approaches may also benefit from this paper.

Context

In the first study it is demonstrated that seasonal variations in ocean temperature and salinity distributions only have a marginal influence on the electric seawater conductivity and, in turn, on the ocean-induced magnetic field. However, this situation changes for processes over multiannual time periods, e.g., processes related to climate variability. In this context, the lunar semi-diurnal (M2) induced magnetic field could serve as a new observation operator of climate variability induced changes in the ocean. Since anomalies in the induced tidal magnetic field can be assumed to dominantly origin from changes in ocean salinity and temperature distributions, i.e., changes in the electric seawater conductivity, observations of these magnetic signals could be used to detect phenomena associated with climate variability. This technique was recently demonstrated in two co-authored studies by Saynisch et al. (2016, 2017).

One prominent example of climate variability is the melting of ice sheets and its profound impact on both sea level and the general circulation of the world ocean (e.g., IPCC, 2013). For instance, a weakening, or even breakdown, of the Atlantic meridional overturning circulation (AMOC) is connected to increased freshwater fluxes into the ocean from melting of the Greenland ice sheet (Rahmstorf, 1995; Yu et al., 2015). Since these melting induced freshwater fluxes also change the local and global distribution of electric seawater conductivity, an AMOC decay should be observable in the otherwise very well predictable and separable (e.g., Sabaka et al., 2016) tidal (M2) induced magnetic field.

In a model-based sensitivity study, Saynisch et al. (2016) found that a total AMOC decay corresponds to anomalies of up to 0.7 nT in the tidal (M2) induced magnetic field at sea level. Compared to the unperturbed tidal magnetic signal at sea level, the anomalies reach more than 30 % of the signal strength. Consequently, these anomalies should be detectable in long time series from magnetometers at land or in the ocean. At altitudes of the Swarm satellites, the anomalies still amount to 0.1 nT, which is close to the nominal Swarm precision (Friis-Christensen et al., 2006; Olsen et al., 2006).

Previously, the spatio-temporal characteristics of electromagnetic induction in the ocean were discussed. In particular, the importance of electric seawater conductivity was

considered, both in terms of sensitivity of the induced magnetic signals (Irrgang et al., 2016a) and possible applications for monitoring climate variability (Saynisch et al., 2016, 2017). Another aspect is the estimation of uncertainties in the modelled ocean-induced magnetic field, i.e., the reliability of model results with respect to biased or erroneous forcing data of the numerical models. Especially the various atmospheric forcings for ocean models (see, e.g., Dee et al., 2011; Saha et al., 2010), which are provided as reanalysis products by different centers, were subject of many comparison studies (e.g., Chaudhuri et al., 2013, 2014) to identify systematic deficiencies globally (e.g., Decker et al., 2012; Gregg et al., 2014) and locally (e.g., Jakobson et al., 2012; Lindsay et al., 2014). The wind stress forcing was found to contain non-negligible discrepancies that can result in large uncertainties in the wind-driven ocean circulation (Chaudhuri et al., 2013). Considering uncertainties in forcing data is not only crucial for estimating the aggregated error in the simulated ocean-induced magnetic field. A measure of model uncertainties is especially important for reliable comparisons of numerical forward simulations and actual observations (e.g., by satellites). Additionally, the residuals between numerical estimates and actual observations of a geophysical system, together with respective uncertainty ranges in the form of error covariance matrices, are the foundation for data assimilation techniques. Therefore, the study in the next chapter focusses on the range of uncertainty of the modelled ocean circulation induced magnetic field.

3

Ensemble simulations of the magnetic field induced by global ocean circulation: Estimating the uncertainty

Chapter Abstract

The modelling of the ocean global circulation induced magnetic field is affected by various uncertainties that originate from errors in the input data and from the model itself. The amount of aggregated uncertainties and their effect on the modelling of electromagnetic induction in the ocean is unknown. For many applications, however, the knowledge of uncertainties in the modelling is essential. To investigate the uncertainty in the modelling of motional induction at the sea surface, simulation experiments are performed on the basis of different error scenarios and error covariance matrices. For these error scenarios, ensembles of an ocean general circulation model and an electromagnetic induction model are generated. This ensemble-based approach allows to estimate both the spatial distribution and temporal variation of the uncertainty in the ocean induced magnetic field. The largest uncertainty in the ocean induced magnetic field occurs in the area of the Antarctic Circumpolar Current. Local maxima reach values of up to 0.7 nano Tesla. The estimated global annual mean uncertainty in the ocean induced magnetic field ranges from 0.1 to 0.4 nT. The relative amount of uncertainty reaches up to 30 % of the signal strength with largest values in regions in the northern hemisphere. The major source of uncertainty is found to be introduced by wind stress from the atmospheric forcing of the ocean model. In addition, the temporal evolution of the uncertainty in the induced magnetic field shows distinct seasonal variations. Specific regions are identified which are robust with respect to the introduced uncertainties.

◆AGUPUBLICATIONS

JGR

Journal of Geophysical Research: Oceans

RESEARCH ARTICLE

Key Points:
- Largest uncertainties in the ocean-induced magnetic field correspond to 30% of the signal strength
- The major source of uncertainty is introduced by the atmospheric forcing of the ocean model
- Specific robust regions with small uncertainties are identified

Correspondence to:
C. Irrgang,
irrgang@gfz-potsdam.de

Ensemble simulations of the magnetic field induced by global ocean circulation: Estimating the uncertainty

Christopher Irrgang[1,2], Jan Saynisch[1], and Maik Thomas[1,2]

[1]Helmholtz Centre Potsdam, GFZ German Research Centre for Geosciences, Section 1.3: Earth System Modelling, Potsdam, Germany, [2]Freie Universität Berlin, Institute of Meteorology, Berlin, Germany

Abstract The modeling of the ocean global circulation induced magnetic field is affected by various uncertainties that originate from errors in the input data and from the model itself. The amount of aggregated uncertainties and their effect on the modeling of electromagnetic induction in the ocean is unknown. For many applications, however, the knowledge of uncertainties in the modeling is essential. To investigate the uncertainty in the modeling of motional induction at the sea surface, simulation experiments are performed on the basis of different error scenarios and error covariance matrices. For these error scenarios, ensembles of an ocean general circulation model and an electromagnetic induction model are generated. This ensemble-based approach allows to estimate both the spatial distribution and temporal variation of the uncertainty in the ocean-induced magnetic field. The largest uncertainty in the ocean-induced magnetic field occurs in the area of the Antarctic Circumpolar Current. Local maxima reach values of up to 0.7 nT. The estimated global annual mean uncertainty in the ocean-induced magnetic field ranges from 0.1 to 0.4 nT. The relative amount of uncertainty reaches up to 30% of the signal strength with largest values in regions in the northern hemisphere. The major source of uncertainty is found to be introduced by wind stress from the atmospheric forcing of the ocean model. In addition, the temporal evolution of the uncertainty in the induced magnetic field shows distinct seasonal variations. Specific regions are identified which are robust with respect to the introduced uncertainties.

1. Introduction

Ocean circulation generates characteristic electromagnetic signals, as the moving salt ions interact with the ambient geomagnetic field. The so-called motionally induced magnetic field is to first order proportional to the conductivity-weighted and depth-integrated ocean velocities [*Sanford*, 1971]. This provides the opportunity to indirectly observe ocean global circulation by measuring the ocean circulation induced magnetic field (e.g., by satellites). Several studies cover the theoretical aspects of the oceanic induced electromagnetic fields, such as *Larsen* [1968], *Sanford* [1971], *Cox* [1980], *Chave* [1983], and *Chave and Luther* [1990]. In more recent studies, the focus is to estimate the strength and the patterns of the motionally induced magnetic field by utilizing ocean models. The modeling of motional induction due to ocean circulation (global and regional) is investigated by, e.g., *Stephenson and Bryan* [1992], *Flosadóttir et al.* [1997], *Tyler et al.* [1997], *Vivier et al.* [2004], and *Manoj et al.* [2006]. In further studies, motional induction due to tidal motion is addressed, e.g., by *Tyler et al.* [2003], *Maus and Kuvshinov* [2004], *Kuvshinov et al.* [2006], *Dostal et al.* [2012], *Schnepf et al.* [2014, 2015], and *Sabaka et al.* [2015]. *Irrgang et al.* [2016] investigate the influence of spatial and temporal variations of seawater conductivity on motional induction due to ocean circulation. The sensitivity experiments demonstrate the need to account for a realistic seawater conductivity distribution. However, the robustness of model-based results of motional induction, i.e., the influence of uncertainties in the modeling approach, has not yet been investigated. Any application of motional induction, e.g., the comparison of model results with observations, feasibility studies, or data assimilation, is only valid if the uncertainty is well characterized [e.g., *Evensen*, 1994]. Uncertainties in the modeling approach can arise from errors in the input data, as well as from errors in the simulation itself. Errors occur due to simplified physics and numerical schemes. Atmospheric forcing reanalysis products are provided by several centers. The discrepancies between the different reanalysis products were analyzed in several recent studies, e.g., *Jakobson et al.* [2012], *Decker et al.* [2012], *Chaudhuri et al.* [2013], and *Kim and Alexander* [2013]. Particularly, wind stress and precipitation fields show nonnegligible discrepancies that can result in large uncertainties in the ocean

circulation [*Chaudhuri et al.*, 2013]. Consequently, the magnetic field, which is induced by ocean circulation, also contains errors due to atmospheric forcing. Additional uncertainties are introduced by errors in the ambient geomagnetic field and in the sediment conductivity, which also arise due to varying modeling approaches [see e.g., *Lowes*, 2000; *Thébault et al.*, 2015] or the application of heuristic methods [e.g., *Everett et al.*, 2003], respectively. Uncertainties in the modeling of the conductivity structure underneath the ocean and oceanic sediments may also influence the modeling of ocean-induced magnetic signals. However, due to the model approach used in this study (see section 2.1.2), the source of uncertainty in the mantle of the Earth is not considered in this study.

In this paper, the robustness of modeling the motionally induced magnetic field is systematically studied by investigating the influence of uncertainties in the modeling approach. This is accomplished by performing a set of ensemble simulations that incorporate different scenarios for error approximations. In this paper, the motionally induced magnetic field is calculated by coupling an ocean global circulation model and an electromagnetic induction model (see section 2.1). The combination of these two models was already used by *Irrgang et al.* [2016] and builds the basis for the ensemble experiments in this study. In particular, the focus of this study lies on magnetic signals, which originate from large-scale ocean circulation patterns and which are apparent at both sea surface and satellite altitude. Both models utilize additional input data, i.e., atmospheric forcing, ambient geomagnetic field, and oceanic sediment conductivity (see section 2.1). The intermediate objectives of this study are (1) the approximation of the major introduced error budgets by error covariance matrices, (2) the calculation of the aggregated uncertainty in the modeling of motional induction, and (3) the identification of spatiotemporal patterns in the motionally induced magnetic field that are robust with respect to introduced uncertainties.

This paper is structured as follows. In section 2, the ocean model and the electromagnetic induction model are described. The setup of the ensemble simulations and the utilized data are depicted and the experiment design is explained (objective 1). The results are presented and discussed in section 3 (objectives 2 and 3). A summary and final conclusions are given in section 4.

2. Methodology

2.1. Model Setup

2.1.1. Global Ocean Model

The global ocean circulation is modeled with the Ocean Model for Circulation and Tides (OMCT) [*Thomas et al.*, 2001]. OMCT is a baroclinic model which incorporates nonlinear balance equations for momentum, the continuity equation, and conservation equations for heat and salt. A resolution of 1.875° in longitude and latitude and 13 layers in the vertical are used. The time stepping is set to 30 min. Additionally, the Boussinesq and the hydrostatic approximations are applied. Artificial mass changes due to the Boussinesq approximation are corrected, as suggested by *Greatbatch* [1994]. The model is forced with heat-flux, wind stress, surface-pressure, precipitation, and evaporation. The forcing is provided by 6-hourly ERA-Interim reanalysis products from the European Centre for Medium-Range Weather Forecasts (ECMWF) [*Dee et al.*, 2011]. Since this study focuses on motional induction due to ocean circulation, ocean tides are not considered in this configuration of the OMCT.

The OMCT is used in several studies [e.g., *Dobslaw and Thomas*, 2007; *Dostal et al.*, 2012; *Dobslaw et al.*, 2013; *Saynisch et al.*, 2014; *Irrgang et al.*, 2016] and is considered to realistically resolve the main features of ocean global circulation. In the current configuration, the OMCT does not resolve small-scale features, which also affect motional induction in the ocean [e.g., *Lilley et al.*, 1993]. However, due to smoothing effects by the upwardly continuation to satellite altitude, small-scale features that are visible in the motionally induced magnetic field at sea surface are blurred with increasing height [*Vennerstrom et al.*, 2005; *Manoj et al.*, 2006]. Therefore, the used resolution is justifiable, since the focus of this study lies on the large-scale features that are apparent at both sea surface and satellite altitude.

2.1.2. Electromagnetic Induction Model

The electromagnetic induction model calculates the radial component of the primary motionally induced poloidal magnetic field. The poloidal component of the motionally induced magnetic field reaches outside the ocean and can be calculated at sea surface and satellite altitude. The focus of this study solely lies on the oceanic induced magnetic signals, which directly originate from large-scale ocean global circulation

and which can, in principle, be measured outside the ocean. Therefore, the primary toroidal component of the oceanic induced magnetic field is not considered in this study, as it is confined to the ocean. Likewise, secondary poloidal magnetic signals, which are generated by coupling effects of the primary toroidal signal and large conductivity contrasts at continental borders [*Dostal et al.*, 2012; *Szuts*, 2010], are not considered.

The model utilizes a 2-D induction equation and follows a similar approach as described in *Vivier et al.* [2004] and *Tyler et al.* [1997]. The ocean basin is approximated by a thin horizontal shell which contains conductivity-weighted and subsequently depth-integrated horizontal ocean flow velocities. Vertical ocean flow velocities are neglected. The atmosphere and upper mantle are treated as insulators [*Vivier et al.*, 2004; *Parkinson and Hutton*, 1989]. The thin shell is allowed to include an underlying layer of conductive sediments. Therefore, a global sediment conductance map has been derived using the method described by *Everett et al.* [2003] and sediment thicknesses obtained from *Laske and Masters* [1997]. Based on Ampere's Law and Ohm's Law, the induced electric currents in the thin shell are given by an electric stream function ψ_e, which leads to a scalar model equation [*Vivier et al.*, 2004]:

$$\nabla \cdot \left(\Sigma^{-1} \nabla \psi_e \right) = \nabla \cdot \left(\Sigma^{-1} F_z \int_h \sigma \boldsymbol{u}_H dz \right). \tag{1}$$

Here h is the variable height of the thin shell according to the bathymetry, Σ is the depth-integrated conductivity of the water column and underlying sediments, σ is the conductivity at a given point (ϕ, ϑ, z), F_z is the radial part of the ambient geomagnetic field, and $\boldsymbol{u}_H$ is the horizontal ocean flow velocity. F_z is derived from the POMME-6 Magnetic Model of the Earth [*Maus et al.*, 2010] and $\boldsymbol{u}_H$ is prognostically calculated with the OMCT. The poloidal oceanic induced magnetic field b_r is derived from the stream function ψ_e using spherical harmonic expansion:

$$b_r(\phi, \vartheta, r) = \sum_{j=0}^{j_{\max}} \sum_{m=-j}^{j} \frac{1}{2} \frac{\mu_0}{r} \psi_{jm} \left(\frac{a}{r} \right)^{j+1} (j+1) Y_{jm}(\phi, \vartheta). \tag{2}$$

Here ϕ and ϑ are longitudinal and colatitudinal coordinates on the sphere, μ_0 is the permeability of free space, a is the Earth's radius, r is the height above sea level, and ψ_{jm} and $Y_{jm}(\phi, \vartheta)$ are the spherical harmonic coefficients and functions. The indices j and m are degree and order of the spherical harmonics. The spherical harmonic coefficients are calculated as described by *Driscoll and Healy* [1994]. The degree and order of the spherical harmonic expansion $j_{\max}$ is limited to 47, in order to prevent aliasing effects due to grid transformations [*Driscoll and Healy*, 1994].

2.2. Ensemble Simulations

The input data that are utilized to initialize and force the two described models contain uncertainty and error correlation. The sources of these uncertainties are manifold and affect both the initial state of the model and the trajectory of the model. To estimate these uncertainties and their effect on the motionally induced magnetic field, an ensemble-based model approach is carried out, as suggested by *Evensen* [1994]. The ensemble members, i.e., the model realizations, differ from each other by the initial OMCT model state x_0, wind stress, geomagnetic field, and sediment conductance (see Figure 1). The spread of the ensemble, i.e., the cross-ensemble variance, arises due to these different initial states and the respective response of the model dynamics to the forcings. The analysis of the ensemble spread allows to quantify amount, spatial patterns, and the temporal evolution of the uncertainty of the motionally induced magnetic field.

The ensemble and its initial spread are generated from the initial model error, which is represented by the error covariance matrix P_0. Since the error covariance matrix of an ocean general circulation model (OGCM) is high-dimensional, a reduced-rank approximation of the error covariance matrix P_0 (in decomposed form) is utilized, i.e.,

$$\tilde{P}_0 := V_0 U_0 V_0^T \approx P_0. \tag{3}$$

This low-rank approximation only considers the r largest eigenmodes of the covariance matrix P_0. More specifically, an error subspace is defined by the most significant directions of uncertainty [*Nerger et al.*, 2005]. Consequently, the $r \times r$ diagonal matrix U_0 contains the r largest eigenvalues of P_0 and the $n \times r$ matrix V_0 contains the corresponding eigenvectors. This projection onto an error subspace allows the usage of (usually) much smaller ensemble sizes to sample P_0 realistically [*Nerger et al.*, 2007]. Consequently, an ensemble
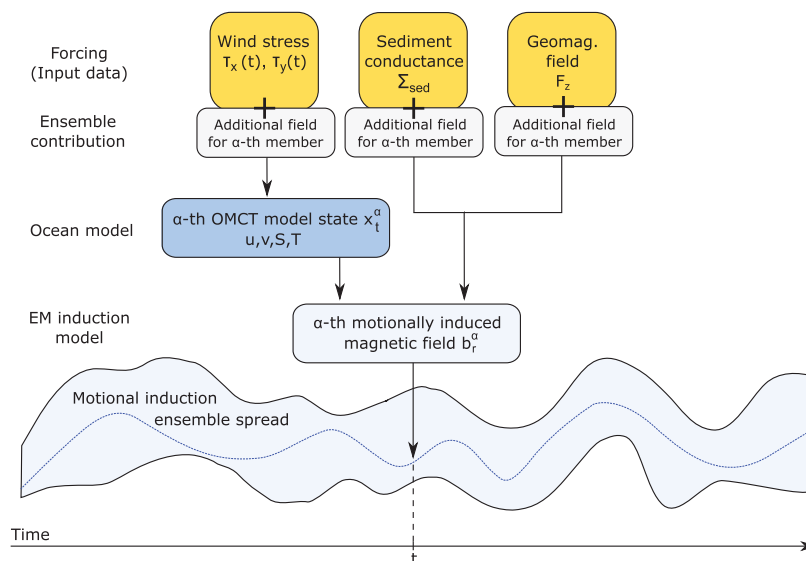
Figure 1. Sketch of the ensemble simulation setup.

$\{x_0^1, \ldots, x_0^{r+1}\}$ of minimum size is generated from the r largest eigenmodes by second-order exact sampling [*Pham*, 2001]:

$$x_0^\alpha = x_0 + \sqrt{r+1}\, V_0 C_0^T (\Omega_0^T)^{(\alpha)}, \tag{4}$$

for $\alpha = 1, \ldots, r+1$. The matrix C_0 is chosen such that $U_0 = C_0^T C_0$ and Ω_0 is a $(r+1) \times r$ random matrix chosen such that the columns are orthonormal to each other and orthogonal to the vector $(1, \ldots, 1)^T$. $(\Omega_0^T)^{(\alpha)}$ is the αth column of Ω_0^T. This construction ensures that the statistics of the ensemble replicate the initial model error (in second-order exact sense), i.e.,

$$\tilde{P}_0 = \frac{1}{r+1} \sum_{\alpha=1}^{r+1} (x_0^\alpha - \overline{x_0^\alpha})(x_0^\alpha - \overline{x_0^\alpha})^T. \tag{5}$$

The cross-ensemble mean $\overline{x_0^\alpha}$ represents the best estimate of the model state. The notation of the ensemble generation follows *Nerger et al.* [2005], who also provide additional information on the mathematical background.

This approach leads to a systematically generated ensemble of model trajectories (see Figure 1). In this study, an ensemble size of 16 is used. Larger ensemble sizes did not change the results. The state vector x_0 is chosen to consist of the following components that are (directly and indirectly) necessary to calculate the motionally induced magnetic field (cf. equation (1)): 3D-fields of zonal ocean flow velocity u, meridional ocean flow velocity v, salinity S, ocean temperature T; and 2D-fields of zonal wind stress τ_x, meridional wind stress τ_y, radial component of the ambient geomagnetic field F_z, and oceanic sediment conductance Σ_{sed} (as a part of Σ). The components u, v, S, and T are dynamically simulated with the OMCT, whereas τ_x, τ_y, F_z, and Σ_{sed} are added via input data. τ_x, τ_y, F_z, and Σ_{sed} are included in the state vector to account for errors in the input data. The forcings (τ_x, τ_y, F_z, and Σ_{sed}) of all ensemble members differ according to equation (4). Consequently, a specific field (depending on the error scenario) is added to the read-in forcings for each ensemble member (see yellow boxes in Figure 1 and *Saynisch et al.* [2014]). τ_x, τ_y, and their errors are assumed to vary in time, whereas F_z, Σ_{sed}, and their errors are assumed to be constant in time. The initial state of each ensemble member is propagated through time with the full nonlinear ocean model and the respective forcings (dark blue box in Figure 1). The initial variance, i.e., the initial spread, of this ensemble equals (in second-order exact sense) to the prescribed uncertainties in P_0 (see error scenarios in the

following section). Note that due to the nonlinearity and internal dynamics of the ocean model, even small differences between the initial state of two ensemble members can eventually lead to very large differences between the two trajectories.

2.3. Experiment Design

The truncated error covariance matrix $\bar{P}_0$ characterizes the main uncertainties in the input data and in the initial state of the ocean model. The estimation of realistic values for $\bar{P}_0$ is a challenge. Therefore, three experiments with different error scenarios, i.e., different error covariance matrices, are performed over the simulation period of 1 year. The wind stress forcing has deficiencies on spatial and temporal scales. Compared to the wind stress values, the errors easily exceed 20% and often reach maxima as large as the modeled stress itself [*Chaudhuri et al.*, 2013]. It is expected to introduce a major source of (temporally variable) error [see also *Saynisch et al.*, 2014].

The first experiment is called ONE-FORC. In ONE-FORC, it is assumed that eventually the atmospheric forcing can be completely wrong. The temporal covariances are calculated from the ERA-Interim atmospheric forcing data for wind stresses τ_x and τ_y. This atmospheric forcing data set is the same that forces the OMCT. Consequently, $\bar{P}_0$ contains the temporal covariances of τ_x and τ_y that force the ocean model.

The second experiment is called TWO-FORC. The Climate Forecast System Reanalysis (CFSR) [*Saha et al.*, 2010] product from the National Centers for Environmental Prediction (NCEP) is used as an additional atmospheric data set. To estimate the errors, the CFSR and the ERA-Interim wind stresses are subtracted from each other to gain a daily data set of differences between the two reanalysis products. Consequently, $\bar{P}_0$ contains the temporal covariances of this data set of differences. Unlike the ONE-FORC experiment, the TWO-FORC experiment also accounts for uncertainties that arise from fundamental distinctions between the two reanalysis products.

ONE-FORC and TWO-FORC are extreme cases of a range of error estimation techniques. Both are commonly used [e.g., *Evensen*, 1994; *Pham et al.*, 1998; *Nerger et al.*, 2006; *Saynisch and Thomas*, 2012; *Saynisch et al.*, 2014].

The third experiment is called NO-FORC. In this experiment, it is assumed that the atmospheric forcing is correct, i.e., no source of error is introduced into the modeling by the atmospheric forcing. Therefore, the NO-FORC experiment describes the influence of uncertainties in the oceanic sediments and in the geomagnetic field in the overall error budget. In contrast to ONE-FORC and TWO-FORC, the added term $\sqrt{r+1}V_0C_0^T$ $(\Omega_0^T)^{(\alpha)}$ in equation (4) is set to zero for the wind stress components τ_x and τ_y in all 16 realizations of the state vector x_0^α. Consequently, the uncertainties in the wind stresses are neither considered for the spanning of the initial state ensemble, nor during the model propagation.

The entries of the error covariance matrices in each experiment vary due to different estimates of uncertainties in the wind stress components of the atmospheric forcing. To account for possible temporal variations in the wind stress uncertainty, the error covariance matrices are computed on a monthly basis for each experiment. Utilizing a single annual error covariance matrix could lead to a wrong ensemble spread. In this case, uncertainties that are only present during a certain time period of the year can influence the spread of the ensemble over the whole simulation period. A set of monthly error covariance matrices allows to estimate the spatial and temporal (e.g., seasonal) occurrence of uncertainties more flexibly and accurately. Each monthly error covariance matrix is calculated from a 3 month time interval of daily anomalies. For example, the error covariance matrix of January is calculated from the temporal covariances of the time interval December–January–February. A 3 month time interval ensures a sufficiently large sample size for the calculation of the temporal covariances. The time intervals of two consecutive error covariance matrices partly coincide. This overlap ensures a smooth transition between the monthly covariances.

The contribution to the uncertainties in F_z and Σ_{sed} is identical for all three experiments. The covariance of F_z is derived from the secular variation of the ambient geomagnetic field. The influence of the uncertainty in the ambient geomagnetic field is considered to be negligible in the context of this study. *Maus et al.* [2010] estimate a root mean square uncertainty of 1.3 nT for the main geomagnetic field (up to 65,000 nT) and 26 nT/a for the secular variation. The authors state that a significant accumulation of these errors and resulting effect on motional induction in the ocean is only expected for longer time scales, e.g., decadal or millennial time scales. Nevertheless, the uncertainty of F_z is considered in order to ensure consistency of the experiment design. For the sediment conductance, few information are available that can be utilized for
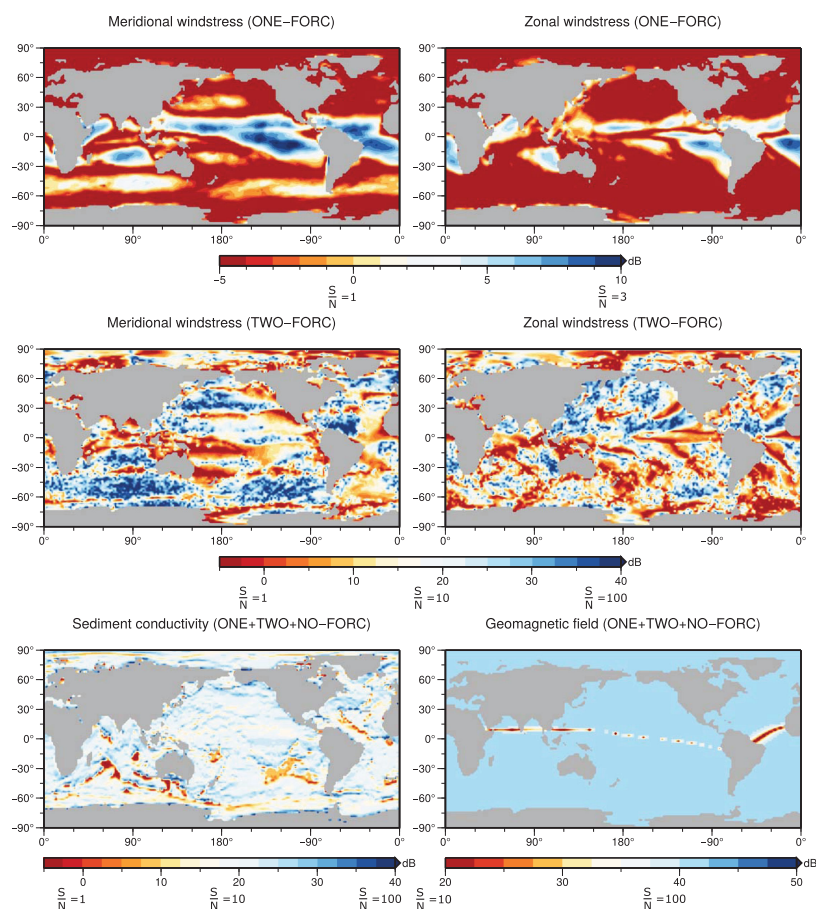
Figure 2. Signal-to-noise ratios (dB) of the estimated uncertainties in the input data used for the January covariance matrices of ONE-FORC, TWO-FORC, and NO-FORC.

estimating the uncertainty. Here five sediment conductivity distributions are mapped to three layers of sediment thicknesses (obtained from *Laske and Masters* [1997]) with respect to the heuristic method described by *Everett et al.* [2003], i.e. (upper layer, middle layer, lower layer): $(0.8, 0.8, 0.02)\,\mathrm{S\,m^{-1}}$, $(0.6, 0.8, 0.02)\,\mathrm{S\,m^{-1}}$, $(0.8, 0.6, 0.02)\,\mathrm{S\,m^{-1}}$, $(0.8, 0.8, 0.01)\,\mathrm{S\,m^{-1}}$ and $(0.7, 0.7, 0.02)\,\mathrm{S\,m^{-1}}$. The results are five different oceanic sediment conductance maps. Next, ten pairwise differences are calculated between the sediment conductance maps. $\tilde{P}_0$ contains the error covariances over these error differences.

The estimated uncertainties in the input data of τ_x, τ_y, F_z, and Σ_{sed} are shown for the January covariance matrices of the ONE-FORC, TWO-FORC, and NO-FORC experiments in Figure 2. The values show signal-to-noise ratios [e.g., *Helstrom et al.*, 2013] between the absolute estimated uncertainty (noise) as described above, and the mean values (signal) of the input data over the 3 month time interval (December–January–February). The signal-to-noise ratios are calculated on a logarithmic scale according to

$$10 \cdot \log_{10}\left(\frac{\mathrm{signal}^2}{\mathrm{noise}^2}\right). \tag{6}$$

In this sense, 0 dB is equivalent to 100% noise, 20 dB is equivalent to 10% noise, and 40 dB is equivalent to 1% noise. In contrast to the calculation of percentage fractions $\frac{\mathrm{noise}}{\mathrm{signal}}$, signal-to-noise ratios circumvent
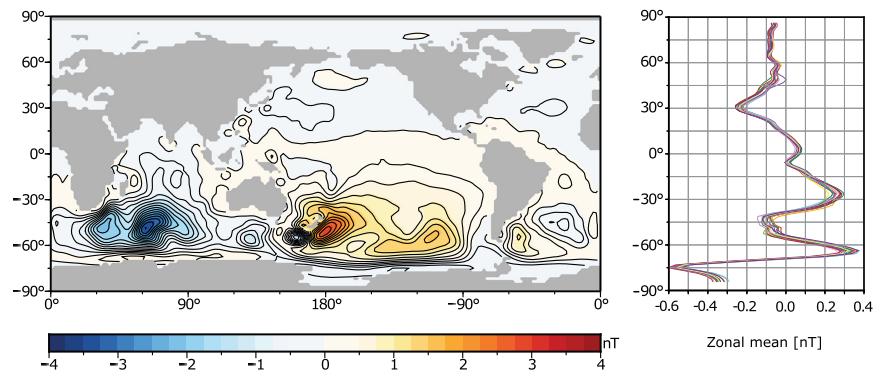
Figure 3. (left) Ensemble mean of the motionally induced magnetic field and (right) zonal mean curves of the 16 motionally induced magnetic field ensemble members of the ONE-FORC experiment. All values are annual mean values at the sea surface (nT).

singularities when the signal strength is equal to zero. On a global scale, the uncertainties in the wind stress of ONE-FORC and TWO-FORC show similar spatial patterns (Figure 2, top and middle). In many regions, the ONE-FORC wind stress uncertainty is 2 orders of magnitude larger than the TWO-FORC uncertainty. Due to the consideration of two different reanalysis data sets, the wind stress uncertainty shows much noisier patterns in TWO-FORC than in ONE-FORC. The estimated wind stress uncertainties derived for the remaining monthly covariance matrices (February–December) differ according to the wind stress dynamics in the respective time intervals. Compared to the wind stress, the uncertainties in the oceanic sediments and in the geomagnetic field are generally low with signal-to-noise ratios mostly below 10% for the oceanic sediments and below 1% for the geomagnetic field (Figure 2, bottom).

Consistent with the atmospheric forcing covariance matrix of January, the uncertainty of the initial state of the OMCT (u, v, S, T) is sampled by the respective covariances from the enclosing time interval December–January–February. The motionally induced magnetic field of each ensemble member and the spread of the ensemble are calculated and stored once per day. The relative amount of uncertainty in the motionally induced magnetic field is calculated by deriving daily signal-to-noise ratios between the ensemble mean of the motionally induced magnetic field (signal) and the ensemble spread (noise).

3. Results and Discussion

3.1. Annual Mean and Maximum Uncertainties

The annual ONE-FORC ensemble mean of the motionally induced magnetic field at the sea surface is depicted in Figure 3 (left). The mean signal strength lies in the range of ± 4 nT and matches with results from previous studies [e.g., *Manoj et al.*, 2006]. The strongest signals are generated by the Antarctic Circumpolar Current in the southern hemisphere. Due to the shape of the radial component of the geomagnetic field of the Earth F_z [e.g., see *Kuvshinov*, 2008, Figure 24], two characteristic large-scale features occur in the South Pacific Ocean (positive values) and in the South Indian Ocean (negative values). To visualize and compare all 16 ensemble members, zonal mean curves are calculated from the 16 annual mean fields. These are depicted in Figure 3 (right) and show the zonally averaged ocean-induced magnetic field of each ensemble member in dependency of the latitude. The zonal mean curves show similar patterns and latitudinal positions of the peak values. However, distinct variations in the peaks of the zonal mean curves are apparent. Additionally, due to the internal dynamics and nonlinearity of the ocean model, the zonal mean curves are not parallel shifted to each other, but strongly interwoven. The zonal mean curves of the ensemble members of the TWO-FORC experiment show similar patterns, but the variations between the zonal mean curves are much smaller (not shown). Hereafter, the causes of these high and low variations in the ONE-FORC and TWO-FORC ensemble spreads are discussed, as well as their spatial distribution and temporal evolution.
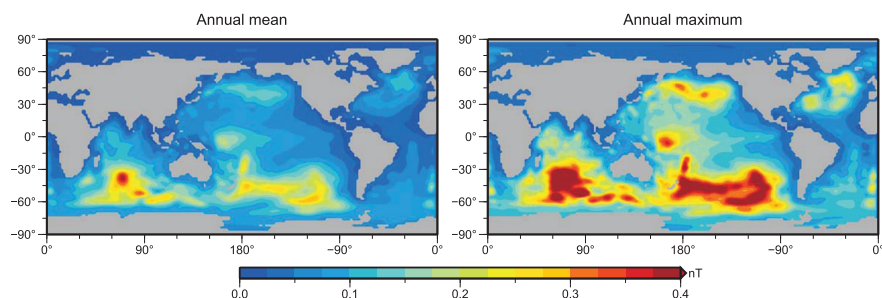
Figure 4. (left) Annual mean and (right) annual maximum ONE-FORC ensemble spread (nT) of the motionally induced magnetic field.

The annual mean and maximum ensemble spreads of the ONE-FORC and the TWO-FORC experiments are shown in Figures 4 and 5. For the sake of comparability, the mean and maximum plots are shown using the same color bar that originates from the respective annual mean value range.

The annual mean ONE-FORC ensemble spread of the motionally induced magnetic field ranges from 0 to 0.4 nT. The highest values occur in the area of the Antarctic Circumpolar Current. More specifically, the areas with the largest ensemble spread occur where also the largest magnetic field strength is generated (compare the left plots of Figures 3 and 4). In the South Pacific Ocean and the South Indian Ocean, large-scale patterns with an ensemble spread between 0.2 and 0.4 nT are visible. Additional features in the range of 0.1 and 0.2 nT occur in the Indian Ocean, east and north-east of Australia, in the North Pacific Ocean (between 30°N and 60°N) and in the North Atlantic Ocean. As shown in Figure 4, the annual mean and maximum values of the ONE-FORC ensemble spread show similar features. However, the values of the annual maximum ensemble spread are much higher and range from 0 to 0.7 nT. Again, the peak values are found in the area of the Antarctic Circumpolar Current with values between 0.3 and 0.7 nT in the South Indian Ocean and between 0.3 and 0.5 nT in the South Pacific Ocean. The features in the Indian Ocean, east and north-east of Australia, in the North Pacific Ocean, and in the North Atlantic Ocean also show relatively high values in the range of 0.25–0.35 nT.

The annual mean and maximum TWO-FORC ensemble spreads show much lower values and different spatial patterns as compared to the ONE-FORC experiment (see Figures 4 and 5). The annual mean ensemble spread of the motionally induced magnetic field ranges from 0 to 0.1 nT. As in the ONE-FORC experiment, the highest values occur in the Antarctic Circumpolar Current. In contrast to the spatial distribution of the ensemble spread in the ONE-FORC experiment (Figure 4, left), the spatial features on the northern hemisphere and in the equatorial region are much more prominent when compared to the strongest features in the area of the Antarctic Circumpolar Current (Figure 5, left). This becomes even more apparent when comparing the annual maximum ensemble spreads of the ONE-FORC and TWO-FORC experiments (right plots of Figures 4 and 5). The strongest features of the maximum TWO-FORC ensemble spread range from 0.1 to 0.15 nT in the western and southern Pacific Ocean and from 0.1 to 0.2 nT in the South Indian Ocean.
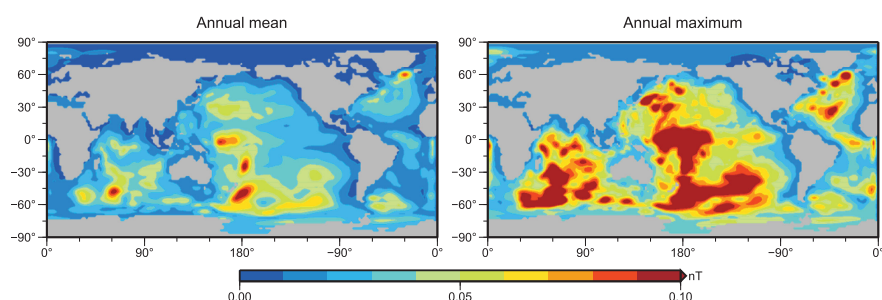

Figure 5. (left) Annual mean and (right) annual maximum TWO-FORC ensemble spread (nT) of the motionally induced magnetic field.
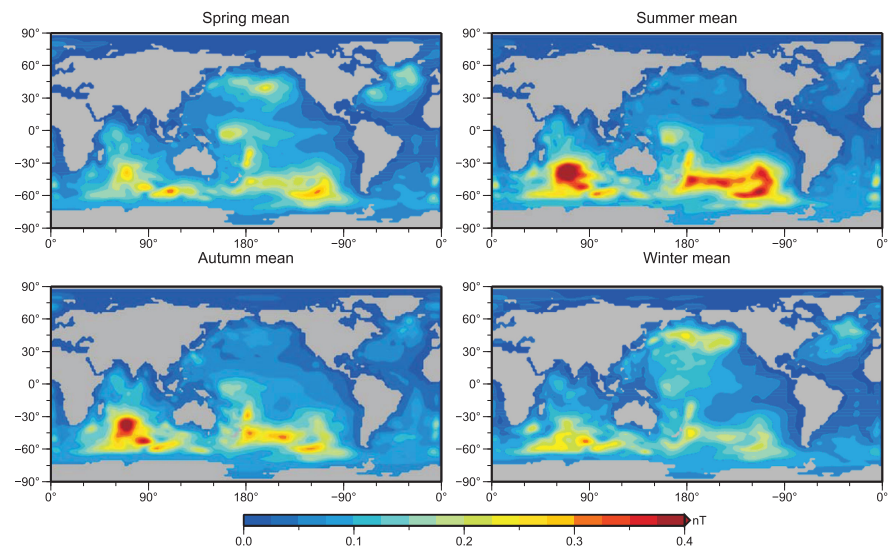
Figure 6. Seasonal mean ONE-FORC ensemble spread (nT) of the motionally induced magnetic field.

In the NO-FORC experiment, the results show only a marginal ensemble spread of the motionally induced magnetic field (not shown). This corresponds to a small influence of the combined uncertainties in the oceanic sediments and in the geomagnetic field on the ocean-induced magnetic field. In many areas, the NO-FORC ensemble spread is 1 order of magnitude smaller than the TWO-FORC ensemble spread. High-value patterns in the NO-FORC ensemble spread lie in the range of 0.02–0.05 nT. In comparison to ONE-FORC and TWO-FORC, the NO-FORC ensemble spread is considered to be negligible.

As a result, it is concluded that uncertainties in the wind stress components of the atmospheric forcing are the major source of the uncertainties in the motionally induced magnetic field (with respect to the considered error budgets, as described in section 2.3).

The differences in the strength and spatial patterns between the ONE-FORC and the TWO-FORC experiments can be explained by the different assumptions for the calculation of the error covariance matrices (see section 2.3 and Figure 2). In the ONE-FORC experiment, the uncertainty in the wind stress is approximated by the temporal variances and covariances of the respective time series. As a consequence, the introduced uncertainties are probably overestimated. In the TWO-FORC experiment, the error covariances are based on the differences between the CFSR and ERA-Interim atmospheric forcing data sets. Ideally, these differences account for various uncertainties in the wind stresses, e.g., errors in the atmospheric modeling, errors due to numerical schemes, errors due to different spatiotemporal availability of observational data, or errors due to different data assimilation schemes. Both the ERA-Interim and the CFSR data sets are reanalysis products that merge atmospheric models and observations. The observations are assimilated by a 4DVar scheme into the ERA-Interim product [*Dee et al.*, 2011] and by a 3DVar scheme into the CFSR product [*Saha et al.*, 2010]. *Decker et al.* [2012] have shown that the two reanalysis products exhibit many differences on varying spatiotemporal scales and, in particular, at regional spatial scales. In principle, large uncertainties in specific regions in the atmospheric forcing can create large uncertainties in the ocean circulation patterns in the respective regions [*Chaudhuri et al.*, 2013]. However, on a global scale and during the considered time scales in this study, the differences between ERA-Interim and CFSR wind stresses in the TWO-FORC experiment lead to a small ensemble spread of the motionally induced magnetic field. The consideration of additional atmospheric forcing data sets could further enhance the error budget and cover more error sources. In this context, the TWO-FORC ensemble spread probably provides an underestimated uncertainty in the motionally induced magnetic field. In summary, it can be concluded that the ONE-FORC and TWO-FORC experiments yield first upper and lower limits (i.e., a reasonable range) of the uncertainty in the motionally induced magnetic field.
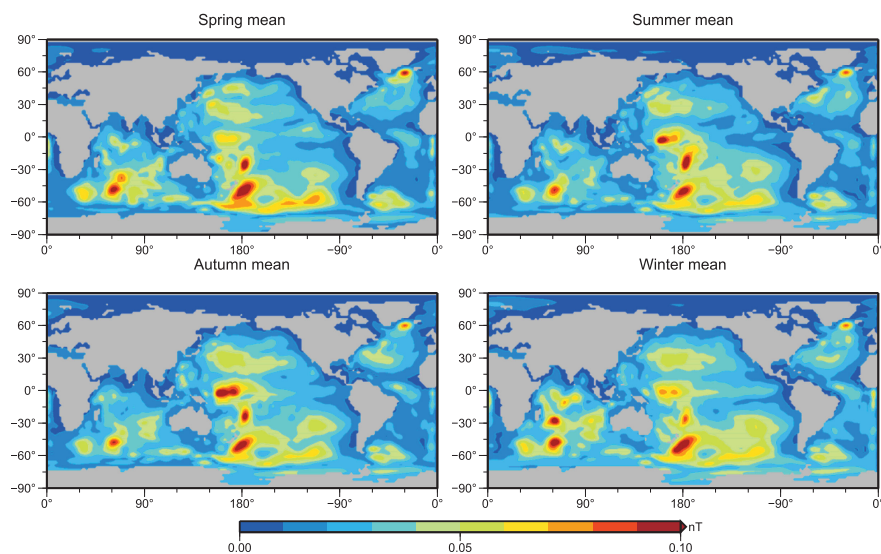
Figure 7. Seasonal mean TWO-FORC ensemble spread (nT) of the motionally induced magnetic field.

3.2. Seasonal Variations in the Uncertainties

The effect of annual and seasonal variations in the introduced uncertainty can also be investigated. The seasonal variations of the ONE-FORC and TWO-FORC ensemble spreads are depicted in Figures 6 and 7. The four plots show mean values over 3 month intervals that are calculated from the daily ensemble spread time series (spring: March–April–May, summer: June–July–August, autumn: September–October–November, and winter: December–January–February).

The ONE-FORC ensemble spread and its spatial distribution show large seasonal variations (Figure 6). The largest values occur in the area of the Antarctic Circumpolar Current during the summer season. Two major patterns are apparent in the South Indian Ocean and in the South Pacific Ocean. In the South Indian Ocean, peak values of up to 0.6 nT occur. In the South Pacific Ocean, the major pattern shows values between 0.2 and 0.4 nT. During the autumn season, the mean ONE-FORC ensemble spread shows a general decrease in the southern hemisphere. The major feature in the South Indian Ocean is still visible and reaches peak values of up to 0.5 nT. In the South Pacific Ocean, peak values up to 0.3 nT occur. The lowest ONE-FORC ensemble spread in the southern hemisphere occurs during the winter season. The major feature that is visible in the South Indian Ocean during the summer and autumn seasons is absent in the winter season. The highest values reach up to 0.3 nT in the South Indian Ocean and up to 0.2 nT in the South Pacific Ocean. In the spring season, the mean ONE-FORC ensemble spread increases again. In contrast to the seasonal changes in the southern hemisphere, the mean ONE-FORC ensemble spread shows converse seasonal variations on the northern hemisphere. The lowest mean ONE-FORC ensemble spread is apparent during the summer season with peak values below 0.1 nT. The highest mean ONE-FORC ensemble spread is visible during the winter season with peak values up to 0.2 nT in the North Pacific Ocean. In summary, the ONE-FORC ensemble spread shows distinct seasonal variations with peak values during the summer season in the southern hemisphere (ACC region) and during the winter season on the northern hemisphere (Kuroshio region).

The TWO-FORC ensemble spread shows a much more static behavior in both the seasonal variations and its spatial distribution (Figure 7). The values for all seasons lie in a comparable range of up to 0.1 nT. In all four seasons, similar patterns with peak values up to 0.1 nT are visible in the South Indian Ocean, south-east of Greenland, and north-east, east, and south-east of Australia. Additional features with values around 0.05 nT are visible throughout all seasons in the Indian Ocean, West Pacific Ocean, South-east Pacific Ocean, North Atlantic Ocean, and east of the Drake passage.
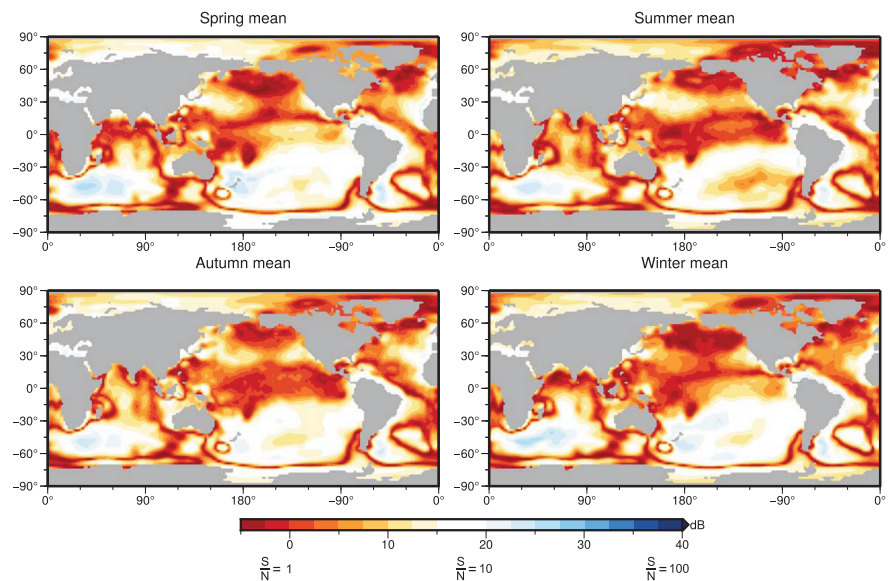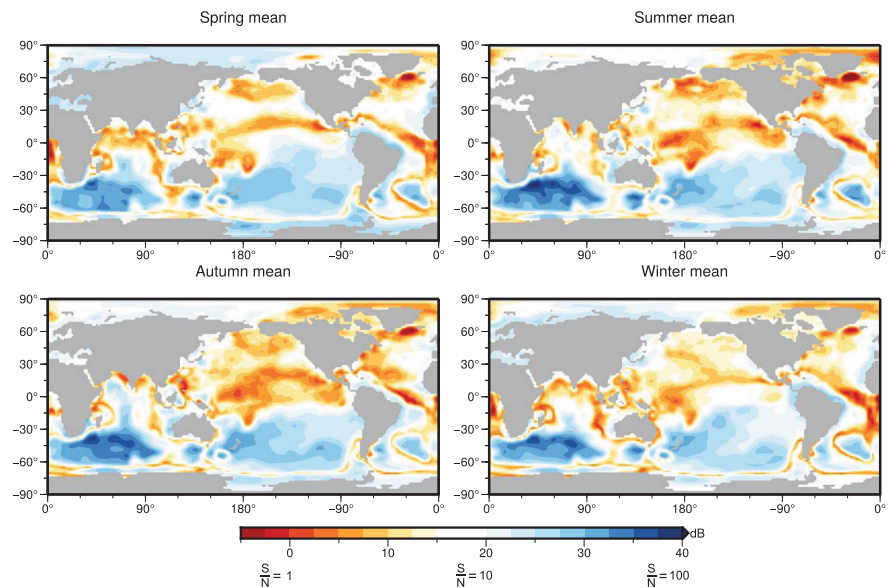
Figure 8. Seasonal mean ONE-FORC signal-to-noise ratio (dB) of the motionally induced magnetic field signal (S) and the ensemble spread (N).

3.3. Signal-To-Noise Ratios of the Motional Induction

In order to put the previously described absolute uncertainty in relation to the motionally induced magnetic field, daily signal-to-noise ratios of the signal strength (Figure 3, left) and the ensemble spreads (Figures 6 and 7) are calculated as described in section 2.3. The signal-to-noise ratios of the ONE-FORC and TWO-FORC experiments are shown in Figures 8 and 9. In accordance with the seasonal depiction of

Figure 9. Seasonal mean TWO-FORC signal-to-noise ratio (dB) of the motionally induced magnetic field signal (S) and the ensemble spread (N).

the ONE-FORC and TWO-FORC ensemble spreads, the signal-to-noise ratios also are subdivided into four seasonal mean maps. Both figures show signal-to-noise ratios of up to 40 dB on a logarithmic scale. High values correspond to a low fraction of noise in the signal, i.e., a small relative ensemble spread. The chosen maximum value of 40 dB corresponds to a signal-to-noise ratio of 100, i.e., a relative uncertainty of 1% in the motionally induced magnetic field. Negative values indicate areas where the ensemble spread is larger than the signal strength.

On a global scale, the seasonal mean ONE-FORC and TWO-FORC signal-to-noise ratios show a distinct partition with low values on the northern hemisphere and high values in the southern hemisphere. This pattern can be explained by the structure of the ocean global circulation induced magnetic field (Figure 3). In particular, the two major features of the motionally induced magnetic field are visible as high-value regions in the South Indian Ocean and in the South Pacific Ocean (compare Figure 3 with Figures 8 and 9). In these areas, the highest signal-to-noise ratios occur.

The highest ONE-FORC signal-to-noise ratios lie in the range from 15 to 25 dB in the South Indian Ocean and from 10 to 25 dB in the South Pacific Ocean (Figure 8). The lowest ONE-FORC signal-to-noise ratios in the range of -5 to 10 dB occur in equatorial regions, North Indian Ocean, North Pacific Ocean, and North Atlantic Ocean. Some regions gain particular interest, as they retain a signal-to-noise ratio of around 20 dB or higher throughout all seasons, i.e., in the South Indian Ocean, around Japan, in the South Pacific Ocean around New Zealand, in the Mediterranean Sea, and east of the Drake Passage.

As described in section 3.2, the TWO-FORC ensemble spread is much smaller than the ONE-FORC ensemble spread. Consequently, higher TWO-FORC signal-to-noise ratios occur in all regions (Figure 9). Peak values in the range of 25–40 dB are found to occur in the South Indian Ocean, South Pacific Ocean, and South Atlantic Ocean. These patterns show a general match with the areas of highest ONE-FORC signal-to-noise ratios in the southern hemisphere. Large-scale features with a low signal-to-noise ratio in the range between 5 and 15 dB are visible in the North Indian Ocean, northern equatorial region of the Atlantic and Pacific Ocean, North Pacific Ocean, and south-east of Greenland. As in the ONE-FORC experiment, some regions retain a low uncertainty throughout the year, e.g., in the South Indian Ocean, in the area of the Kuroshio Current, in the South Pacific Ocean, east of the Drake Passage, and in the South Atlantic Ocean.

The presented results reveal spatiotemporal patterns that are either highly or minimally sensitive toward the introduced uncertainties. Although the ONE-FORC and TWO-FORC ensemble spreads (Figures 6 and 7) show by far the largest range in the area of the Antarctic Circumpolar Current, the ONE-FORC and TWO-FORC signal-to-noise ratios show the lowest amount of noise in these areas (Figures 8 and 9). The exact opposite is found in many regions on the northern hemisphere. These results are due to the spatial distribution of the signal strength of the motionally induced magnetic field (Figure 3). The Antarctic Circumpolar Current is the strongest ocean current and generates the largest magnetic signals (Figure 3). In turn, the large ONE-FORC ensemble spread in these areas (Figure 4) result in a large signal-to-noise ratio of the magnetic field. On the contrary, even the small TWO-FORC ensemble spread (Figure 5) results in a considerable small signal-to-noise ratio of the magnetic field on the northern hemisphere (Figure 9).

The results of this study suggest that the aggregated influence of the various introduced uncertainties on motional induction in the ocean is very diverse. However, despite the varying assumptions for the uncertainty in the atmospheric forcing, the ONE-FORC and TWO-FORC experiments show coinciding regions where the signal-to-noise ratios remain either large or small throughout all seasons. These regions are identified as either nonsensitive or sensitive toward the introduced uncertainties. Especially the nonsensitive areas, i.e., regions in which the uncertainty in the motionally induced magnetic field remains low, are of interest. Regions in which the modeled motionally induced magnetic field is found reliable (within uncertainty limits) allows the most reasonable comparison with observational data. Also the assimilation of observational data into a model is most promising in regions of a low and well-known uncertainty. As described in section 3.1, the derived ONE-FORC and TWO-FORC uncertainties describe upper and lower limits of a realistic range of the uncertainties. In the setting of this study, the main contribution is caused by the wind stress from the atmospheric forcing. To further narrow the presented range of uncertainties, additional constraints for the error budgets in the atmospheric forcing need to be included in the error covariance matrices.

4. Summary and Conclusion

The modeling of the ocean global circulation induced magnetic field is affected by various errors that are introduced through input data and modeling deficiencies. In this study, ensemble simulations over one annual cycle are carried out to estimate the uncertainty in the modeling of the magnetic field that is induced by ocean global circulation. Both spatial patterns and seasonal variations of the uncertainty in the so-called motionally induced magnetic field are investigated. Furthermore, distinct regions are identified in the motionally induced magnetic field, which are only minimally sensitive toward introduced uncertainties.

To calculate the motionally induced magnetic field, a one-sided coupling of an ocean global circulation model and an electromagnetic induction model is used. The initial state and its prescribed uncertainty are assumed to resemble a normal probability density distribution, which is sampled by an ensemble of model realizations. The ensemble mean and spread are generated systematically and approximate the error statistics of the initial probability density distribution. To span this ensemble, error covariance matrices are calculated, which account for error budgets in zonal ocean flow velocity, meridional ocean flow velocity, zonal wind stress, meridional wind stress, ocean temperature, salinity, radial component of the ambient geomagnetic field, and oceanic sediment conductance. The analysis of the ensemble spread allows to investigate the aggregated effect of the introduced uncertainties on the motional induction. In addition, the predominant source of uncertainty is identified.

The global annual mean ensemble spread of the motionally induced magnetic field ranges from 0.1 to 0.4 nT. The largest mean values occur in the area of the Antarctic Circumpolar Current, especially in South Indian Ocean and in the South Pacific Ocean. The largest annual maximum ensemble spread reaches values in the range of 0.2–0.7 nT in the South Indian Ocean. In the South Pacific Ocean, the largest annual maximum ensemble spread reaches values in the range of 0.15–0.5 nT. In these areas, the relative amount of uncertainty (signal-to-noise ratio between the signal strength of the motionally induced magnetic field and its ensemble spread) lies in the range of 1%–10%. However, on the northern hemisphere, the overall smaller ensemble spreads result in much higher signal-to-noise ratios. In particular, large-scale regions with signal-to-noise ratios of 30% or higher occur in the North Indian Ocean, North Pacific Ocean, and North Atlantic Ocean. The described range of uncertainty in the motionally induced magnetic field is found to predominantly originate from the uncertainty in the wind stresses that force the wind-driven ocean circulation.

The experiments demonstrate that the motionally induced magnetic field reacts very sensitively toward introduced uncertainties. Nevertheless, some regions appear to be minimally sensitive, i.e., a small uncertainty is retained throughout all simulation experiments. These regions are found to occur in the South Indian Ocean, South Pacific Ocean, around Japan, and in the South Atlantic Ocean.

Motionally induced magnetic fields may be utilized as indirect observations of ocean global circulation. To understand the spatiotemporal behavior of the induced magnetic field, the numerical modeling of this process is essential. This study highlights that the modeling of motional induction due to ocean global circulation is subject to various errors. For many applications, the knowledge about uncertainties in the modeling is crucial, e.g., the comparison of observational data and model results, or for data assimilation purposes. In this context, the revealed minimally sensitive patterns in the oceanic induced magnetic field may serve as candidate regions for promising future studies of motional induction in the ocean. The inclusion of additional error budgets may further constrain the range of a realistic estimation of the uncertainty in the motionally induced magnetic field (e.g., error information on conductivity structures in the mantle of the Earth).

References

Chaudhuri, A. H., R. M. Ponte, G. Forget, and P. Heimbach (2013), A comparison of atmospheric reanalysis surface products over the ocean and implications for uncertainties in air–sea boundary forcing, *J. Clim.*, 26(1), 153–170, doi:10.1175/JCLI-D-12-00090.1.
Chave, A. D. (1983), On the theory of electromagnetic induction in the Earth by ocean currents, *J. Geophys. Res.*, 88(B4), 3531–3542, doi:10.1029/JB088iB04p03531.
Chave, A. D., and D. S. Luther (1990), Low-frequency, motionally induced electromagnetic fields in the ocean: 1. Theory, *J. Geophys. Res.*, 95(C5), 7185–7200.
Cox, C. S. (1980), Electromagnetic induction in the oceans and interferences on the constitution of the earth, *Surv. Geophys.*, 4, 137–156, doi:10.1007/BF01452963.
Decker, M., M. A. Brunke, Z. Wang, K. Sakaguchi, X. Zeng, and M. G. Bosilovich (2012), Evaluation of the reanalysis products from GSFC, NCEP, and ECMWF using flux tower observations, *J. Clim.*, 25(6), 1916–1944, doi:10.1175/JCLI-D-11-00004.1.

Dee, D. P., et al. (2011), The ERA-Interim reanalysis: Configuration and performance of the data assimilation system, *Q. J. R. Meteorol. Soc.*, *137*(656), 553–597, doi:10.1002/qj.828.

Dobslaw, H., and M. Thomas (2007), Simulation and observation of global ocean mass anomalies, *J. Geophys. Res.*, *112*, C05040, doi: 10.1029/2006JC004035.

Dobslaw, H., F. Flechtner, I. Bergmann-Wolf, C. Dahle, R. Dill, S. Esselborn, I. Sasgen, and M. Thomas (2013), Simulating high-frequency atmosphere-ocean mass variability for dealiasing of satellite gravity observations: AOD1B RL05, *J. Geophys. Res.*, *118*, 3704–3711, doi: 10.1002/jgrc.20271.

Dostal, J., Z. Martinec, and M. Thomas (2012), The modelling of the toroidal magnetic field induced by tidal ocean circulation, *Geophys. J. Int.*, *189*(2), 782–798, doi:10.1111/j.1365-246X.2012.05407.x.

Driscoll, J. R., and D. M. Healy (1994), Computing Fourier transforms and convolutions on the 2-sphere, *Adv. Appl. Math.*, *15*, 202–250, doi: 10.1006/aama.1994.1008.

Evensen, G. (1994), Inverse methods and data assimilation in nonlinear ocean models, *Physica D*, *77*(1–3), 108–129, doi:10.1016/0167-2789(94)90130-9.

Everett, M. E., S. Constable, and C. G. Constable (2003), Effects of near-surface conductance on global satellite induction responses, *Geophys. J. Int.*, *153*(1), 277–286, doi:10.1046/j.1365-246X.2003.01906.x.

Flosadóttir, A. H., J. C. Larsen, and J. T. Smith (1997), Motional induction in North Atlantic circulation models, *J. Geophys. Res.*, *102*(C5), 10,353–10,372, doi:10.1029/96JC03603.

Greatbatch, R. J. (1994), A note on the representation of steric sea level in models that conserve volume rather than mass, *J. Geophys. Res.*, *99*(C6), 12,767–12,771, doi:10.1029/94JC00847.

Helstrom, C., D. Fry, L. Costrell, and K. Kandiah (2013), *Statistical Theory of Signal Detection: International Series of Monographs in Electronics and Instrumentation, Int. Ser. Monogr. Electron. Instrum.*, Elsevier Sci., Amsterdam, Netherlands.

Irrgang, C., J. Saynisch, and M. Thomas (2016), Impact of variable seawater conductivity on motional induction simulated with an ocean general circulation model, *Ocean Sci.*, *12*, 129–136, doi:10.5194/os-12-129-2016.

Jakobson, E., T. Vihma, T. Palo, L. Jakobson, H. Keernik, and J. Jaagus (2012), Validation of atmospheric reanalyses over the central Arctic Ocean, *Geophys. Res. Lett.*, *39*, L10802, doi:10.1029/2012GL051591.

Kim, J.-E., and M. J. Alexander (2013), Tropical precipitation variability and convectively coupled equatorial waves on submonthly time scales in reanalyses and TRMM, *J. Clim.*, *26*(10), 3013–3030, doi:10.1175/JCLI-D-12-00353.1.

Kuvshinov, A. (2008), 3-D global induction in the oceans and solid earth: Recent progress in modeling magnetic and electric fields from sources of magnetospheric, ionospheric and oceanic origin, *Surv. Geophys.*, *29*(2), 139–186, doi:10.1007/s10712-008-9045-z.

Kuvshinov, A., T. Sabaka, and N. Olsen (2006), 3-D electromagnetic induction studies using the Swarm constellation: Mapping conductivity anomalies in the Earth's mantle, *Earth Planets Space*, *58*, 417–427, doi:10.1186/BF03351938.

Larsen, J. C. (1968), Electric and magnetic fields induced by deep sea tides, *Geophys. J. R. Astron. Soc.*, *16*, 47–70, doi:10.1111/j.1365-246X.1968.tb07135.x.

Laske, G., and G. Masters (1997), A global digital map of sediment thickness, *Eos Trans. AGU*, *78*(46), Fall Meet. Suppl., F483.

Lilley, F. E. M., J. H. Filloux, P. J. Mulhearn, and I. J. Ferguson (1993), Magnetic signals from an ocean eddy, *J. Geomagn. Geoelectr.*, *45*(5), 403–422, doi:10.5636/jgg.45.403.

Lowes, F. J. (2000), An estimate of the errors of the IGRF/DGRF fields 1945–2000, *Earth Planets Space*, *52*(12), 1207–1211, doi:10.1186/BF03352353.

Manoj, C., A. Kuvshinov, S. Maus, and H. Lühr (2006), Ocean circulation generated magnetic signals, *Earth Planets Space*, *58*(4), 429–437, doi:10.1186/BF03351939.

Maus, S., and A. Kuvshinov (2004), Ocean tidal signals in observatory and satellite magnetic measurements, *Geophys. Res. Lett.*, *31*, L15313, doi:10.1029/2004GL020090.

Maus, S., C. Manoj, J. Rauberg, I. Michaelis, and H. Lühr (2010), NOAA/NGDC candidate models for the 11th generation International Geomagnetic Reference Field and the concurrent release of the 6th generation Pomme magnetic model, *Earth Planets Space*, *62*(10), 729–735, doi:10.5047/eps.2010.07.006.

Nerger, L., W. Hiller, and J. Schröter (2005), A comparison of error subspace Kalman filters, *Tellus, Ser. A*, *57*(5), 715–735, doi:10.1111/j.1600-0870.2005.00141.x.

Nerger, L., S. Danilov, W. Hiller, and J. Schröter (2006), Using sea-level data to constrain a finite-element primitive-equation ocean model with a local SEIK filter, *Ocean Dyn.*, *56*(5–6), 634–649, doi:10.1007/s10236-006-0083-0.

Nerger, L., S. Danilov, G. Kivman, W. Hiller, and J. Schröter (2007), Data assimilation with the ensemble Kalman filter and the SEIK filter applied to a finite element model of the North Atlantic, *J. Mar. Syst.*, *65*(1–4), 288–298, doi:10.1016/j.jmarsys.2005.06.009.

Parkinson, W. D., and V. R. S. Hutton (1989), *The Electrical Conductivity of the Earth*, vol. 3, pp. 261–232, Academic, San Diego, Calif.

Pham, D. T. (2001), Stochastic methods for sequential data assimilation in strongly nonlinear systems, *Mon. Weather Rev.*, *129*, 1194–1207, doi:10.1175/1520-0493(2001)129 < 1194:SMFSDA>2.0.CO;2.

Pham, D. T., J. Verron, and M. Christine Roubaud (1998), A singular evolutive extended Kalman filter for data assimilation in oceanography, *J. Mar. Syst.*, *16*(3–4), 323–340, doi:10.1016/S0924-7963(97)00109-7.

Sabaka, T. J., N. Olsen, R. H. Tyler, and A. Kuvshinov (2015), CM5, a pre-Swarm comprehensive geomagnetic field model derived from over 12 yr of CHAMP, Orsted, SAC-C and observatory data, *Geophys. J. Int.*, *200*(3), 1596–1626, doi:10.1093/gji/ggu493.

Saha, S., et al. (2010), The NCEP climate forecast system reanalysis, *Bull. Am. Meteorol. Soc.*, *91*(8), 1015–1057, doi:10.1175/2010BAMS3001.1.

Sanford, T. B. (1971), Motionally induced electric and magnetic fields in the sea, *J. Geophys. Res.*, *76*(15), 3476–3492, doi:10.1029/JC076i015p03476.

Saynisch, J., and M. Thomas (2012), Ensemble Kalman-filtering of Earth rotation observations with a global ocean model, *J. Geodyn.*, *62*, 24–29, doi:10.1016/j.jog.2011.10.003.

Saynisch, J., I. Bergmann-Wolf, and M. Thomas (2014), Assimilation of GRACE-derived oceanic mass distributions with a global ocean circulation model, *J. Geod.*, *89*(2), 121–139, doi:10.1007/s00190-014-0766-0.

Schnepf, N. R., C. Manoj, A. Kuvshinov, H. Toh, and S. Maus (2014), Tidal signals in ocean-bottom magnetic measurements of the Northwestern Pacific: Observation versus prediction, *Geophys. J. Int.*, *198*(2), 1096–1110, doi:10.1093/gji/ggu190.

Schnepf, N. R., A. Kuvshinov, and T. Sabaka (2015), Can we probe the conductivity of the lithosphere and upper mantle using satellite tidal magnetic signals?, *Geophys. Res. Lett.*, *42*, 3233–3239, doi:10.1002/2015GL063540.

Stephenson, D., and K. Bryan (1992), Large-scale electric and magnetic fields generated by the oceans, *J. Geophys. Res.*, *97*(C10), 15,467–15,480, doi:10.1029/92JC01400.

Szuts, Z. B. (2010), Relationship between ocean velocity and motionally induced electrical signals: 2. In the presence of sloping topography, *J. Geophys. Res.*, *115*, C06004, doi:10.1029/2009JC006054.

Thébault, E., et al. (2015), Evaluation of candidate geomagnetic field models for IGRF-12, *Earth Planets Space*, *67*(1), 112, doi:10.1186/s40623-015-0273-4.

Thomas, M., J. Sündermann, and E. Maier-Reimer (2001), Consideration of ocean tides in an OGCM and impacts on subseasonal to decadal polar motion excitation, *Geophys. Res. Lett.*, *28*(12), 2457–2460, doi:10.1029/2000GL012234.

Tyler, R. H., L. A. Mysak, and J. M. Oberhuber (1997), Electromagnetic fields generated by a three dimensional global ocean circulation, *J. Geophys. Res.*, *102*(C3), 5531–5551, doi:10.1029/96JC03545.

Tyler, R. H., S. Maus, and H. Lühr (2003), Satellite observations of magnetic fields due to ocean tidal flow, *Science*, *299*(5604), 239–241, doi:10.1126/science.1078074.

Vennerstrom, S., E. Friis-Christensen, H. Lühr, T. Moretto, N. Olsen, C. Manoj, P. Ritter, L. Rastätter, A. Kuvshinov, and S. Maus (2005), The impact of combined magnetic and electric field analysis and of ocean circulation effects on swarm mission performance, technical report, Dan. Natl. Space Cent., Kgs. Lyngby, Denmark.

Vivier, F., E. Meier-Reimer, and R. H. Tyler (2004), Simulations of magnetic fields generated by the Antarctic Circumpolar Current at satellite altitude: Can geomagnetic measurements be used to monitor the flow?, *Geophys. Res. Lett.*, *31*, L10306, doi:10.1029/2004GL019804.

Context

The physical characterization of the ocean circulation induced magnetic field (first study in chapter 2) together with the estimation of the signal uncertainties (second study in chapter 3) form the two main pillars for designing and performing the first motional induction data assimilation experiments. The applied data assimilation technique is based on an ensemble Kalman filter (Kalman, 1960; Evensen, 1994, 2003). Kalman filters utilize statistical and stochastic approaches to correct a numerical model. In contrast to variational data assimilation techniques (e.g., 4DVar, Bouttier and Courtier, 1999), which often rely on the development of an adjoint model, a Kalman filter can be implemented into the motional induction model combination in a convenient way. The combination of the ocean general circulation model and the electromagnetic induction model (chapter 2) is now utilized as an observation operator of motional induction in the assimilation scheme. The ensemble generation is performed by utilizing the monthly error covariance matrices that were calculated in the course of the motional induction uncertainty estimation (chapter 3). Thereby, the new insights from the previous two studies are tied together and allow to conduct motional induction data assimilation experiments.

In contrast to now readily separable satellite observations of the tidal induced magnetic field from both CHAMP (M2 tide, Sabaka et al., 2015) and Swarm satellite data (M2 and N2 tides, Sabaka et al., 2016), it remains a challenge to detect the small and irregular magnetic signals generated by general ocean circulation in satellite observations. So far, this task has not yet been achieved. Since data analysis and extraction of actual satellite observations are not in the scope of this project, the lack of data availability is circumvented by creating a set of model-based artificial and idealized observations of the ocean circulation induced magnetic field at satellite altitude. These artificial observations only consider the oceanic contribution to the magnetic field at satellite altitude, assuming a nearly error-free separability from other magnetic field constituents. These so-called synthetic observations are utilized in the third study, which is presented in the following chapter 4. The study design yields several advantages.

First, the principle feasibility of assimilating motional induction satellite observations

into an ocean general circulation model and the corresponding impact on the ocean model state can be investigated in a controlled environment. This is essential, as there exist no published studies on the assimilation of electromagnetic induction signals into an ocean model. The possible amount of improvement of an ocean model state due to the assimilation of induced electromagnetic signals is unknown.

Second, the performance of the data assimilation can be accurately measured in a model-based twin experiment. Since the synthetic observations are drawn from a model-based representation of the true ocean state, the impact of the assimilation scheme on the individual ocean state variables, e.g., zonal and meridional velocities, oceanic heat and salinity distributions, can be calculated. This is of specific interest, as the induced magnetic field signals are solely a proportionality measure for conductivity-weighted and depth-integrated ocean velocities (Sanford, 1971). It will be shown that this leads to a systematic trade-off between improving the ocean model state in the sense of optimally recovering the depth-integrated and conductivity-weighted velocities and in the sense of optimally recovering the individual components of the ocean model state, i.e., ocean velocities, temperature, and salinity.

Third, since all assimilation parameters and model variables are known in a twin experiment with synthetic observations, this setup could also be used to determine minimum requirements for the quality of actual future satellite observations that are necessary for a successful data assimilation (e.g., spatial and temporal resolution, measurement precision, sources of uncertainties, etc.). These potential requirements are important for separating the ocean induced magnetic field contribution from other magnetic field sources in magnetic field observations. Therefore, model-based studies as in the following chapter help to accelerate the ongoing efforts to also detect ocean circulation induced magnetic signals in satellite observations.

4

Utilizing oceanic electromagnetic induction to constrain an ocean general circulation model: A data assimilation twin experiment

Chapter Abstract

Satellite observations of the magnetic field induced by the general ocean circulation could provide new constraints on global oceanic water and heat transports. This opportunity is investigated in a model-based twin experiment by assimilating synthetic satellite observations of the ocean-induced magnetic field into a global ocean model. The general circulation of the world ocean is simulated over the period of one month. Idealized daily observations are generated from this simulation by calculating the ocean-induced magnetic field at 450 km altitude and disturbing these global fields with error estimates. Utilizing an ensemble Kalman filter, the observations are assimilated into the same ocean model with a different initial state and different atmospheric forcing. Compared to a reference simulation without data assimilation, the corrected ocean-induced magnetic field is improved throughout the whole simulation period and over large regions. The global RMS differences of the ocean-induced magnetic field are reduced by up to 17 %. Local improvements show values up to 54 %. RMS differences of the depth-integrated zonal and meridional ocean velocities are improved by up to 7 % globally, and up to 50 % locally. False corrections of the ocean model state are identified in the South Pacific Ocean and are linked to a deficient estimation of the ocean model error covariance matrices. Most Kalman filter induced changes in the ocean velocities extend from the sea-surface down to the deep ocean. Allowing the Kalman filter to correct the wind stress forcing of the ocean model is essential for a successful assimilation.

4.1   Introduction

Electromagnetic induction in the ocean arises from interactions between the highly conducting salt-water and the ambient geomagnetic field. Sanford (1971) showed that these motionally induced magnetic signals are to first order proportional to the conductivity-weighted and depth-integrated ocean velocities. Measurements (e.g., by satellites) of the induced magnetic signals could serve as additional observations of the general ocean circulation and provide a new opportunity to constrain oceanic water, heat, and salinity transports in ocean models.

Based on the early pioneering work of Larsen (1968), Sanford (1971), Cox (1981), Chave (1983), and Chave and Luther (1990), several studies were conducted during the last two decades that aimed to characterize both tide and circulation induced magnetic fields by using ocean models. Among others, electromagnetic induction due to the general ocean circulation was investigated by Stephenson and Bryan (1992), Flosadóttir et al. (1997), Tyler et al. (1997), Vivier et al. (2004), Manoj et al. (2006), and Irrgang et al. (2016a). Since tidal induced magnetic signals are now readily extracted from satellite measurements (Tyler et al. (2003), Sabaka et al. (2016)), practical applications of these signals were investigated, e.g., probing the conductivity of the lithosphere (Schnepf et al. (2015)) and detecting long-term changes in the sea-water conductivity due to climate variability (Saynisch et al. (2016)). The influence of uncertainties and erroneous input data on the modelling of electromagnetic induction in the ocean was recently analyzed by Irrgang et al. (2016b).

In this study, we explore a new application of oceanic electromagnetic induction, i.e., the correction of an ocean general circulation model by assimilating satellite observations of the ocean-induced magnetic field. This is especially rewarding for ocean modelling, since potential magnetic field satellite observations provide integrated information about ocean flow from the sea surface down to the bottom of the ocean.

ESA's Swarm mission measures the magnetic field of the Earth with unprecedented precision. The detection of signals from the general ocean circulation was defined in the Swarm research objectives (Friis-Christensen et al. (2006)). However, in contrast to the easier detectable tidal magnetic field (Sabaka et al. (2016)), ocean circulation induced magnetic signals have not yet been extracted from satellite observations (a review was presented by Kuvshinov (2008)). Additionally, it is unknown, whether such satellite observations depict suitable constraints for ocean models, since small-scale features of the smoothed ocean-induced magnetic field are not visible at satellite altitude (Manoj et al. (2006)).

A model-based twin experiment is conducted in this study to investigate the potential of assimilating ocean-induced magnetic field satellite observations into an ocean general

circulation model. For this, it is assumed that a processed and idealized data product with motional induction satellite observations exists. The ocean model together with an electromagnetic induction model are utilized to generate a set of synthetic, i.e., artificial, and idealized observations in the form of global fields. The observations are disturbed with Gaussian white noise. The data assimilation is performed with an ensemble-based Kalman filter. The calculation of the ocean model error covariance matrices bases on the findings of Irrgang et al. (2016b), whereas the observation error covariance matrix is estimated from the observation noise level based on the nominal Swarm precision of 0.1 nT (Friis-Christensen et al. (2006), Olsen et al. (2006)). The impact of the assimilation on the model trajectories is quantified with respect to an unconstrained forward simulation. This experiment setup allows to analyze and to quantify the Kalman filter impact on the individual components of the ocean model state in a consistent way. Additionally, problems arising due to the data assimilation are identified and discussed.

This paper is structured as follows. In section 4.2, the numerical models are described. The twin experiment setup together with the utilized data assimilation scheme and the generation of the synthetic observations are illustrated. In section 4.3, the performance of the data assimilation and the impact on the model results are presented and discussed. In section 4.4, a summary and conclusions are given.

4.2   Methodology

4.2.1   Model setup

4.2.1.1   Global Ocean model

The general circulation of the world ocean is simulated with the Ocean Model for Circulation and Tides (OMCT, Thomas et al. (2001)). OMCT is a baroclinic free-surface ocean model and bases on non-linear balance equations for momentum, the continuity equation and conservation equations for salt and heat. The hydrostatic and the Boussinesq approximations are applied. Artificial mass change caused by the Boussinesq approximation is corrected as proposed by Greatbatch (1994). According to K-theory, a turbulence closure scheme is applied by specifying horizontal eddy diffusivity and vertical eddy viscosity constants, respectively. The longitudinal and latitudinal resolution is 1.875°. OMCT is a z-model and the vertical is resolved by 13 layers. A time step of 30 minutes is used. OMCT is forced with wind stress, surface pressure, heat flux, precipitation, and evaporation. The forcing data is derived from 6-hourly ERA-Interim reanalysis products provided by the European Centre for Medium-Range Weather Forecasts (ECMWF, Dee et al. (2011)). Ocean tides are not simulated with the used configuration of the model.

In recent studies, OMCT has been used for various purposes (e.g., Dobslaw and Thomas (2007), Dobslaw et al. (2013), Saynisch et al. (2014), Irrgang et al. (2016a)) and it realistically resolves the main features of the general ocean circulation. Additionally, OMCT is suitable for simulating short times-scales. The model has been operatively used to simulate sub-monthly ocean bottom pressure anomalies for de-aliasing gravity observations from the GRACE (Gravity Recovery And Climate Experiment) satellites (Dobslaw et al. (2013)). The effect of small-scale features in the ocean circulation on the ocean-induced magnetic field (e.g., Lilley et al. (1993)) is not reproduced by the current version of OMCT. However, since the aim of this study is the assimilation of synthetic magnetic field observations at satellite altitude, the resolution of the used models is sufficiently large. Any small-scale features that are present in the ocean-induced magnetic field near the sea surface are blurred with increasing height due to the smoothing effect by the upwardly continuation of the induced signal (Vennerstrom et al. (2005), Manoj et al. (2006)).

4.2.1.2   Electromagnetic induction model

The electromagnetic induction model is used to derive synthetic observations of the ocean-induced magnetic field at satellite altitude (see section 4.2.2.3). In the data assimilation scheme it is applied as a global observation operator of the general ocean circulation (see section 4.2.2.2). The model calculates the radial component of the primary ocean-induced poloidal magnetic field, which is generated by the large-scale horizontal ocean circulation and emitted outside of the ocean. The primary toroidal ocean-induced magnetic field component (Chave (1983)) and secondary poloidal magnetic signals near continental borders (Szuts (2010), Dostal et al. (2012)) are not considered in this model.

Based on a 2-D induction equation as described by Tyler et al. (1997) and Vivier et al. (2004), the electromagnetic induction source is calculated in a thin-shell approximation of the ocean basin. This thin shell only contains conductivity-weighted and depth-integrated horizontal ocean velocities and induced electric currents. Vertical ocean flow is neglected in this approach. The thin shell is supplemented by an underlying layer of conductive ocean sediments, whereas the atmosphere and upper mantle are treated as insulators (Parkinson and Hutton (1989), Vivier et al. (2004)). The layer of conductive ocean sediments is derived by applying a heuristic method described by Everett et al. (2003) to the sediment thickness maps of Laske and Masters (1997).

In the thin shell, Ampere's Law and Ohm's Law are simplified and induced horizontal electric currents can be expressed by an electric stream function ψ_e (Vivier et al. (2004)),

which is calculated from the scalar model equation

$$\nabla \cdot \left(\Sigma^{-1} \nabla \psi_e \right) = \nabla \cdot \left(\Sigma^{-1} F_r \int_h \sigma \boldsymbol{u}_H dr \right) . \tag{4.1}$$

Here, h is the variable thickness of the thin shell according to the bathymetry, Σ is the depth-integrated conductivity of the water column and underlying sediments, σ is the conductivity at a given point (ϕ, ϑ, z), F_r is the radial part of the ambient geomagnetic field and $\boldsymbol{u}_H$ is the horizontal ocean flow velocity. F_r is derived from the POMME-6 Magnetic Model of the Earth (Maus et al. (2010)) and $\boldsymbol{u}_H$ is prognostically calculated with OMCT. The ocean-induced magnetic field $\boldsymbol{b}$ is expressed by the gradient of a potential field P as

$$\boldsymbol{b} = -\nabla P . \tag{4.2}$$

Given the non-divergence of the ocean-induced magnetic field, $\nabla \cdot \boldsymbol{b} = 0$, P can be derived from ψ_e through a boundary value problem, i.e.,

$$\nabla^2 P(\phi, \vartheta, r) = 0 , \tag{4.3}$$

$$P(\phi, \vartheta, \infty) = 0 , \tag{4.4}$$

$$P(\phi, \vartheta, a + \zeta) = -\frac{1}{2} \mu_0 \psi_e(\phi, \vartheta) , \tag{4.5}$$

where a is the Earth's radius, and ζ is the sea surface height. The solution for P is given by a spherical harmonics expansion according to

$$P(\phi, \vartheta, r) = -\sum_{j=0}^{\infty} \sum_{m=-j}^{j} \frac{1}{2} \mu_0 \psi_{jm} \left(\frac{a}{r} \right)^{j+1} Y_{jm}(\phi, \vartheta) . \tag{4.6}$$

Here, ϕ and ϑ are longitudinal and colatitudinal coordinates on the sphere, μ_0 is the permeability of free space, a is the Earth's radius, r is the height above sea level, ψ_{jm} and $Y_{jm}(\phi, \vartheta)$ are the spherical harmonic coefficients and functions, respectively. The indices j and m are degree and order of the spherical harmonics. The global radial component b_r of the ocean-induced magnetic field at satellite altitude is derived from the upwardly continuation of P to satellite altitude by

$$b_r(\phi, \vartheta, r) = \frac{\partial}{\partial r} P(\phi, \vartheta, r) \tag{4.7}$$

$$= \sum_{j=0}^{j_{\max}} \sum_{m=-j}^{j} \frac{1}{2} \frac{\mu_0}{r} \psi_{jm} \left(\frac{a}{r} \right)^{j+1} (j+1) Y_{jm}(\phi, \vartheta) . \tag{4.8}$$

As described in Irrgang et al. (2016a), the maximum degree j_{max} of the spherical harmonics expansion is limited to 47 in order to prevent aliasing artefacts during the grid

transformations.

4.2.2   Data assimilation

4.2.2.1   Kalman filter

Data assimilation aims to combine a numerically calculated state forecast x^f of a geophysical system with observational data y. Kalman filters (Kalman (1960)) form one class of data assimilation techniques that sequentially assimilate observations into a model at the time they become available. At a time t where observations y_t are present, an analyzed state x_t^a is calculated by

$$x_t^a = x_t^f + K_t \left(y_t - H \left[x_t^f \right] \right) \ . \tag{4.9}$$

H is the observation operator that projects the estimated state x_t^f into the observation space of y_t. Here, H is the electromagnetic induction model that calculates the ocean-induced magnetic field for the state x_t^f at satellite altitude (see section 4.2.2.3). The matrix K_t is the Kalman gain at time t that depends on the error covariance matrices, i.e, uncertainty information, of the ocean model (P_t) and of the observations (R_t). Accordingly, a small (large) observation residual $y_t - H[x_t^f]$ results in a small (large) update of the model state x_t^f, which is weighted by the combined uncertainty information. Subsequently, the analyzed state x_t^a is propagated through time with the numerical model until the next observation is available (forecast phase).

In oceanography, data assimilation typically is a high-dimensional problem that involves state forecasts from non-linear models with several thousand entries and cost-expensive inversions of the respective error covariance matrices. Therefore, ensemble Kalman filters (Evensen (1994), Evensen (2003)) and their error subspace variants (a description and comparison are presented in Nerger et al. (2005a)) are commonly used for efficiently assimilating observations with non-linear and high-dimensional numerical models (e.g., Pham et al. (1998a), Pham (2001), Saynisch and Thomas (2012), Saynisch et al. (2014)).

In this study, we use the localized error subspace transform Kalman filter (LESTKF, Nerger et al. (2012a)) from the parallel data assimilation framework (PDAF, Nerger et al. (2005b)). The LESTKF is an error subspace ensemble Kalman filter and was constructed as a variant of the singular evolutive interpolated Kalman filter (SEIK, Pham et al. (1998b)) that performs minimum ensemble member transformations in the assimilation step. The exact formalism of equation 4.9 in the LESTKF is given by Nerger et al. (2012a).

The state forecast x^f contains six components that can be adjusted by the Kalman filter: 3-D fields of zonal (u) and meridional (v) ocean velocities, ocean temperature (T),

ocean salinity (S); and 2-D fields of zonal (τ_x) and meridional (τ_y) wind stress forcing. During the forecast phase, the variables u, v, S, T are prognostically calculated with the OMCT, whereas τ_x and τ_y are read in from input data (see also section 4.2.1.1). Since Irrgang et al. (2016b) showed that errors in the wind stress forcing have a major impact on the ocean-induced magnetic field, the forcing fields τ_x and τ_y are also allowed to be adjusted in the assimilation step.

The initial state x_0^f and the uncertainty P_0 for the simulated month January are sampled by a 32-member ensemble, which is created by second-order exact sampling (Pham (2001)). Larger ensemble sizes did not change the results of this study. The ensemble is generated such that the cross-ensemble variance represents the initial uncertainty provided by the error covariances in P_0. The ensemble members differ from each other by the initial OMCT state and by the wind stress of the atmospheric forcing. A detailed description of the ensemble generation and the calculation of the initial error covariance matrix P_0 is presented by Irrgang et al. (2016b) and is adopted for this study. The observation error covariance matrix is chosen to be a time-invariant diagonal matrix, i.e., $R_t = R$. The variances on the diagonal of R are derived from the estimated error in the synthetic satellite observations (see section 4.2.2.3). All ensemble members are propagated through time independently with the non-linear ocean model until a new observation is available. After this forecast phase, the assimilation step (equation 4.9) is performed on the cross-ensemble mean $\overline{x_t^f}$.

Localized Kalman filters as LESTKF are based on the assumption that only observations in close proximity to the currently analyzed grid point, or region, have an influence on the assimilation update (e.g., Evensen (2003)). Therefore, both the mean state forecast $\overline{x_t^f}$ and the observation vector y_t are decomposed into local components before the assimilation step. The localization used in this version of LESTKF subdivides the ocean basin into disjoint vertical columns ($1 \times 1 \times$ number of vertical grid points). The number of vertical columns is equal to the number of sea surface grid points. Each local state consists of one vertical ocean column and the corresponding values of the wind stresses τ_x and τ_y. The local state vectors are updated independently in the assimilation step according to equation 4.9. Although the ocean-induced magnetic field at satellite altitude is in principal non-local (due to the upwardly continuation, see section 4.2.1.2), the large-scale spatial distribution remains very similar to the magnetic field signals at the sea surface. On this basis, a quasi-local correspondence between the observed ocean-induced magnetic signal at a given location and the oceanic transport underneath is assumed. The observation y_t is localized for each local state by restricting the global observation field (see section 4.2.2.3) to a circular subset with a radius of 8 grid points and its center located at the sea surface grid point of the local state. From a range of tested radii, the chosen
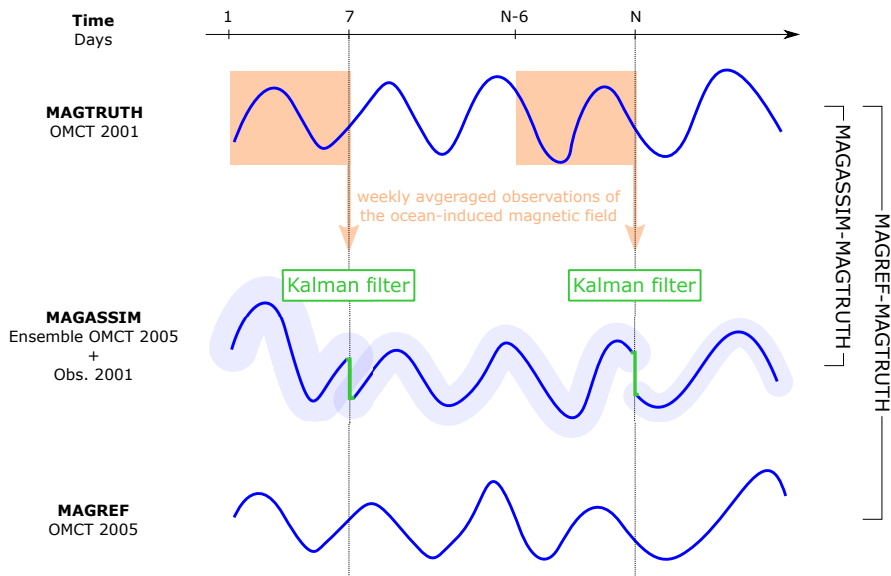
Figure 4.1: Sketch of the data assimilation twin experiment. The blue curves represent OMCT state trajectories. The synthetic observations are generated from MAGTRUTH and assimilated into MAGASSIM. MAGREF is a reference simulation without data assimilation. To evaluate the performance of the Kalman filter, the differences MAGASSIM minus MAGTRUTH and MAGREF minus MAGTRUTH are compared.

radius of 8 grid points provides the highest Kalman filter improvements. Consequently, the localized observations of two neighbouring local states largely overlap. This ensures a smooth transition between the analyzed local states and the global analyzed state. After all local states have been updated by the Kalman filter, the global analyzed mean state $\overline{x_t^a}$ is re-assembled from the local analyzed state vectors and the ensemble is updated. Subsequently, the next forecast phase starts. A detailed formulation of the localization scheme is presented by Nerger et al. (2012b).

4.2.2.2   Twin experiment setup

A model-based twin experiment is performed to investigate the performance of the data assimilation. The experiment setup is shown in Fig. 4.1 and consists of three OMCT state trajectories with a length of one month. Snapshots, i.e., instantaneous values, of the ocean-induced magnetic field, ocean velocities, temperature and salinity are stored once per day for all simulations.

The first simulation is called MAGTRUTH and simulates January of 2001. MAG-TRUTH represents the true state of the general ocean circulation in January. The synthetic satellite measurements of the ocean-induced magnetic field are generated from MAGTRUTH once per day (details follow in section 4.2.2.3). These observations are the only information, which are derived and utilized from the known true state of the general
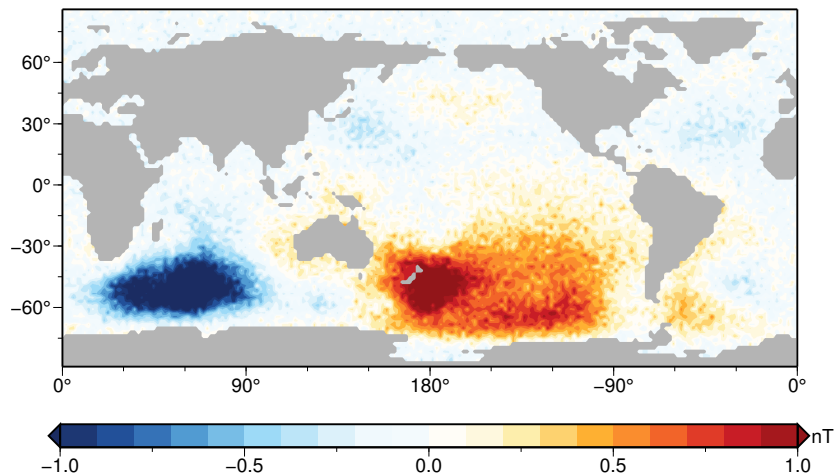
Figure 4.2: Synthetic observation field of the ocean-induced magnetic field. The map shows mean values over one week at satellite altitude (450 km) disturbed with uncorrelated Gaussian white noise (0.1 nT standard deviation).

ocean circulation.

MAGREF represents a known unconstrained state of the general ocean circulation in January and serves as a reference simulation without data assimilation. The deviations in MAGREF from MAGTRUTH are generated by simulating the same time period of a different year, i.e., January 2005. Consequently, the deviations between MAGTRUTH and MAGREF result from different initial OMCT states and by the different responses of OMCT to the atmospheric forcing of the respective time periods (2001 versus 2005). The differences in the OMCT states between MAGREF and MAGTRUTH (MAGREF-MAGTRUTH) represent the error made by the ocean model to replicate the true prior state of the ocean.

To visualize the different ocean model states of MAGTRUTH and MAGREF, vector plots of both conductivity-weighted and depth-integrated ocean velocities and surface velocities are shown in Fig. 4.3. The depicted monthly mean flows show distinct variations between the large-scale currents of both simulations. These are visible in all major depth-integrated ocean velocities, e.g., in western boundary currents, and in the Antarctic Circumpolar Current, but also in equatorial surface currents.

MAGASSIM is the simulation with data assimilation and aims to recover the true ocean state and ocean-induced magnetic field of MAGTRUTH. MAGASSIM has the same initial OMCT state and forcing as MAGREF. Starting from day 7, the synthetic satellite observations from MAGTRUTH are assimilated into MAGASSIM once per day. The differences in the OMCT states between MAGASSIM and MAGTRUTH (MAGASSIM-MAGTRUTH) represent the error between the corrected ocean model and the true prior state of the ocean (see also Fig. 4.3).
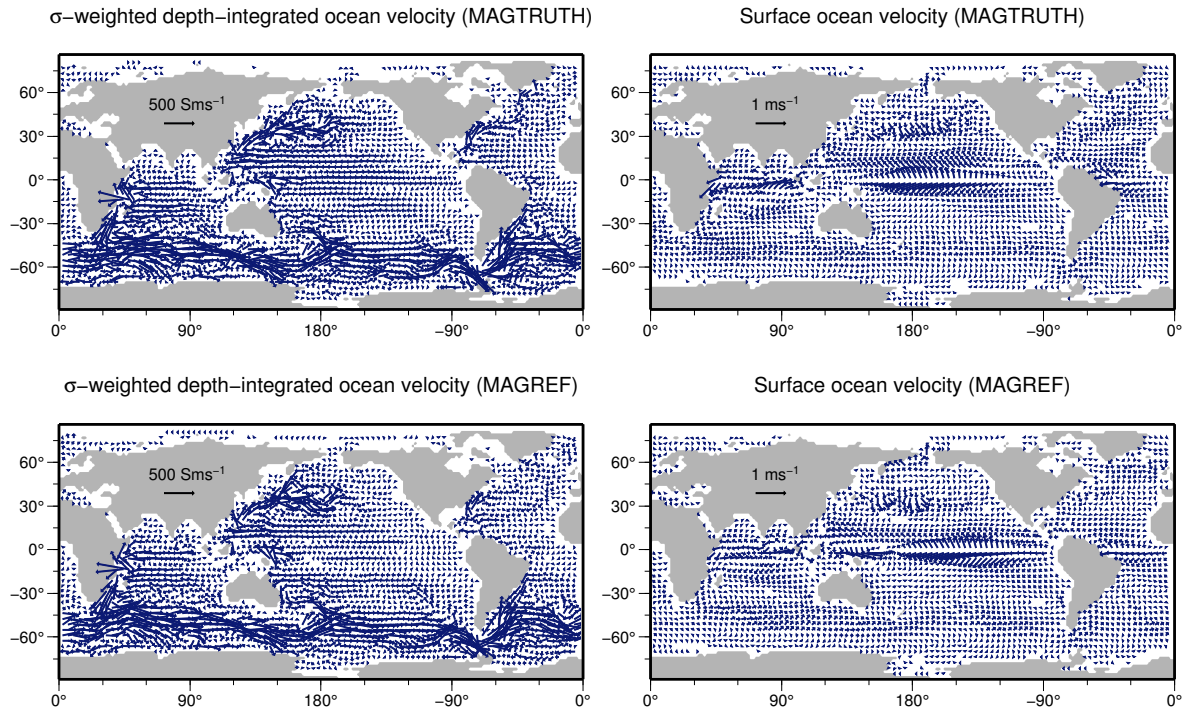
Figure 4.3: Ocean velocity vector plots of MAGTRUTH and of MAGREF at selected grid points. The left column shows conductivity-weighted and depth-integrated ocean velocities, the right column shows surface velocities of MAGTRUTH and MAGREF, respectively. Arrow lengths are mean values over the one month simulation time period.

As in a real-world data assimilation experiment with actual satellite observations of the ocean-induced magnetic field, it is assumed that the initial error covariance matrix P_0 of the ocean model in MAGASSIM is unknown and has to be estimated. For this, we utilize the common approach to estimate P_0 through the respective temporal variations of forward simulations during the considered time period (e.g., Evensen (1994)). Irrgang et al. (2016b) calculated monthly error covariance matrices for each month of the year 2005. Accordingly, for this data assimilation experiment the previously calculated error covariance matrix for the month January of 2005 is applied, which includes uncertainty estimates for the ocean model state (u, v, S, T), and for the atmospheric wind stress forcing (τ_x, τ_y). Consequently, this a-priori estimation of P_0 is independent from the differences between the false and true ocean model states (MAGREF-MAGTRUTH), and solely the synthetic satellite observations from MAGTRUTH (see Sec. 4.2.2.3) are utilized to provide information about the known true ocean state.

Due to the twin experiment setup, the deviations between MAGASSIM-MAGTRUTH and MAGREF-MAGTRUTH are a measure of the performance of the data assimilation. A decrease in MAGASSIM-MAGTRUTH compared to MAGREF-MAGTRUTH means a success of the data assimilation, i.e., the corrected ocean model recovers the known truth better than the reference, and vice versa. The choice of the years 2001 and 2005, i.e., the

choice of true and false realizations of the general ocean circulation, is arbitrary and can also be made differently (e.g., Saynisch et al. (2015)).

4.2.2.3 Synthetic satellite observations

The Swarm satellite trio measures the Earth's magnetic field with unprecedented precision and the detection of the general ocean circulation by its small induced magnetic signals was defined as one of the Swarm research objectives (Friis-Christensen et al. (2006)). Since Tyler et al. (2003) demonstrated the possibility to identify tidal (M2) magnetic signals in CHAMP satellite observations, several subsequent studies were performed to further characterize and utilize tide and circulation induced magnetic signals (e.g., Maus and Kuvshinov (2004), Manoj et al. (2006), Schnepf et al. (2015), Grayver et al. (2016), Irrgang et al. (2016a), Irrgang et al. (2016b)). Recently, Sabaka et al. (2016) extracted the M2 and N2 ocean tide from 20.5 months of Swarm data. However, it remains a challenge to extract general circulation induced magnetic signals from satellite observations (see also Kuvshinov (2008)) and has so far not been achieved.

In this study, we assume that a data product with extracted and processed satellite observations of the general circulation induced magnetic field exists. The numerical models described in sections 4.2.1.1 and 4.2.1.2 are used to generate daily global fields that contain synthetic, i.e., artificial, and idealized satellite observations of ocean-induced magnetic signals (see Fig. 4.2). The observations are calculated at a satellite altitude of 450 kilometers above sea level. To overcome the lack of the temporal deviation in the EM-induction model (see section 4.2.1.2) and to smoothen the transition between two consecutive observations, each daily observation is a weekly average of its preceding seven days (see also the orange bins in Fig. 4.1). Accordingly, the first observation at day 7 is generated from weekly averaged values over the days 1–7, the second observation at day 8 is generated from weekly averaged values over the days 2–8, and so on. From a range of tested setups of the observation operator, the usage of weekly averaged fields provided the best performance of the data assimilation (not shown). The uncertainty of the synthetic observations is modelled by adding uncorrelated Gaussian white noise with a standard deviation of 0.1 nT to each of the weekly averaged global fields. This matches with the nominal Swarm precision of 0.1 nT (Friis-Christensen et al. (2006), Olsen et al. (2007)). The respective variance values of the Gaussian white noise are utilized as diagonal elements of the observation error covariance matrix R. As already stated in section 4.2.2.1, spatial error covariances, i.e., non-diagonal elements, in R are not considered in this study. As there is still only very limited knowledge about actual satellite observations of the ocean-induced magnetic field and its observational uncertainty, estimating the respective values in R would be speculative and does not provide additional

conclusions in this twin experiment.

Due to several simplifications, the synthetic observations generated with this approach will naturally differ from actual satellite observations. The thin-sheet electromagnetic induction model assumes an insulating atmosphere and mantle (see section 4.2.1.2). Additionally, a high spatial and temporal resolution is assumed by generating daily and global observation fields with uniform errors. In our data assimilation twin experiment (section 4.2.2.2), the described synthetic observations are derived from MAGTRUTH and assimilated into MAGASSIM. Since MAGTRUTH is governed by the same ocean model and electromagnetic induction model and its simplifications, the realization of the real world is also restricted by these simplifications. Consequently, the twin experiment together with the synthetic observations build a consistent data assimilation test environment. The influence of more complex properties of observations (e.g., non-uniform temporal resolution, spatial gaps, non-uniform uncertainty, etc.) can also be investigated in a twin experiment approach but are not part of this first assimilation study. Instead, we investigate the principle possibility of recovering a known ocean state by assimilating observations of the ocean-induced magnetic field into an ocean general circulation model.
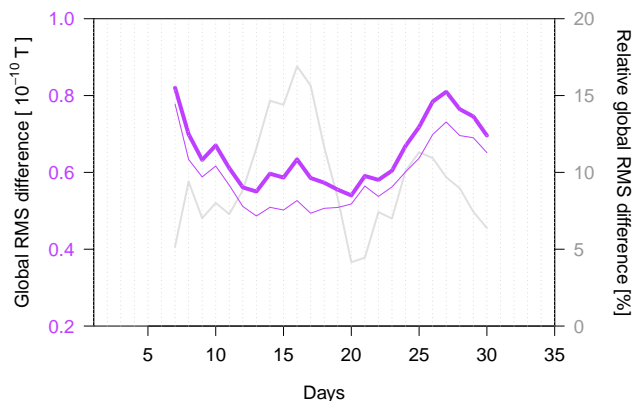
Figure 4.4: Global RMS differences of the MAGTRUTH ocean-induced magnetic field to MAGREF (thick purple line) and MAGASSIM (thin purple line). The relative difference between the two purple lines is depicted in grey.

4.3   Results and Discussion

4.3.1   Assimilation impact on the ocean-induced magnetic field

A first measure of the assimilation performance is the global impact of the Kalman filter on the assimilated variable, i.e., the ocean-induced magnetic field. Since the synthetic

satellite observations are generated from weekly-averaged fields (see section 4.2.2.3 and Fig. 4.1), we consistently measure the impact on the ocean model by calculating temporal RMS differences over the same weekly-average bins for each assimilation step. The global RMS differences of the ocean-induced magnetic field of MAGREF-MAGTRUTH and MAGASSIM-MAGTRUTH over the one-month simulation period are depicted in Figure 4.4. A perfect replication of MAGTRUTH would lead to a global RMS difference of zero. The values of the global RMS differences reside in the range of 0.05 and 0.08 nT. Both purple lines show a strong non-static and non-linear behaviour. This is due to the non-linear ocean model and its response to the highly variable atmospheric forcing. Since also the respective errors of the models and input data evolve in time (see Irrgang et al. (2016b)), the experiment setup builds a challenging test environment for the Kalman filter.

Throughout the whole simulation period, the global RMS differences between the corrected ocean-induced magnetic field and the known true values (thin purple line in Fig. 4.4) stay below the RMS differences between the reference and the truth (thick purple line in Fig. 4.4). In other words, the true motional induction is consistently better recovered (in the global sense) by the corrected model than by the reference without data assimilation. The improvement of the global RMS remains larger than 5 % in almost all assimilation steps and reaches values up to 17 % (see grey line in Fig. 4.4). The temporal mean improvement of the global RMS over the whole simulation period amounts to 8 %. Due to the twin experiment setup, the differences MAGREF-MAGTRUTH and MAGASSIM-MAGTRUTH must be attributed to the impact of the Kalman filter. Consequently, it can be concluded that the assimilation of the synthetic observations has a positive effect on the models (in the global sense) and leads to an overall improvement of the modelled ocean-induced magnetic field.

To investigate the assimilation impact on the ocean-induced magnetic field in more detail, global misfit maps containing the temporal RMS differences over the whole simulation period are shown in Fig. 4.5. The top left panel shows the misfit map between the reference and the truth with values of up to 0.22 nT. Note that this panel depicts the RMS error of the modelled ocean-induced magnetic field with respect to the known truth. Again, in the case of a perfect model replication of the true ocean-induced magnetic field, the misfit map would only show zero values. The highest RMS values with large-scale patterns are found in the North Pacific Ocean, east of Australia, east of South Africa, and in the North Atlantic Ocean. Generally lower RMS values are present in the area of the Antarctic Circumpolar Current. As described in section 4.2.2.2, the misfit between MAGREF and MAGTRUTH is essentially determined by the different wind stress forcings in the respective simulation time periods. The spatial distribution of the misfit between
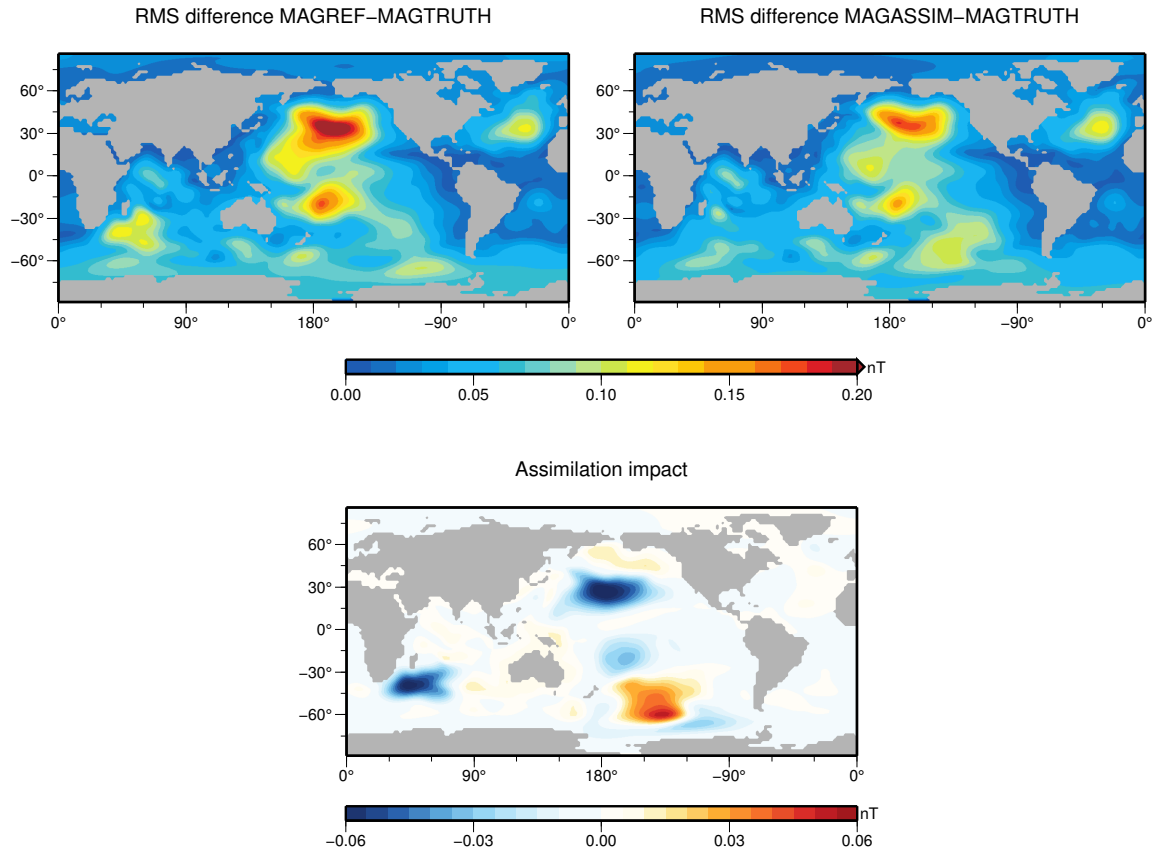
Figure 4.5: Top: RMS difference maps of the ocean-induced magnetic field of MAGREF-MAGTRUTH (left) and MAGASSIM-MAGTRUTH (right) over the whole simulation period. Bottom: Changes in the RMS difference due to the Kalman filtering (difference of the top maps). Blue areas indicate improvements, red areas indicate deteriorations.

MAGREF and MAGTRUTH shows similar patterns as the estimated uncertainty of the ocean-induced magnetic field due to the wind stress forcing (see Irrgang et al. (2016b)). Since the wind stress forcing and its uncertainty are variable on various temporal scales (see also Chaudhuri et al. (2013)), the MAGREF-MAGTRUTH misfit will also show different values and patterns for different simulation time periods.

The top right panel of Fig. 4.5 shows the RMS differences between MAGASSIM and MAGTRUTH. The maximum misfit is lower compared to MAGREF-MAGTRUTH with values up to 0.18 nT. The large-scale patterns in the North Atlantic Ocean and east of Australia are still present, but with generally lower values. The pattern east of South Africa almost vanished. The misfit in the North Atlantic Ocean is only changed marginally and in the South Pacific Ocean a new pattern with values around 0.12 nT is visible.

The so-called assimilation impact (bottom panel of Fig. 4.5) is the difference (MAGASSIM–MAGTRUTH)–(MAGREF–MAGTRUTH). It quantifies the changes due to the Kalman filter and shows values in the range of −0.07 and 0.05 nT. Here, negative values indicate improvements due to the Kalman filter and positive values indicate
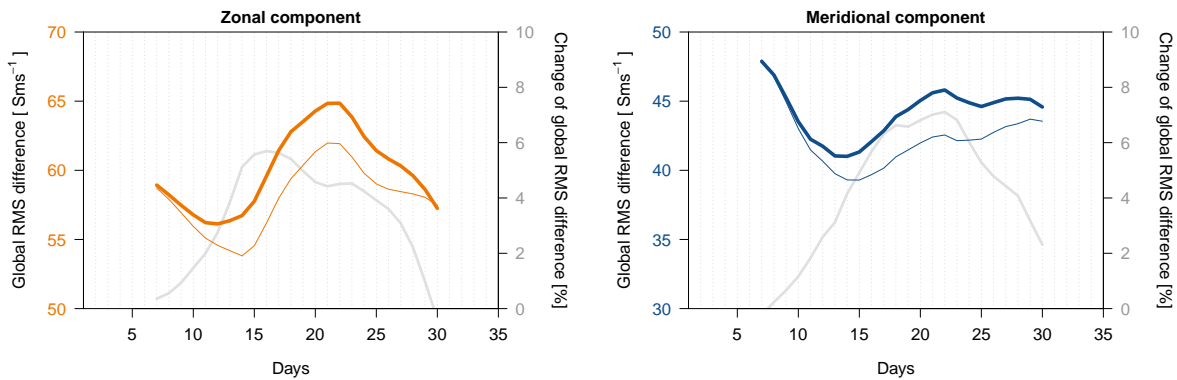
Figure 4.6: Global RMS differences MAGREF-MAGTRUTH (thick orange and thick blue lines) and MAGASSIM-MAGTRUTH (thin orange and thin blue lines) of the conductivity-weighted and depth-integrated ocean velocities. The relative difference for each pair of lines is depicted in grey.

deteriorations. From the assimilation impact it can be seen that the misfit of the ocean-induced magnetic field is reduced in almost all regions. The Kalman filtering leads to improvements especially in the regions with the largest misfits (see upper left panel of Fig. 4.5), i.e., in the North Pacific Ocean, east of Australia, and east of South Africa. The largest improvements correspond to a misfit reduction of up to 42 % in the North Pacific Ocean and up to 54 % in the region east of South Africa. In the South Pacific Ocean, the misfit between MAGASSIM and MAGTRUTH is larger than between MAGREF and MAGTRUTH, i.e., the Kalman filter introduced false corrections into the ocean-induced magnetic field in this region. Since the ocean-induced magnetic field is an integral quantity that is generated from several combined oceanic variables, there are many possible sources for the above described (positive and negative) impact of the Kalman filter. These sources are discussed in the following section.

4.3.2   Assimilation impact on the ocean model state

The novel opportunity of assimilating ocean-induced magnetic field observations is to provide constraints to depth-integrated conductivity and velocities to the ocean model. In a first order approximation, the ocean-induced magnetic field is proportional to the conductivity-weighted and depth-integrated ocean velocities (Sanford (1971)), which are calculated by the integral in Eq. 4.1. Therefore, we investigate the performance of the Kalman filter on these weighted depth-integrated velocities.

The global RMS differences of the conductivity-weighted and depth-integrated (hereafter called σ-depth-integrated) ocean velocities of MAGREF-MAGTRUTH and

MAGASSIM-MAGTRUTH are depicted in Fig. 4.6. The RMS differences reside in the range of 54 and 65 Sms^{-1} for the zonal (west-east) velocity and between 40 to 48 Sms^{-1} for the meridional (south-north) velocity. Similar to the ocean-induced magnetic field, both the zonal and meridional σ-depth-integrated velocities are corrected by the Kalman filter towards the truth (in the global sense) and show smaller RMS differences compared to the reference. The relative improvement amounts to up to 5 % for the zonal component and up to 7 % for the meridional component (see grey lines in Fig. 4.6). The temporal mean improvements of the global RMS of the zonal and meridional components amount to 3 % and 4 %, respectively. Note that the σ-depth-integrated velocities are not corrected uniformly, i.e., the evolution of improvements varies between the two components. This results from the uncertainty estimation of the two components, i.e., the respective error covariances in P_t, that are used to weight the observation residual in the assimilation step (see Eq. 4.9). This also underlines the importance of an accurate estimation of the error covariances between all state vector components in addition to the quality of the observations. Since the sediment conductance and the geomagnetic field are not corrected by the Kalman filter, the improvements in the ocean-induced magnetic field (see Figs. 4.4 and 4.5) originate from the combined improvements in the σ-depth-integrated velocities (see Eq. 4.1).

The MAGREF-MAGTRUTH misfit maps of the σ-depth-integrated velocities and the corresponding assimilation impacts are shown in Fig. 4.7. Again, the assimilation impact quantifies the RMS impact of the Kalman filter on the zonal and meridional velocity components over the whole simulation period. The large-scale pattern of the MAGREF-MAGTRUTH misfit of the σ-depth-integrated velocities are in agreement with the MAGREF-MAGTRUTH misfit of the ocean-induced magnetic field (compare Figs. 4.5 and 4.7). Naturally, the misfit of the σ-depth-integrated velocities shows more small-scale features that are not visible in the magnetic field misfit due to the upwardly continuation of the signal to satellite altitude. Additionally, it is visible that RMS differences of the zonal velocity close to the geomagnetic equator are weakened significantly in the RMS differences of the ocean-induced magnetic field, e.g, north east of Madagascar or in the equatorial region of the East Pacific Ocean. Since the motional induction signal is close to zero in proximity of the geomagnetic equator, this intrinsic 'observation blindness' provides an additional challenge to the Kalman filter.

A comparison of Figs. 4.3 and 4.7 allows to draw relations between the major ocean currents, the RMS differences between MAGREF and MAGTRUTH, and the assimilation impact in the regions of the respective currents, respectively. In comparison with the assimilation impact of the ocean-induced magnetic field (Fig. 4.5), the σ-depth-integrated velocities show similar large-scale improvements with values over -40 Sms^{-1} ($\approx 30\%$) in

RMS difference MAGREF–MAGTRUTH

Zonal component   Meridional component

Assimilation impact

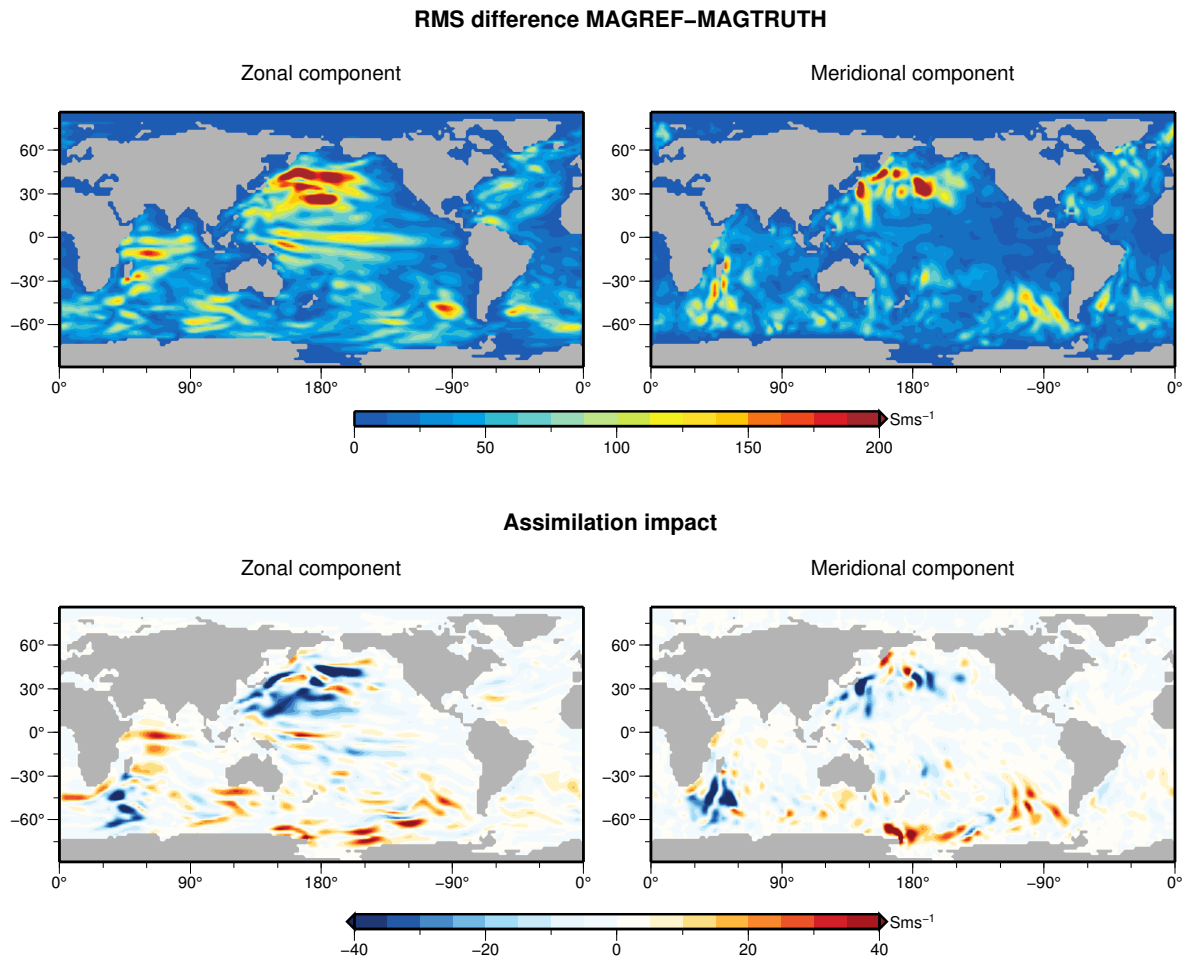Zonal component   Meridional component

Figure 4.7: Top: RMS difference maps of the conductivity-weighted and depth-integrated ocean velocities of MAGREF-MAGTRUTH. Bottom: Changes in the RMS difference due to the Kalman filtering. Blue areas indicate improvements, red areas indicate deteriorations.

the North Pacific Ocean. Especially in the region of the Kuroshio current, large improvements over $-60\,\mathrm{Sms^{-1}}$ ($\approx 50\%$) are found. In the Antarctic Circumpolar Current, the largest improvements are found east of South Africa, with values over $-50\,\mathrm{Sms^{-1}}$ ($\approx 30\%$) (bottom row of Fig. 4.7). Peak values of the improvement reach over $-100\,\mathrm{Sms^{-1}}$ in the North Pacific Ocean. In the equatorial region of the zonal currents, the transport is corrected by up to $-20\,\mathrm{Sms^{-1}}$ ($\approx 25\%$), and in the region of the Gulf stream by up to $-10\,\mathrm{Sms^{-1}}$ ($\approx 15\%$). Since the strongest ocean-induced magnetic field signals and respective variations occur in the region of the Antarctic Circumpolar Current (compare Fig. 4.2), it was common to assume that improvements due to data assimilation are also mainly confined to regions in the southern hemisphere. Consequently, the shown large-scale improvements in the northern hemisphere, especially in the North Pacific Ocean, are both surprising and encouraging for the application of this technique.

In general, the deterioration pattern between the ocean-induced magnetic field and
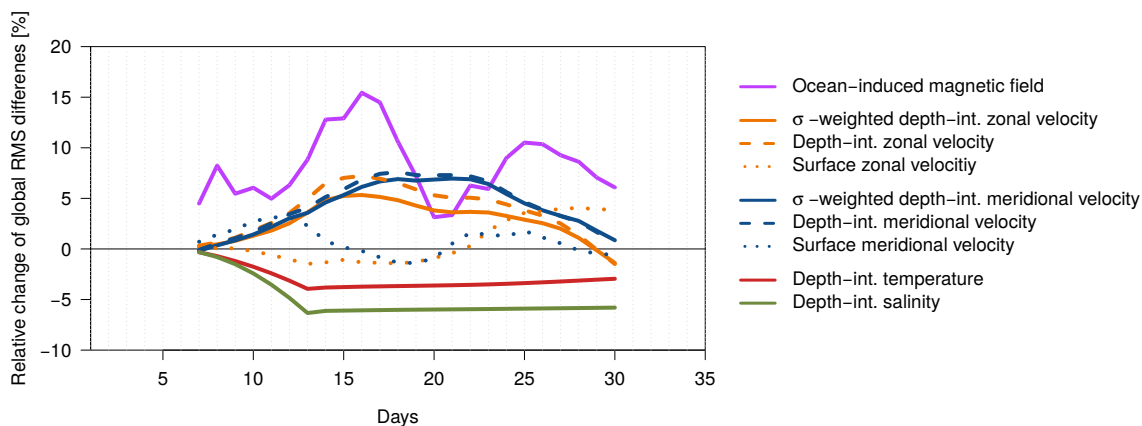
Figure 4.8: Relative changes of the global RMS differences. Positive values indicate improvements of the respective quantities, negative values indicate deteriorations.

the σ-depth-integrated velocities also coincide (compare Figs. 4.5 and 4.7). The largest deteriorations with values between 30 and 40 Sms^{-1} occur for both velocity components in the South Pacific Ocean between the Ross Sea and the southern tip of South America. Further false corrections by the Kalman filter are visible in the zonal velocity in the Northwest Indian Ocean close to the geomagnetic equator.

The most likely source of these false correction is a deficient prescription of the error covariance information in P_t for that particular region, which is solely based on the temporal covariances of MAGREF (see Sec. 4.2.2.2). An accurate calculation of the error covariances is a challenge and the estimation of these is not unique (Irrgang et al. (2016b)). However, the current configuration of the Kalman filter functions remarkably well in improving the ocean-induced magnetic field and the σ-depth-integrated velocities in most regions, given the blurry and noisy magnetic field observations. Further constraints on the error covariances, especially for the wind stress forcing, could resolve the major deteriorations found in the South Pacific Ocean and further reduce the differences between the ocean model and the known true ocean state.

Over simulation periods longer than one month, the impact of the Kalman filter on the ocean model state becomes negligible. The model uncertainty decreases during each assimilation step, which eventually leads to an underestimation of the model variance (not shown). Thereby, the confidence in the ocean model state and in the adjusted wind stress forcing rises continuously compared to the confidence in the observations. This reduces the Kalman filter increments in each assimilation step. Consequently, the MAGASSIM and MAGTRUTH model trajectories gradually diverge due to the non-linear ocean model and due to the non-static atmospheric forcing. This is a well known behaviour (e.g., Furrer and Bengtsson (2007)) and might be overcome in subsequent studies by
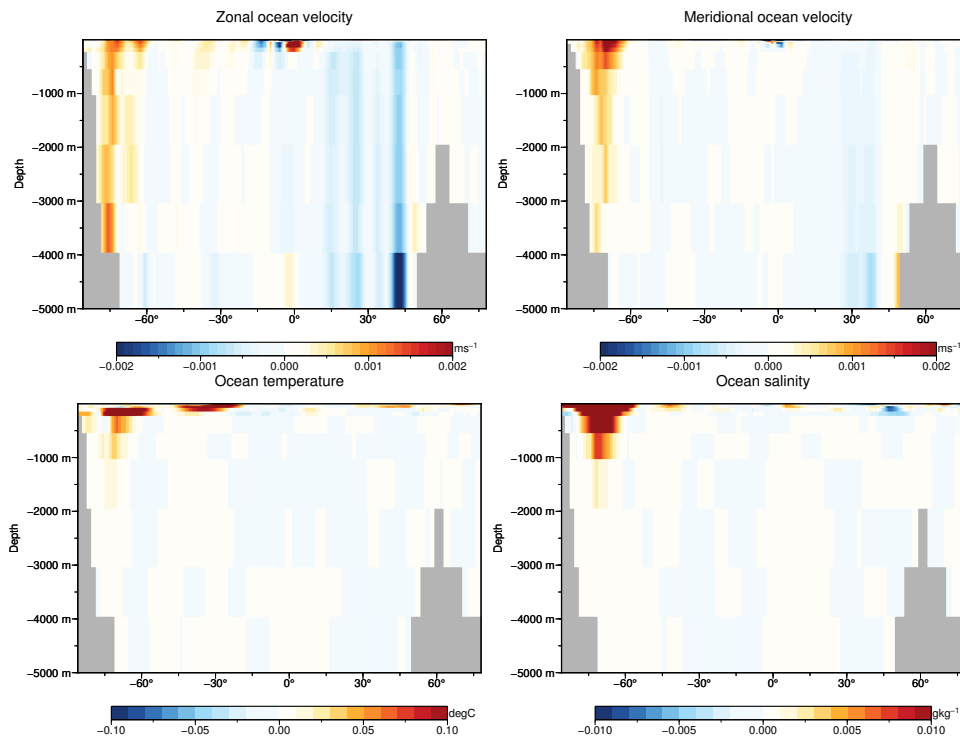
Figure 4.9: Zonally (west-east) averaged depth-profiles of the assimilation gain over the whole simulation period. Blue areas indicate improvements, red areas indicate deteriorations.

applying additional covariance inflation techniques (e.g., Anderson (2007)) or sequential assimilation experiments over consecutive simulation periods that utilize specific error covariance matrices.

The biggest challenge in assimilating ocean-induced magnetic field satellite observations is the improvement of the separate ocean variables that determine the motional induction, i.e., ocean velocities, temperature and salinity. The impact of the Kalman filter on each of these four variables is depicted in the Figs. 4.8 and 4.9. Fig. 4.8 shows the relative change of the global RMS differences for each variable over the whole simulation period. In addition to the curves of the ocean-induced magnetic field and the σ-depth-integrated velocities presented before (see grey lines in Figs. 4.4 and 4.6), the respective curves for depth-integrated velocities, surface velocities, temperature and salinity are plotted. The changes in the RMS differences of ocean temperature and salinity reveal that the Kalman filter fails to improve these quantities (green and red lines in Fig. 4.8) during all assimilation steps. Although the deterioration gradually decrease over time after day 13, the values mostly remain between -2 and -3 % for the depth-integrated temperature and between -4 and -5 % for the depth-integrated salinity. One explanation of this false shift is a possibly deficient estimation of the temperature and salinity error covariances for the simulated time period. The combined false shift in the two components

is transferred to the sea-water conductivity and, subsequently, to the σ-depth-integrated velocities. Thereby, the depth-integrated zonal and meridional velocities show a larger improvement than the respective conductivity-weighted quantities (see dashed blue and orange lines in Fig. 4.8). The difference between the conductivity-weighted and non-weighted depth-integrated velocities amounts to up to 2 percentage points (compare solid and dashed blue and orange lines in Fig. 4.8). It was possible to weaken the false shift in the ocean temperature and salinity, by reducing the Kalman filter increments of the two variables in each assimilation step (not shown). However, it is important to demonstrate the challenge of improving the whole ocean state consistently. A second challenge becomes apparent, when the relative changes in RMS differences of depth-integrated ocean velocities and of surface velocities are compared (compare dashed and dotted blue and orange lines in Fig. 4.8). In contrast to the water transport over the whole water column, surface currents are not improved consistently over the simulation period. The respective relative changes in the RMS differences of the surface velocities are generally smaller than changes in the depth-integrated quantities and fluctuate between -2 and 5 %. Not surprisingly, this result shows that a consistent global correction of oceanic transports at individual layers of the ocean model is difficult due to the integral magnetic field observations. For this, additional constraints are necessary, which relate the observed ocean-induced magnetic field to its electromagnetic source at individual depths of the ocean.

In addition to showing the assimilation improvements in an depth-integrated sense, Fig. 4.9 depicts the Kalman filter impact as zonally and temporally averaged cross sections of the global ocean for each oceanic quantity. This allows to associate the Kalman filter impact (in depth-integrated sense as seen in Fig. 4.7) with specific depths. The zonal and meridional ocean velocities show improvements over large regions of the cross sections that reach from the sea surface down to the ocean bottom (upper left and right panels of Fig. 4.9). Most prominent regions are found in the northern hemisphere between 0° and 60°. Consequently, the previously described improvements of the σ-depth-integrated velocities in the North Pacific Ocean (bottom panels of Fig. 4.7) result from a state shift towards the true state over the whole water column. In contrast, the improvements found in the equatorial region of the σ-depth-integrated zonal velocities mainly originate from a state correction in the upper 250 m (compare lower left panel of Fig. 4.7 and upper left panel of Fig. 4.9). Likewise, the deterioration of the σ-depth-integrated zonal velocity in the north west Indian ocean also originates from a false correction in the upper 250 m. The most prominent false corrections in the ocean-induced magnetic field and in the σ-depth-integrated velocities in the South Pacific Ocean (Figs. 4.5 and 4.7) dominantly originate from deteriorations in the zonal and meridional velocities over the whole water columns. These are additionally intensified by false corrections of the ocean salinity and
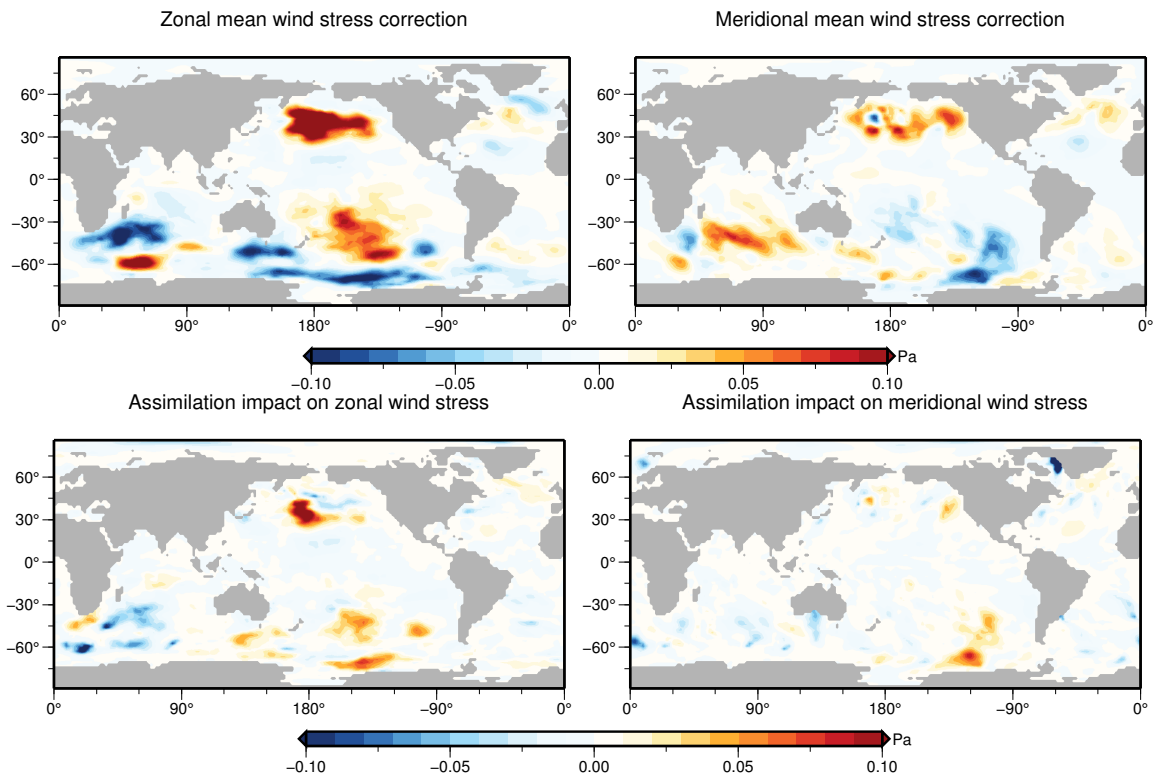
Figure 4.10: Top: Temporal mean wind stress forcing corrections due to the Kalman filtering. The maps show ensemble mean values. Bottom: Changes in the RMS differences of the wind stress forcing due to Kalman filtering. Blue areas indicate improvements, red areas indicate deteriorations.

temperature in the upper 1000 m south of $-60°$ (bottom panels of Fig. 4.9).

A consistent correction of the wind stress forcing together with the ocean model state is found to be essential for the described results of the data assimilation. In a twin experiment without wind stress correction (otherwise identical to the twin experiment of this study), the Kalman filter failed to improve both the ocean model state and the ocean-induced magnetic field (not shown). Previously, Saynisch et al. (2014) also recognized the need to correct the wind stress forcing in order to improve trajectories of an ocean general circulation model. This repeatedly underlines the fragility of data assimilation in ocean models. The temporal mean correction of the wind stress forcing estimated by the Kalman filter and the respective assimilation impact are shown in Fig. 4.10. Most values reside in the range of $\pm$ 0.1 Pa. The large-scale wind stress corrections are well in agreement with the uncertainty estimation of the ocean-induced magnetic field (see Irrgang et al. (2016b)) and, subsequently, with the assimilation impact of the ocean-induced magnetic field and of the σ-depth-integrated velocities (compare top row of Fig. 4.10 with Figs. 4.5 and 4.7). This points out the close connection of the error covariances between the ocean state and the wind stress forcing. In the regions of highest wind stress adjustment, the

vertical adjustment of the ocean velocities mostly extends over the whole water column (see Fig. 4.9). In particular, the top row of Fig. 4.10 shows a considerable adjustment of the wind stress forcing in the South Pacific Ocean, where the largest deteriorations in the ocean-induced magnetic field and in the σ-depth-integrated velocities are detected. Consequently, the false corrections by the Kalman filter are assumed to dominantly originate from a deficient estimation of the error covariances between the wind stress forcing and the ocean model state, and a false adjustment of the wind stresses in this region. This is further emphasized by the assimilation impact on the wind stress forcing (see bottom row of Fig. 4.10). As it was shown for the σ-depth-integrated velocities in Fig. 4.7, the blue areas represent improvements due to the Kalman filtering, whereas red areas indicate deteriorations. The major deteriorations, which are visible in the North and South Pacific Ocean, largely coincide with the major deteriorations in the σ-depth-integrated velocities (compare bottom rows of Figs. 4.7 and 4.10). These overestimated adjustments are attributed to the functionality of the Kalman filter, as corrections of the wind stress forcing are based on static error covariance matrices instead of dynamic ensemble-based correction estimates. However, in most regions, large-scale improvement of RMS differences of both zonal and meridional wind stresses are visible. As stated before, these adjustments are found to be essential for a successful assimilation.

The assimilation of synthetic ocean-induced magnetic field satellite observations into an ocean general circulation model shows very promising results. Despite the low amount of detail in the blurry observations, the Kalman filter succeeded to improve the ocean model results in all erroneous regions. Additionally, the observations positively constrained ocean velocities from the sea-surface down to the deep ocean. This study highlights that actual satellite observations of the general circulation induced magnetic field could be utilized to constrain large-scale oceanic transports. Subsequent studies may demonstrate the sensitivity of the assimilation towards the data quality (e.g. non-uniform noise, spatial and temporal gaps, residuals from other electromagnetic sources etc.). In turn, it might be possible to provide minimum requirements of the quality of actual magnetic field observations for a successful data assimilation. Our results emphasize the need for a careful treatment of model uncertainties and error covariances. Aside from the quality of the observational data, the knowledge about model and forcing uncertainties is crucial for a successful data assimilation.

4.4   Summary and Conclusion

The general ocean circulation generates characteristic magnetic signals that in principle can be detected by low earth orbit satellites like the Swarm mission. Since these magnetic

signals are mainly proportional to the conductivity-weighted and depth-integrated ocean velocities, the satellite observations may serve as indirect observations of global oceanic water and heat transports. In this study, we investigate the potential to correct an ocean general circulation model by assimilating artificial satellite observations of the ocean-induced magnetic field for the first time. In a model-based twin experiment over the time period of one month, the impact of the data assimilation on the individual components of the oceanic electromagnetic induction source is estimated, i.e., ocean velocities, ocean temperature, and ocean salinity.

Due to the difficult separability of the general circulation induced magnetic field from other electromagnetic sources, these signals have so far not yet been detected in satellite observations. Instead, we assume that a data product exists that contains idealized daily global observation fields of the ocean-induced magnetic field at satellite altitude. The synthetic satellite observations are calculated with a combination of an ocean general circulation model and an electromagnetic induction model. Observational errors are modelled by adding uncorrelated Gaussian white noise to the calculated magnetic signals. These synthetic observations are sequentially assimilated into the ocean model. The data assimilation is performed by a localized version of an ensemble-based error subspace Kalman filter. This Kalman filter is integrated into the ocean model and corrects zonal and meridional ocean velocities, ocean temperature, and ocean salinity, and wind stresses from the atmospheric forcing of the ocean model.

Compared to a reference simulation without data assimilation, the simulation corrected by the Kalman filter performs better in recovering the synthetic observations throughout the whole simulation period. The global RMS error of the ocean-induced magnetic field is reduced by up to 17 %. Locally, the RMS reduction amounts up to 42 % in the North Pacific Ocean and up to 54 % in the region east of South Africa. All spatial regions with large RMS errors in the reference simulation, e.g., in the North Pacific Ocean, east of Australia, and east of South Africa, are improved in the simulation with data assimilation. In particular, the results demonstrate the feasibility to correct an ocean model in areas with comparable weak induced magnetic field observations, e.g., in the North Pacific Ocean and in equatorial regions. False corrections are introduced in the South Pacific Ocean that originate from false adjustments in the conductivity-weighted and depth-integrated ocean velocities. The main source of false corrections is presumably due to the combined effect of large wind stress forcing adjustments and a deficient estimation of ocean model and wind stress error covariances. In an identical twin experiment without correction of the wind stress from the atmospheric forcing of the ocean model, it was not possible to recover the synthetic observations.

The conductivity-weighted and depth-integrated velocities are improved throughout

the simulation period (in the global RMS sense) with values up to 5 % for the zonal component and up to 7 % for the meridional component. Locally, the improvements of water transports in individual ocean currents reach higher values, e.g., over 30 % in the Antarctic Circumpolar Current, over 50 % in the Kuroshio current, over 15 % in the Gulf Stream, and over 25 % in the equatorial region of the Pacific Ocean. The improved regions coincide with the improved regions of the ocean-induced magnetic field. Global RMS differences of the individual components reveal that the Kalman filter fails to improve ocean temperature and salinity. However, vertical cross-sections of the individual ocean variables reveal that respective improvements in the ocean velocities mostly extend from the sea surface down to the deep ocean, whereas deteriorations in the ocean temperature and salinity mostly reside in the upper 1000 m of the southern ocean. Since all major deteriorations in the ocean model state are introduced in regions with major corrections of the wind stresses, a more dynamical estimation of the error covariances between the ocean state and the atmospheric forcing might diminish these false corrections.

The results of this study show that satellite observations of the ocean-induced magnetic field could provide useful constraints on depth-integrated ocean variables, e.g., oceanic water and heat transports. Although even the idealized synthetic satellite observations only provide a small amount of detail, the Kalman filter succeeded to better recover both the ocean-induced magnetic field and the underlying ocean state in most regions. Consequently, these results support the ongoing effort to separate ocean circulation in-duced magnetic signals in satellite observations. However, actual satellite observations will naturally differ from the idealized data generated for this study. Among others, these differences result from the simplified physics in the electromagnetic induction model, the considered time period, temporal and spatial gaps in the observations, and remaining residuals from other electromagnetic induction sources. The same holds for the spatio-temporal distribution of observational uncertainty, which is assumed uniform in this study. Future studies might provide minimum constraints on the data quality necessary to gain useful constraints on the underlying general ocean circulation. From the ocean modelling perspective, the results of this study emphasize the crucial need for realistic and dynamic error covariance matrices. In addition to the quality of the data, knowledge about model and forcing uncertainties is essential for a successful data assimilation.

5

Summary and Outlook

Short version. Satellite observations of electromagnetic induction in the ocean provide the opportunity to infer global estimates about oceanic transports of water, heat, and salinity. The Ocean Model for Circulation and Tides and an electromagnetic induction model are combined to simulate magnetic signals that are generated by the general ocean circulation. This model setup is used to examine the ocean-induced magnetic field in terms of magnitude, spatial and temporal variability, sensitivity towards oceanic variables, and model uncertainties. For the first time, these findings are utilized to design and to perform data assimilation experiments, aiming to constrain the ocean general circulation model with artificial satellite observations of the ocean-induced magnetic field. It was possible to improve the recovery of simulated depth-integrated ocean velocities with an ensemble-based Kalman filter. In contrast, it is demonstrated that it remains a challenge for future motional induction data assimilation studies to simultaneously improve ocean velocities, heat and salinity distributions in a consistent way.

Long version. The main focus of this thesis lay on the characterization of electromagnetic induction in the world ocean and possible beneficial applications of this geomagnetic process in the context of ocean modelling. Ultimately, it was investigated whether satellite observations of oceanic electromagnetic induction can be utilized to constrain forward simulations of an ocean general circulation model. Three consecutive numerical model-based studies were presented that contribute to the topics of *physical characterization*, *uncertainty estimation*, and *data assimilation*, respectively, and answer the research questions posed at the beginning of this thesis (see section 1.4).

Two numerical models were combined to simulate electromagnetic induction in the ocean. *(1)* The general ocean circulation was simulated with the Ocean Model for Circulation and Tides (OMCT). OMCT is a baroclinic ocean model based on nonlinear balance equations for momentum, the continuity equation, and conservation equations for heat and salt. The atmospheric forcing of OMCT encompasses heat-flux, wind stress, surface pressure, precipitation, and evaporation. Ocean tides were not considered in the current configuration of OMCT. *(2)* A magnetostatic induction model was used to derive the ocean-induced magnetic field from instantaneous OMCT states. The radial component of the poloidal induced magnetic field was calculated by solving a 2-D induction equation based on Maxwell's equations. In this approach, only horizontal ocean flow was considered for the induction process, reducing the ocean basin to a thin shell. Together with a conductive layer of oceanic sediments, this thin shell was nested between an insulating atmosphere and an insulating mantle.

Physical characterization. The magnetic field induced by the general ocean circulation is five orders of magnitudes smaller compared to the magnetic core field of the Earth and reaches values up to a few nano Tesla. Additionally, its spatio-temporal variations are highly irregular due to the wind- and density-driven electric current source in the ocean. As the ocean-induced magnetic signal range furthermore overlaps with other magnetic field constituents of similar magnitude, these signals have not yet been detected in satellite observations. A realistic model-based estimation of motional induction can help to accelerate the data-based detection and separation of motional induction signals. In particular, temporal variations of the ocean-induced magnetic field distinguish the signal from other more static magnetic field constituents of the same order of magnitude, e.g., the crustal magnetic field. Therefore, the two numerical models were utilized to estimate the ocean-induced magnetic signals and to assess their sensitivity towards oceanic quantities. In several previous studies, seawater was treated in a simplified way by assuming it to be uniformly distributed or time-invariant. To validate these simplifications, the influence of spatial and temporal seawater conductivity variations on the variability of motional induction was investigated. It was shown that a globally uniform seawater conductivity is insufficient to capture the temporal variability of motional induction accurately. Especially the large vertical gradients in seawater conductivity in the upper ocean above the main thermocline impact the electromagnetic induction process and its temporal variations. In contrast, it was shown that seasonal and annual variability of seawater conductivity only have a marginal influence on the induction process.

Uncertainty estimation. Numerical forward simulations of the general ocean circulation are affected by various sources of uncertainty, mostly due to errors in the atmospheric forcing of ocean models. These errors are highly non-uniform on various spatial and tem-

poral scales. Several studies have estimated the non-negligible response of ocean models to such uncertainties, implying that the ocean circulation induced magnetic field is subject to these introduced uncertainties, too. To examine this hypothesis, ensemble simulations of OMCT and the electromagnetic induction model were performed. There are two major benefits from estimating the aggregated uncertainty in forward simulations of motional induction. First, since simulated oceanic magnetic signals are supposed to be comparable to actual observations of these magnetic signals, a reasonable uncertainty range of the simulated signals is desirable. Assessing the sensitivity of model results towards uncertainties in input data also allows the identification of so-called robust regions, i.e., regions that retain a small uncertainty regardless of the variations in input data errors. Identified robust regions in the simulated ocean-induced magnetic field can then be utilized as prioritized candidate regions for reliable comparisons of model results and real-world observations. Second, the estimation of uncertainties in modelling motional induction by an ensemble-based approach, e.g., with the usage of error covariance matrices, is necessary for data assimilation experiments. Therefore, uncertainty estimates for ocean velocities, oceanic heat and salinity distributions, atmospheric wind stress forcing, sediment conductance, geomagnetic core field, and respective spatial and temporal covariances were derived in the form of monthly varying error covariance matrices. An ensemble of different model realizations was generated on the basis of these error covariance matrices for conservative and extreme error scenarios. The ensemble spread of the simulated ocean-induced magnetic field was a measure of uncertainty, allowing to quantify its magnitude, as well as spatial and temporal variations. It was shown that the ocean-induced magnetic field reacts very sensitively with respect to the introduced uncertainties. Largest uncertainties occurred in the southern hemisphere in the area of the Antarctic Circumpolar Current. Distinct seasonal variations were detected in the motional induction uncertainty, which were governed by uncertainties in the wind stress forcing of the ocean model. Uncertainties in the geomagnetic core field and in the sediment conductance were found to be negligible. Despite the large uncertainty range in some areas, large-scale regions were identified in the ocean-induced magnetic field that retained a small uncertainty in all error scenarios.

Data assimilation. An ensemble-based Kalman filter was used to correct ocean velocities, temperature, and salinity distributions of OMCT by assimilating artificial satellite observations of the ocean-induced magnetic field. At this time, no Swarm satellite observations of the general circulation induced magnetic field were available and the possible beneficial impact of assimilating these observations into an ocean model was unknown. Therefore, this study was designed as a proof of concept to investigate the principle feasibility of assimilating satellite observations of motional induction into a global ocean

model. An Observing System Simulation Experiment (OSSE) was constructed to measure the impact of the Kalman filter on the ocean model state, compared to an assimilation-free simulation. Synthetic satellite observations were generated from the combined ocean model and electromagnetic induction model, which incorporated the realistic estimation of electric seawater conductivity. The Kalman filter ensemble was generated based on derived monthly error covariance matrices that prescribe uncertainties for the numerical models and for wind stress forcing data. The proportionality between ocean-induced magnetic signals and depth-integrated ocean flow is the primary source for corrections in the ocean model state due to the Kalman filter. Globally averaged trajectories of the corrected depth-integrated ocean velocities and of the corresponding ocean-induced magnetic field were reproducing the synthetic observations consistently better than the assimilation-free simulation. The spatial analysis has shown that all regions with large errors in the global maps of depth-integrated velocities and of the ocean-induced magnetic field were identified and reduced by the Kalman filter. These results could not have been reproduced without Kalman filter corrections of the atmospheric wind stress forcing of the ocean model. This, again, highlights the high degree of uncertainty in the wind stress forcing and the necessity to correct the wind stress forcing in data assimilation experiments. The analysis over the vertical water column revealed that improvements of ocean velocities reach from sea surface to ocean bottom. Especially the correction of velocities in the deep ocean was envisioned as one of the key benefits from utilizing ocean-induced magnetic field observations in data assimilation experiments. At the same time, the underdetermination of the ocean state by the integral magnetic field observations showed its effect by false Kalman filter corrections of oceanic temperature and salinity distributions in the upper 1000 metres in the Southern Ocean. Additionally, deteriorations can be generated, or amplified, by deficiently estimated error covariances between the ocean model and the wind stress forcing.

The results presented in this thesis demonstrate the encouraging benefits of inferring properties of the world ocean by detecting its emitted electromagnetic signals. Likewise, the complex challenges of this task are highlighted. To further mature motional induction data assimilation that eventually utilizes actual satellite observations, the following branches need to be further investigated:

The used magnetostatic thin-sheet induction model is based on several physical simplifications, i.e., no temporal deviations (magnetostatic assumption), insulating subsurface structure in the Earth's mantle, no vertical diffusion due to the thin-sheet approximation, and no coupling to the toroidal induced magnetic field. Consequently, the motional induction model might not be the optimal observation operator in data assimilation studies with actual satellite observations. Grayver et al. (2016) have recently shown, that assum-

ing an insulating mantle is insufficient to numerically reproduce the tidal (M2) induced magnetic field recovered from Swarm satellite data. Similar results might hold for the ocean circulation induced magnetic field, due to the galvanic coupling of the ocean with the seafloor. The magnetostatic assumption holds well for seasonal and annual time scales of the general ocean circulation (see chapters 2 and 3), but it was not possible to derive accurate daily observations with this approach (see section 4.2.2.3). A detailed comparison of the currently existent electromagnetic induction models (see, e.g., Tyler et al., 1997; Vivier et al., 2004; Velímský and Martinec, 2005; Kuvshinov and Semenov, 2012) and a classification for potential applications is currently undertaken in a cooperated benchmark study. The results of this benchmark might already indicate the most suitable motional induction observation operator for future data assimilation studies. Additionally, such a numerical model benchmark can help to quantify and to compare the contributions of the various simplifications that are implemented into the electromagnetic induction models (see also Sec. 1.2)

The estimation of uncertainties in the numerical modelling of geophysical processes is an important and still emerging research topic. One crucial and difficult task in this topic is the accurate estimation of error covariance matrices (see chapter 3). Realistic error covariances, which consider the major spatial and temporal scales of the examined geophysical process, are essential for successful data assimilation studies. In chapter 4, it was shown, that even the specific monthly error covariance matrices are still a major cause for false adjustments in the ocean model state. These are largely originating from deficient error covariance estimates of the ocean's response to sea surface wind stresses. Incorporating additional error information, e.g., by deriving error covariances from additional atmospheric forcing reanalysis products, will lead to more precise adjustments by Kalman filter schemes.

The findings of this thesis highlight that monitoring and utilizing electromagnetic induction in the ocean has the potential to complement existing observation techniques of the world ocean. Besides the new insights into the model-based perspective of motional induction that are presented in this thesis, the recovery of actual satellite observations of the ocean-induced magnetic field will shed new light onto this topic. Further potential sources of oceanic magnetic field observations, e.g., land-based magnetometers or ocean bottom magnetometers mounted on sea cables, might also find their way into novel techniques to observe the ocean and to find new constraints for ocean models. The ongoing effort to collect new high-quality oceanic magnetic field observations will allow another step in the future development of this fascinating way to view the world ocean and its interior.

List of Figures

Nomenclature

Abbreviations

4DVar	Four-dimensional variational assimilation method
ACC	Antarctic Circumpolar Current
AMOC	Atlantic Meridional Overturning Circulation
ARGO	Worldwide fleet of drifting ocean profiling floats
CFSR	Climate Forecast System Reanalysis
CHAMP	CHAllenging Minisatellite Payload
ECMWF	European Centre for Medium-Range Weather Forecasts
ERA-Interim	ECMWF reanalysis product (1979 – present)
GRACE	Gravity Recovery And Climate Experiment
IPCC	Intergovernmental Panel on Climate Change
LESTKF	Local Error Subspace Transform Kalman Filter
LSDM	Land Surface Discharge Model
M2	Principal lunar semi-diurnal ocean tide constituent
N2	Larger lunar elliptic semi-diurnal ocean tide constituent
NCEP	National Centers for Environmental Prediction
OGCM	Ocean General Circulation Model
OMCT	Ocean Model for Circulation and Tides
OSSE	Observing System Simulation Experiment
Ørsted	Danish geomagnetic field satellite mission
PDAF	Parallel Data Assimilation Framework
SAC-C	Scientific Application Satellite-C
SEIK	Singular Evolutive Interpolated Kalman filter
Swarm	ESA geomagnetic field satellite mission
TOPEX/Poseidon	Ocean Surface Topography from Space

List of Symbols

Symbol	Definition	Unit
$\vec{\nabla} f, \vec{\nabla} \cdot \vec{f}, \vec{\nabla} \times \vec{f}$	Nabla: Gradient of $\vec{f}$, Divergence of $\vec{f}$, Rotation of $\vec{f}$	
$\vec{B}$	Magnetic field	[T]
$\boldsymbol{b}, \vec{b}$	Ocean-induced magnetic field	[T]
b_r	Radial component of the ocean-induced magnetic field	[T]

C_t	Square root matrix of U_t, .i.e., $U_t = C_t^T C_t$	
$\vec{E}$	Electric field	$[\mathrm{V\ m^{-1}}]$
$\vec{e}_z$	Unit vector in z-direction	
ε_0	Permittivity of free space	$[\mathrm{F\ m^{-1}}]$
$\vec{F}$	Geomagnetic core field	$[\mathrm{T}]$
F_z	Radial component of the geomagnetic core field	$[\mathrm{T}]$
$H[\cdot]$	Observation operator	
h	Ocean basin depth	$[\mathrm{m}]$
$\vec{j}$	Electric current density	$[\mathrm{A\ m^{-2}}]$
j	Spherical harmonic degree	
K_t	Kalman gain matrix at time t	
m	Spherical harmonic order	
μ_0	Permeability of free space	$[\mathrm{H\ m^{-1}}]$
Ω_t	Random matrix at time t	
P	Magnetic potential field	$[\mathrm{V\ s\ m^{-1}}]$
P_t	State covariance matrix at time t	
$\tilde{P}_t$	Reduced-rank approximation of P_t at time t	
ϕ	Longitudinal coordinate	$[\mathrm{°E}]$
ψ_e	Electric stream function	$[\mathrm{A}]$
ψ_{jm}	Spherical harmonics coefficients of degree j and order m	
R_E, a	Mean Earth radius of 6371 km	
R_t	Observation covariance matrix at time t	
r	Observation height of the ocean-induced magnetic field	$[\mathrm{m}]$
ρ	Electric charge density	$[\mathrm{C\ m^{-3}}]$
S	Seawater salinity	$[\mathrm{g\ kg^{-1}}]$
Σ	Depth-integrated conductivity	$[\mathrm{S}]$
Σ_{sed}	Depth-integrated sediment conductivity	$[\mathrm{S}]$
σ	Seawater conductivity	$[\mathrm{S\ m^{-1}}]$
T	Seawater temperature	$[\mathrm{°C}]$
t	Time	$[\mathrm{s}]$
ϑ	Latitudinal coordinate	$[\mathrm{°N}]$
τ_x, τ_y	Zonal and meridional wind stress forcing	$[\mathrm{Pa}]$
U_t	Eigenvector matrix at time t	
$\vec{u}$	Ocean velocity vector	$[\mathrm{m\ s^{-1}}]$
u	Zonal ocean velocity	$[\mathrm{m\ s^{-1}}]$
$\mathbf{u}_H$	Horizontal ocean velocity vector	$[\mathrm{m\ s^{-1}}]$
V_t	Eigenvalue matrix at time t	
v	Meridional ocean velocity	$[\mathrm{m\ s^{-1}}]$
x_t	Ocean model state vector at time t	
x_t^a, x_t^f	State vector analysis and forecast at time t, respectively	
Y_{jm}	Spherical harmonics functions of degree j and order m	
y_t	Observation vector at time t	
z	Vertical coordinate	$[\mathrm{m}]$
ζ	Sea surface height	$[\mathrm{m}]$

Bibliography

Anderson, J. L.: An adaptive covariance inflation error correction algorithm for ensemble filters, Tellus A, 59, 210–224, doi:10.1111/j.1600-0870.2006.00216.x, 2007.

Apel, J. R.: Principles of ocean physics, vol. 38, Inte. Academic Press., San Diego, California, 1987.

Atkinson, K. and Han, W.: Spherical Harmonics and Approximations on the Unit Sphere: An Introduction, Springer, Heidelberg, 2012.

Bouttier, F. and Courtier, P.: Data assimilation concepts and methods, p. 59 pp., European Centre for Medium-Range Weather Forecasts, England, 1999.

Chaudhuri, A. H., Ponte, R. M., Forget, G., and Heimbach, P.: A Comparison of Atmospheric Reanalysis Surface Products over the Ocean and Implications for Uncertainties in Air–Sea Boundary Forcing, J. Climate, 26, 153–170, doi:10.1175/JCLI-D-12-00090.1, 2013.

Chaudhuri, A. H., Ponte, R. M., and Nguyen, A. T.: A Comparison of Atmospheric Reanalysis Products for the Arctic Ocean and Implications for Uncertainties in Air–Sea Fluxes, J. Climate, 27, 5411–5421, doi:10.1175/JCLI-D-13-00424.1, 2014.

Chave, A. D.: On the theory of electromagnetic induction in the Earth by ocean currents, J. Geophys. Res., 88, 3531–3542, doi:10.1029/JB088iB04p03531, 1983.

Chave, A. D. and Luther, D. S.: Low-Frequency , Motionally Induced Electromagnetic Fields in the Ocean, 1. Theory, J. Geophys. Res., 95, 7185–7200, 1990.

Cherry, D. W. and Stovold, A. T.: Earth Currents in Short Submarine Cables, Nature, 157, 766–766, doi:10.1038/157766a0, 1946.

Colomb, R., Alonso, C., and Nollman, I.: SAC-C Mission and the International AM Constellation for Earth Observation, in: Proceedings of the 3rd International Symposium of IAA, Berlin, April 2-6, pp. 433–437, International Symposium of IAA, 2001.

Cox, C. S.: On the electrical conductivity of the oceanic lithosphere, Phys. Earth Planet. In., 25, 196–201, doi:10.1016/0031-9201(81)90061-3, 1981.

Decker, M., Brunke, M. A., Wang, Z., Sakaguchi, K., Zeng, X., and Bosilovich, M. G.: Evaluation of the Reanalysis Products from GSFC, NCEP, and ECMWF Using Flux Tower Observations, J. Climate, 25, 1916–1944, doi:10.1175/JCLI-D-11-00004.1, 2012.

Dee, D. P., Uppala, S. M., Simmons, A. J., Berrisford, P., Poli, P., Kobayashi, S., Andrae, U., Balmaseda, M. a., Balsamo, G., Bauer, P., Bechtold, P., Beljaars, a. C. M., van de Berg, L., Bidlot, J., Bormann, N., Delsol, C., Dragani, R., Fuentes, M., Geer, a. J., Haimberger, L., Healy, S. B., Hersbach, H., Hólm, E. V., Isaksen, L., Kaallberg, P., Köhler, M., Matricardi, M., McNally, a. P., Monge-Sanz, B. M., Morcrette, J.-J., Park, B.-K., Peubey, C., de Rosnay, P., Tavolato, C., Thépaut, J.-N., and Vitart, F.: The ERA-Interim reanalysis: configuration and performance of the data assimilation system, Q. J. Roy. Meteor. Soc., 137, 553–597, doi:10.1002/qj.828, 2011.

Dill, R.: Hydrological model LSDM for operational Earth rotation and gravity field variations, Tech. rep., Helmholtz-Zentrum Potsdam Deutsches GeoForschungsZentrum, doi:11.2312/GFZ.b103-08095, 2008.

Dobslaw, H. and Thomas, M.: Simulation and observation of global ocean mass anomalies, J. Geophys. Res., 112, C05 040, doi:10.1029/2006JC004035, 2007.

Dobslaw, H., Flechtner, F., Bergmann-Wolf, I., Dahle, C., Dill, R., Esselborn, S., Sasgen, I., and Thomas, M.: Simulating high-frequency atmosphere-ocean mass variability for dealiasing of satellite gravity observations: AOD1B RL05, J. Geophys. Res., 118, 3704–3711, doi:10.1002/jgrc.20271, 2013.

Dostal, J.: Modelling of the Magnetic Field Induced by Ocean Circulation, Dissertation, Freie Universität Berlin, URL http://www.diss.fu-berlin.de/diss/receive/FUDISS_thesis_000000098809, 2014.

Dostal, J., Martinec, Z., and Thomas, M.: The modelling of the toroidal magnetic field induced by tidal ocean circulation, Geophys. J. Int., 189, 782–798, doi:10.1111/j.1365-246X.2012.05407.x, 2012.

Driscoll, J. R. and Healy, D. M.: Computing Fourier transforms and convolutions on the 2-sphere, Adv. Appl. Math., 15, 202–250, doi:10.1006/aama.1994.1008, 1994.

Evensen, G.: Inverse methods and data assimilation in nonlinear ocean models, Physica D, 77, 108–129, doi:10.1016/0167-2789(94)90130-9, 1994.

Evensen, G.: The Ensemble Kalman Filter: theoretical formulation and practical implementation, Ocean Dynam., 53, 343–367, doi:10.1007/s10236-003-0036-9, 2003.

Everett, M. E., Constable, S., and Constable, C. G.: Effects of near-surface conductance on global satellite induction responses, Geophys. J. Int., 153, 277–286, doi:10.1046/j.1365-246X.2003.01906.x, 2003.

Faraday, M.: Experimental Researches in Electricity, Philos. T. Roy. Soc. A, 122, 125–162, doi:10.1098/rstl.1832.0006, 1832.

Flosadóttir, A. H., Larsen, J. C., and Smith, J. T.: Motional induction in North Atlantic circulation models, J. Geophys. Res., 102, 10 353–10 372, doi:10.1029/96JC03603, 1997.

Friis-Christensen, E., Lühr, H., and Hulot, G.: Swarm: A constellation to study the Earth's magnetic field, Earth Planets Space, 58, 351–358, doi:10.1186/BF03351933, 2006.

Fu, L.-l., Christensen, E. J., Yamarone, C. A., Lefebvre, M., Ménard, Y., Dorrer, M., and Escudier, P.: TOPEX/POSEIDON mission overview, J. Geophys. Res., 99, 24 369, doi:10.1029/94JC01761, 1994.

Furrer, R. and Bengtsson, T.: Estimation of high-dimensional prior and posterior covariance matrices in Kalman filter variants, J. Multivariate Anal., 98, 227–255, doi:10.1016/j.jmva.2006.08.003, 2007.

Glazman, R. E. and Golubev, Y. N.: Variability of the ocean-induced magnetic field predicted at sea surface and at satellite altitudes, J. Geophys. Res., 110, C12 011, doi:10.1029/2005JC002926, 2005.

Grayver, A. V., Schnepf, N. R., Kuvshinov, A. V., Sabaka, T. J., Manoj, C., and Olsen, N.: Satellite tidal magnetic signals constrain oceanic lithosphere-asthenosphere boundary., Sci. Adv., 2, e1600 798, doi:10.1126/sciadv.1600798, 2016.

Greatbatch, R. J.: A note on the representation of steric sea level in models that conserve volume rather than mass, J. Geophys. Res., 99, 12 767, doi:10.1029/94JC00847, 1994.

Gregg, W. W., Casey, N. W., and Rousseaux, C. S.: Sensitivity of simulated global ocean carbon flux estimates to forcing by reanalysis products, Ocean Model., 80, 24–35, doi:10.1016/j.ocemod.2014.05.002, 2014.

Haagmans, R. and Plank, G.: Swarm: the Earth's Magnetic Field and Environment Explorers, Presentation, available at https://directory.eoportal.org/web/eoportal/satellite-missions/s/swarm, downloaded on September 29th, 2016.

IPCC: Climate Change 2013: The Physical Science Basis. Contribution of Working Group I to the Fifth Assessment Report of the Intergovernmental Panel on Climate Change, Cambridge University Press, Cambridge, United Kingdom and New York, NY, USA, doi:10.1017/CBO9781107415324, URL www.climatechange2013.org, 2013.

Irrgang, C., Saynisch, J., and Thomas, M.: Impact of variable seawater conductivity on motional induction simulated with an ocean general circulation model, Ocean Sci., pp. 129–136, doi:10.5194/os-12-129-2016, 2016a.

Irrgang, C., Saynisch, J., and Thomas, M.: Ensemble simulations of the magnetic field induced by global ocean circulation: Estimating the uncertainty, J. Geophys. Res. Oceans, 121, 1866–1880, doi:10.1002/2016JC011633, 2016b.

Jakobson, E., Vihma, T., Palo, T., Jakobson, L., Keernik, H., and Jaagus, J.: Validation of atmospheric reanalyses over the central Arctic Ocean, Geophys. Res. Lett., 39, doi:10.1029/2012GL051591, 2012.

Jian-Ming, J.: Theory and Computation of Electromagnetic Fields, John Wiley & Sons, Hoboken, New Jersey, 2015.

Kalman, R. E.: A New Approach to Linear Filtering and Prediction Problems, Trans. ASME, J. Basic Eng., 82, 35–45, doi:10.1115/1.3662552, 1960.

Kuvshinov, A.: 3-D Global Induction in the Oceans and Solid Earth: Recent Progress in Modeling Magnetic and Electric Fields from Sources of Magnetospheric, Ionospheric and Oceanic Origin, Surv. Geophys., 29, 139–186, doi:10.1007/s10712-008-9045-z, 2008.

Kuvshinov, A. and Semenov, A.: Global 3-D imaging of mantle electrical conductivity based on inversion of observatory C-responses-I. An approach and its verification, Geophys. J. Int., 189, 1335–1352, doi:10.1111/j.1365-246X.2011.05349.x, 2012.

Kuvshinov, A., Sabaka, T., and Olsen, N.: 3-D electromagnetic induction studies using the Swarm constellation: Mapping conductivity anomalies in the Earth's mantle, Earth Planets Space, 58, 417–427, doi:10.1186/BF03351938, 2006.

Larsen, J. C.: Electric and Magnetic Fields Induced by Deep Sea Tides, Geophys. J. R. astr. Soc., 16, 47–70, doi:10.1111/j.1365-246X.1968.tb07135.x, 1968.

Laske, G. and Masters, G.: A global digital map of sediment thickness, Eos Trans. AGU, Fall Meet. Suppl., 78, F483, 1997.

Lilley, F. E. M., Filloux, J. H., Mulhearn, P. J., and Ferguson, I. J.: Magnetic Signals from an Ocean Eddy., J. Geomag. Geoelectr., 45, 403–422, doi:10.5636/jgg.45.403, 1993.

Lindsay, R., Wensnahan, M., Schweiger, A., and Zhang, J.: Evaluation of Seven Different Atmospheric Reanalysis Products in the Arctic*, J. Climate, 27, 2588–2606, doi:10.1175/JCLI-D-13-00014.1, 2014.

Longuet-Higgins, M. S.: The electrical and magnetic effects of tidal streams, Geophys. J. Int., 5, 285–307, doi:10.1111/j.1365-246X.1949.tb02945.x, 1949.

Longuet-Higgins, M. S., Stern, M. E., and Stommel, H. M.: The electrical field induced by ocean currents and waves, with applications to the method of towed electrodes, Phys. Oceanogr. Meteor., 8, 1–37, doi:10.1575/1912/1064, 1954.

Lundahl, P., Thomsen, and Hansen, F.: Danish Ørsted Mission In-Orbit Experiences and Status of the Danish Small Satellite Program, in: Proceedings of the 13th Annual AIAA/USU Conference on Small Satellites, Logan UT, SSC99-I-8, 1999.

Luther, D. S. and Chave, A. D.: Observing 'integrating' variables in the ocean, in: Proc. 7th 'Aha Huliko'a Hawaiian Winter Workshop on Statistical Methods in Physical Oceanography, edited by Muller, P. and Henderson, D., pp. 103–130, 1993.

Macrander, A., Böning, C., Boebel, O., and Schröter, J.: Validation of GRACE Gravity Fields by In-Situ Data of Ocean Bottom Pressure, pp. 169–185, Springer Berlin Heidelberg, Berlin, Heidelberg, doi:10.1007/978-3-642-10228-8, 2010.

Manoj, C., Kuvshinov, A., Maus, S., and Lühr, H.: Ocean circulation generated magnetic signals, Earth Planets Space, 58, 429–437, doi:10.1186/BF03351939, 2006.

Masters, D., Nerem, R. S., Choe, C., Leuliette, E., Beckley, B., White, N., and Ablain, M.: Comparison of Global Mean Sea Level Time Series from TOPEX/Poseidon, Jason-1, and Jason-2, Mar. Geod., 35, 20–41, doi:10.1080/01490419.2012.717862, 2012.

Maus, S. and Kuvshinov, A.: Ocean tidal signals in observatory and satellite magnetic measurements, Geophys. Res. Lett., 31, L15 313, doi:10.1029/2004GL020090, 2004.

Maus, S., Manoj, C., Rauberg, J., Michaelis, I., and Lühr, H.: NOAA/NGDC candidate models for the 11th generation International Geomagnetic Reference Field and the concurrent release of the 6th generation Pomme magnetic model, Earth Planets Space, 62, 729–735, doi:10.5047/eps.2010.07.006, 2010.

Maxwell, J. C.: A Dynamical Theory of the Electromagnetic Field, Phil. Trans. R. Soc. Lond., 155, 459–512, doi:10.1098/rstl.1865.0008, 1865.

Meloni, A., Lanzerotti, L. J., and Gregori, G. P.: Induction of currents in long submarine cables by natural phenomena, Rev. Geophys., 21, 795–803, doi:10.1029/RG021i004p00795, 1983.

Minami, T., Toh, H., and Tyler, R. H.: Properties of electromagnetic fields generated by tsunami first arrivals: Classification based on the ocean depth, Geophys. Res. Lett., 42, 2171–2178, doi:10.1002/2015GL063055, 2015.

Nerger, L., Hiller, W., and Schröter, J.: A comparison of error subspace Kalman filters, Tellus A, 57, 715–735, doi:10.1111/j.1600-0870.2005.00141.x, 2005a.

Nerger, L., Hiller, W., and Schröter, J.: PDAF-the parallel data assimilation framework: experiences with Kalman filtering, in: Use of High Performance Computing in Meteorology-Proceedings of the 11. ECMWF Workshop, pp. 63–83, World Scientific, 2005b.

Nerger, L., Janjić, T., Schröter, J., and Hiller, W.: A Unification of Ensemble Square Root Kalman Filters, Mon. Weather Rev., 140, 2335–2345, doi:10.1175/MWR-D-11-00102.1, 2012a.

Nerger, L., Janjić, T., Schröter, J., and Hiller, W.: A regulated localization scheme for ensemble-based Kalman filters, Q. J. Roy. Meteor. Soc., 138, 802–812, doi:10.1002/qj.945, 2012b.

Olsen, N., Haagmans, R., Sabaka, T. J., Kuvshinov, A., Maus, S., Purucker, M. E., Rother, M., Lesur, V., and Mandea, M.: The Swarm End-to-End mission simulator study: A demonstration of separating the various contributions to Earth's magnetic field using synthetic data, Earth Planets Space, 58, 359–370, doi:10.1186/BF03351934, 2006.

Olsen, N., Sabaka, T. J., and Gaya-Pique, L. R.: Study of an Improved Comprehensive Magnetic Field Inversion Analysis for Swarm - Final Report, Tech. rep., Danisch National Science Center, 2007.

Parkinson, W. D. and Hutton, V. R. S.: The electrical conductivity of the Earth, vol. 3, pp. 261–232, Academic Press, San Diego, Calif., 1989.

Pham, D. T.: Stochastic Methods for Sequential Data Assimilation in Strongly Nonlinear Systems, Mon. Weather Rev., 129, 1194–1207, doi:10.1175/1520-0493(2001)129<1194:SMFSDA>2.0.CO;2, 2001.

Pham, D. T., Verron, J., and Christine Roubaud, M.: A singular evolutive extended Kalman filter for data assimilation in oceanography, J. Marine Syst., 16, 323–340, doi:10.1016/S0924-7963(97)00109-7, 1998a.

Pham, D. T., Verron, J., and Gourdeau, L.: Singular evolutive Kalman filters for data assimilation in oceanography, C. R. Acad. Sci., Ser. II, 326, 255–160, 1998b.

Rahmstorf, S.: Bifurcations of the Atlantic thermohaline circulation in response to changes in the hydrological cycle, Nature, 378, 145–149, doi:10.1038/378145a0, 1995.

Reigber, C., Lühr, H., and Schwintzer, P.: CHAMP mission status, Adv. Space Res., 30, 129–134, doi:10.1016/S0273-1177(02)00276-4, 2002.

Roemmich, D., Johnson, G., Riser, S., Davis, R., Gilson, J., Owens, W. B., Garzoli, S., Schmid, C., and Ignaszewski, M.: The Argo Program: Observing the Global Oceans with Profiling Floats, Oceanography, 22, 34–43, doi:10.5670/oceanog.2009.36, 2009.

Sabaka, T. J., Olsen, N., Tyler, R. H., and Kuvshinov, A.: CM5, a pre-Swarm comprehensive geomagnetic field model derived from over 12 yr of CHAMP, Orsted, SAC-C and observatory data, Geophys. J. Int., 200, 1596–1626, doi:10.1093/gji/ggu493, 2015.

Sabaka, T. J., Tyler, R. H., and Olsen, N.: Extracting Ocean-Generated Tidal Magnetic Signals from Swarm Data through Satellite Gradiometry, Geophys. Res. Lett., doi:10.1002/2016GL068180, 2016.

Saha, S., Moorthi, S., Pan, H.-L., Wu, X., Wang, J., Nadiga, S., Tripp, P., Kistler, R., Woollen, J., Behringer, D., Liu, H., Stokes, D., Grumbine, R., Gayno, G., Wang, J., Hou, Y.-T., Chuang, H.-Y., Juang, H.-M. H., Sela, J., Iredell, M., Treadon, R., Kleist, D., Van Delst, P., Keyser, D., Derber, J., Ek, M., Meng, J., Wei, H., Yang, R., Lord, S., Van Den Dool, H., Kumar, A., Wang, W., Long, C., Chelliah, M., Xue, Y., Huang, B., Schemm, J.-K., Ebisuzaki, W., Lin, R., Xie, P., Chen, M., Zhou, S., Higgins, W., Zou, C.-Z., Liu, Q., Chen, Y., Han, Y., Cucurull, L., Reynolds, R. W., Rutledge, G., and Goldberg, M.: The NCEP Climate Forecast System Reanalysis, B. Am. Meteorol. Soc., 91, 1015–1057, doi:10.1175/2010BAMS3001.1, 2010.

Sanford, T. B.: Motionally induced electric and magnetic fields in the sea, J. Geophys. Res., 76, 3476–3492, doi:10.1029/JC076i015p03476, 1971.

Saynisch, J. and Thomas, M.: Ensemble Kalman-Filtering of Earth rotation observations with a global ocean model, J. Geodyn., 62, 24–29, doi:10.1016/j.jog.2011.10.003, 2012.

Saynisch, J., Bergmann-Wolf, I., and Thomas, M.: Assimilation of GRACE-derived oceanic mass distributions with a global ocean circulation model, J. Geodesy, 89, 121–139, doi:10.1007/s00190-014-0766-0, 2014.

Saynisch, J., Semmling, M., Wickert, J., and Thomas, M.: Potential of space-borne GNSS reflectometry to constrain simulations of the ocean circulation, Ocean Dynam., 65, 1441–1460, doi:10.1007/s10236-015-0886-y, 2015.

Saynisch, J., Petereit, J., Irrgang, C., Kuvshinov, A., and Thomas, M.: Impact of climate variability on the tidal oceanic magnetic signal-A model-based sensitivity study, J. Geophys. Res. Oceans, 121, 5931–5941, doi:10.1002/2016JC012027, 2016.

Saynisch, J., Petereit, J., Irrgang, C., and Thomas, M.: Impact of global warming on electromagnetic oceanic tidal signals – a CMIP5 climate model based sensitivity study, Geophys. Res. Lett. (in review), 2017.

Schnepf, N. R., Manoj, C., Kuvshinov, A., Toh, H., and Maus, S.: Tidal signals in ocean-bottom magnetic measurements of the Northwestern Pacific: observation versus prediction, Geophys. J. Int., 198, 1096–1110, doi:10.1093/gji/ggu190, 2014.

Schnepf, N. R., Kuvshinov, A., and Sabaka, T.: Can we probe the conductivity of the lithosphere and upper mantle using satellite tidal magnetic signals?, Geophys. Res. Lett., doi:10.1002/2015GL063540, 2015.

Schnepf, N. R., Manoj, C., An, C., Sugioka, H., and Toh, H.: Time–Frequency Characteristics of Tsunami Magnetic Signals from Four Pacific Ocean Events, doi:10.1007/s00024-016-1345-5, URL http://link.springer.com/10.1007/s00024-016-1345-5, 2016.

Stephenson, D. and Bryan, K.: Large-scale electric and magnetic fields generated by the oceans, J. Geophys. Res., 97, 15 467–15 480, doi:10.1029/92JC01400, 1992.

Stommel, H.: The theory of the electric field induced in deep ocean currents, J. Mar. Res., 7, 386–392, 1948.

Szuts, Z. B.: Relationship between ocean velocity and motionally induced electrical signals: 2. In the presence of sloping topography, J. Geophys. Res., 115, C06 004, doi:10.1029/2009JC006054, 2010.

Tapley, B. D., Bettadpur, S., Watkins, M., and Reigber, C.: The gravity recovery and climate experiment: Mission overview and early results, Geophys. Res. Lett., 31, L09 607, doi:10.1029/2004GL019920, 2004.

Thébault, E., Finlay, C. C., Beggan, C. D., Alken, P., Aubert, J., Barrois, O., Bertrand, F., Bondar, T., Boness, A., Brocco, L., Canet, E., Chambodut, A., Chulliat, A., Coïsson, P., Civet, F., Du, A., Fournier, A., Fratter, I., Gillet, N., Hamilton, B., Hamoudi, M., Hulot, G., Jager, T., Korte, M., Kuang, W., Lalanne, X., Langlais, B., Léger, J.-M., Lesur, V., Lowes, F. J., Macmillan, S., Mandea, M., Manoj, C., Maus, S., Olsen, N., Petrov, V., Ridley, V., Rother, M., Sabaka, T. J., Saturnino, D., Schachtschneider, R., Sirol, O., Tangborn, A., Thomson, A., Tøffner-Clausen, L., Vigneron, P., Wardinski, I., and Zvereva, T.: International Geomagnetic Reference Field: the 12th generation, Earth Planets Space, 67, 79, doi:10.1186/s40623-015-0228-9, 2015.

Thomas, M., Sündermann, J., and Maier-Reimer, E.: Consideration of ocean tides in an OGCM and impacts on subseasonal to decadal polar motion excitation, Geophys. Res. Lett., 28, 2457–2460, doi:10.1029/2000GL012234, 2001.

Toh, H., Satake, K., Hamano, Y., Fujii, Y., and Goto, T.: Tsunami signals from the 2006 and 2007 Kuril earthquakes detected at a seafloor geomagnetic observatory, J. Geophys. Res., 116, B02 104, doi:10.1029/2010JB007873, 2011.

Tyler, R. H. and Mysak, L. a.: Motionally-induced electromagnetic fields generated by idealized ocean currents, Geophys. Astro. Fluid., 80, 167–204, doi:10.1080/03091929508228954, 1995.

Tyler, R. H., Mysak, L. A., and Oberhuber, J. M.: Electromagnetic fields generated by a three dimensional global ocean circulation, J. Geophys. Res., 102, 5531–5551, doi:10.1029/96JC03545, 1997.

Tyler, R. H., Oberhuber, J. M., and Sanford, T.: The potential for using ocean generated electromagnetic fields to remotely sense ocean variability, Phys. Chem. Earth, 24, 429–432, doi:10.1016/S1464-1895(99)00054-X, 1998.

Tyler, R. H., Maus, S., and Lühr, H.: Satellite observations of magnetic fields due to ocean tidal flow, Science, 299, 239–241, doi:10.1126/science.1078074, 2003.

Velímský, J. and Martinec, Z.: Time-domain, spherical harmonic-finite element approach to transient three-dimensional geomagnetic induction in a spherical heterogeneous Earth, Geophys. J. Int., 161, 81–101, doi:10.1111/j.1365-246X.2005.02546.x, 2005.

Vennerstrom, S., Friis-Christensen, E., Lühr, H., Moretto, T., Olsen, N., Manoj, C., Ritter, P., Rastätter, L., Kuvshinov, A., and Maus, S.: The Impact of Combined Magnetic and Electric Field Analysis and of Ocean Circulation Effects on Swarm Mission Performance, Tech. rep., Danish National Space Center, Kgs. Lyngby, Denmark, 2005.

Vivier, F., Meier-Reimer, E., and Tyler, R. H.: Simulations of magnetic fields generated by the Antarctic Circumpolar Current at satellite altitude: Can geomagnetic measurements be used to monitor the flow?, Geophys. Res. Lett., 31, L10 306, doi:10.1029/2004GL019804, 2004.

Wollaston, C.: Discussion on 'Earth Currents', J. Soc. Telegr. Eng., 10, 44–56, doi:10.1049/jste-2.1881.0005, 1881.

Yu, L., Gao, Y., and Otterå, O. H.: The sensitivity of the Atlantic meridional overturning circulation to enhanced freshwater discharge along the entire, eastern and western coast of Greenland, Clim. Dynam., 46, 1351–1369, doi:10.1007/s00382-015-2651-9, 2015.

Dank

Die geschriebenen Wörter, Zeilen und Kapitel, erzählen meistens nicht die ganze Geschichte. So ist es auch bei dieser Arbeit. Denn ohne die unermessliche Unterstützung durch meine Familie, Freunde und Kollegen, wäre diese Dissertation und das ganze Promotionsprojekt sicher nicht möglich gewesen. Hier möchte ich mich bei euch bedanken.

Ich danke Prof. Dr. Maik Thomas und Prof. Dr. Rupert Klein, meinen beiden Betreuern in der GeoSim-Graduiertenschule, dass sie mir ihr Vertrauen und ihre Unterstützung boten, um eine Promotion anzustreben. Maik danke ich ebenfalls für meinen ersten Gedanken an ozeanische elektromagnetische Felder – ein Funke, dessen Faszination mich maßgeblich während des gesamten Promotionsprojektes angetrieben hat.

Ich danke Dr. Jan Saynisch für seine fachliche Betreuung und, dass er es mit stoischer Gelassenheit drei Jahre lang nicht aufgegeben hat, einem Mathematiker etwas über den (echten und modellierten) Ozean beizubringen. Jan danke ich auch für unsere vielen Mythenmetz'schen Abschweifungen durch wahrscheinlich fast alle multidimensionalen Räume, die man sich vorstellen kann – mir hat es immer großen Spaß bereitet.

I thank Jorge Bernales for being the best office mate in the world. It was a great pleasure to share the office with you during the last years. In those dark days, when nothing worked nor compiled, you still managed to make me laugh. Every time.

Ich danke Dr. Volker Klemann und Dr. Jan Hagedoorn dafür, dass ich immer wieder aus ihrem wirklich unerschöpflichen Wissen über elektromagnetische Induktion, Kugelflächenfunktionen, GMT und Latex schöpfen durfte.

Natürlich danke ich der gesamten Sektion 1.3 der Erdsystem-Modellierung am GFZ, allen KollegInnen, Mit-DoktorandInnen und neuen Freunden. Die letzten drei Jahre waren in jeder Hinsicht intensiv und ich werde mich immer gerne an diese Zeit erinnern – dank euch.

Vor allem aber danke ich meinen Eltern, Eva und Hubert Irrgang, die immer alles daran gesetzt haben, dass aus dem Jungen was wird. Ob das gelungen ist, vermag ich nicht zu beurteilen. Ich danke euch dafür, dass ihr immer für mich da seid, ganz egal, in welche Richtung es geht.

Meiner Frau, Anna, kann ich gar nicht genug danken. Während der ganzen letzten Jahre warst und bist du mein Ruhepol – durch dich erscheint mir jede Hürde wie ein Katzensprung. Ohne dich wären diese Seiten leer.

Eidesstattliche Erklärung

Hiermit versichere ich an Eides statt, die vorliegende Dissertation selbstständig und ohne unerlaubte Hilfe angefertigt zu haben.

Bei der Verfassung der Dissertation wurden keine anderen als die im Text aufgeführten Hilfsmittel verwendet.

Ein Promotionsverfahren zu einem früheren Zeitpunkt an einer anderen Hochschule oder bei einem anderen Fachbereich wurde nicht beantragt.

_____   _____
Ort, Datum   Christopher Irrgang